SYNTHESIS AND FUNCTIONAL PROPERTIES OF Ni-Mn-Ga FERROMAGNETIC SHAPE MEMORY THIN FILMS

SYNTHESIS AND FUNCTIONAL PROPERTIES OF Ni-Mn-Ga FERROMAGNETIC SHAPE MEMORY THIN FILMS

By

YUEPENG ZHANG, M.A.SC.

A Thesis
Submitted to the School of Graduate Studies
in Partial Fulfilment of the Requirements
for the Degree of
Doctor of Philosophy

McMaster University

DOCTOR OF PHILOSOPHY (2009)	McMaster University
(Department of Materials Science and Engineering)	Hamilton, Ontario

TITLE:	SYNTHESIS AND FUNCTIONAL PROPERTIES OF Ni-Mn-Ga FERROMAGNETIC SHAPE MEMORY THIN FILMS
AUTHOR:	Yuepeng Zhang, M.A.Sc. (McMaster University)
SUPERVISORS:	Professor Marek Niewczas and Gianluigi A. Botton
NUMBER OF PAGES:	xv, 165

Abstract

The purpose of this work was to develop a growth pathway for synthesis of high-quality ferromagnetic Ni-Mn-Ga shape memory thin films and to understand their functional properties.

Two groups of Ni-Mn-Ga films were prepared using the pulsed laser deposition technique. One group was grown on (100) YSZ ($(Zr,Y)O_2$ with ZrO_2:Y_2O_2=92:8) and was used to study the thermal, magnetic, and magnetocaloric properties. The other group was deposited on (100) MgO. These films were fabricated into free-standing micro-bridges.

These Ni-Mn-Ga films were synthesized in a previously unexplored high temperature deposition regime. The temperatures employed encouraged the development of the desired micrometer-size highly twinned martensite grain structure while the general problem of preferential evaporation of the volatile elements at elevated temperatures was solved by using a manganese and gallium enriched target.

The films grown on (100) YSZ exhibit a self-reversible, magnetically induced reorientation of the martensite variants (MIR), which is temperature dependent. The mechanism associated with the self-activated reversibility in the MIR effect was established through a detailed characterization of the texture, microstructure, and magnetic domain structure of the films.

The synthesized films also show a large magnetocaloric effect (MCE), which is particularly strong at low magnetic fields. The effect is associated with an overlapped ferromagnetic and martensitic phase transition. Detailed characterization of these transitions allow for an understanding of the role each phase transition plays in determining the level of enhancement to a standard MCE governed only by the ferromagnetic phase transition.

Ni-Mn-Ga free-standing micro-bridges were fabricated using photolithography followed by wet chemical etching. Microstructural evolution of the martensitic variants resulting from changes to the stress field in the detached areas was studied in the context of potential film applications for micro-actuators.

Acknowledgements

There are many people to whom I owe a debt of gratitude for their help with my studies, without which I could never have completed this work.

I wish to express my sincere appreciation to my supervisor Dr. Marek Niewczas for his continuous guidance and encouragement. The road towards a doctorate was not a smooth path as I experienced many difficulties. I still recall the three years of hard times which we spent trying to optimize the film growth conditions. After growing more than 500 samples we still could not obtain satisfactory films. The feeling was like someone hopelessly groping in the dark for a light switch. It was the encouragement of Dr. Niewczas that stimulated me towards the final success. Dr. Niewczas also provided me with strong academic support. His insightful discussions and advice helped me overcome obstacles. At the same time, Dr. Niewczas gave me great freedom in carrying out my research. I was able to decide what my research objectives would be and how I would achieve them. This self-learning process greatly aroused my enthusiasm for research and innovation. It also helped me to improve my ability to conduct research independently.

In addition, I am especially grateful to my co-supervisor, Dr. Gianluigi Botton. He has incredible knowledge and deep insight in the field of nanotechnology and electron microscopy. His comments and advice are always the most valuable in these areas. Dr. Botton is a very thoughtful professor who always shows considerations for students. It was a very pleasant and enjoyable experience to work with him.

In particular, I would like to thank Dr. Robert Hughes for his long-term interest, passion, and support for the project. Rob is a very quick-minded and creative person. His personality which seeks perfection ensured that I obtained a source of high quality samples. His passion for research made him to get involved in the work well beyond the scope of just sample growth. His comments on texture analysis and transport properties were extremely valuable.

I would also like to acknowledge Dr. Adrian Kitai and Dr. John Preston who generously allowed me to use their sputtering and laser deposition chambers during my Ph. D. studies. They provided me tremendous help and support as well as valuable advice.

I would like to thank to Dr. Jim Britten from whom I achieved a solid knowledge of crystallography, texture, and X-ray diffraction/absorption. Dr. Britten is very warm-hearted. He often sacrificed his spare time to help me with XRD measurements. He trained me to use his 3D-XRD facilities and allowed me to attach my in-house temperature control device to his equipments. I was very fortunate to have his support.

McMaster is a fantastic place for studying and performing research and where a large group of outstanding scientists are gathered. Dialogue with them has had a direct influence on my research. In particular, I would like to thank Dr. David Embury, Dr. Malcolm

Collins, and Dr. John Greedan for their invaluable insight and fruitful discussions.

Progress would be greatly obstructed without the help of excellent technical personnel. Gratitude is given to Dr. Paul Dube, Mr. Andy Duft, Mr. Jim Garrett, Mr. Wenhe Gong, Dr. Steve Koprich, and Mr. Fred Pearson, for their great help and technical excellence.

Thanks also goes out to the researchers and students in the departments of materials science and engineering physics, whom over the years contributed to the fantastic collaborative atmosphere and friendship, in particular Dr. Carmen Andrei, Dr. Nadi Braidy, Dr. Shery Chang, Dr. Martin Couillard, Dr. Antoni Dabkowski, Dr. Andi M. Limarga, Dr. Christian Maunders, Dr. Yang Shao, Dr. Florent Lefevre-Schlick, Dr. Kevin Spencer, Dr. Xiang Wang, Dr. Arnaud Weck, Dr. Ping Wei, Dr. Tao Wu, Dr. Yingwei Xiang, Mariana Budiman, Edgar Huante Ceron, Kai Cui, Gabriel Devenyi, Lina Gunawan, Akhide Hosakawa, Julia Huang, Juan Kong, Jing Li, Beth McNally, Pawel Okrutny, Ana Villafranca, Tihe Zhou, and Guozhen Zhu.

A special acknowledgement goes out to Dr. Kui Yu-Zhang whose care and encouragement inspired me throughout the entire course of my Ph.D. studies.

Finally, I would like to thank my husband Liang. His love, understanding, support, and patience enabled me to complete this work. A special thought is also devoted to my parents for the never-ending support.

Hamilton, August 2009
Yuepeng Zhang

Contents

List of Figures

List of Tables

Chapter 1

Introduction

The shape memory effect (SME) is a phenomenon whereby a material restores its previously defined shape or size when subjected to an appropriate thermo-mechanical treatment. The shape recovery, as shown in figure 1.1, is accomplished in three steps: (1) the sample is cooled so that it transforms from the cubic to a crystal structure with lower symmetry (e.g. tetragonal structure); (2) it is then mechanically deformed in the tetragonal phase; (3) the shape is recovered during a subsequent heating process where the sample transforms back to the initial cubic structure.

Since its first discovery within a Au-Cd alloy in 1951, the SME has been studied and utilized for a wide variety of applications, such as actuators, sensors, coupling devices, dental braces, and vascular stents (Anson, 1999; Mavroidis, 2002; Tung *et al.*, 2008). Recently, the SME was observed in a group of ferromagnetic alloys in which the shape change is induced by an external magnetic field (Ullakko *et al.*, 1996), an effect now referred to

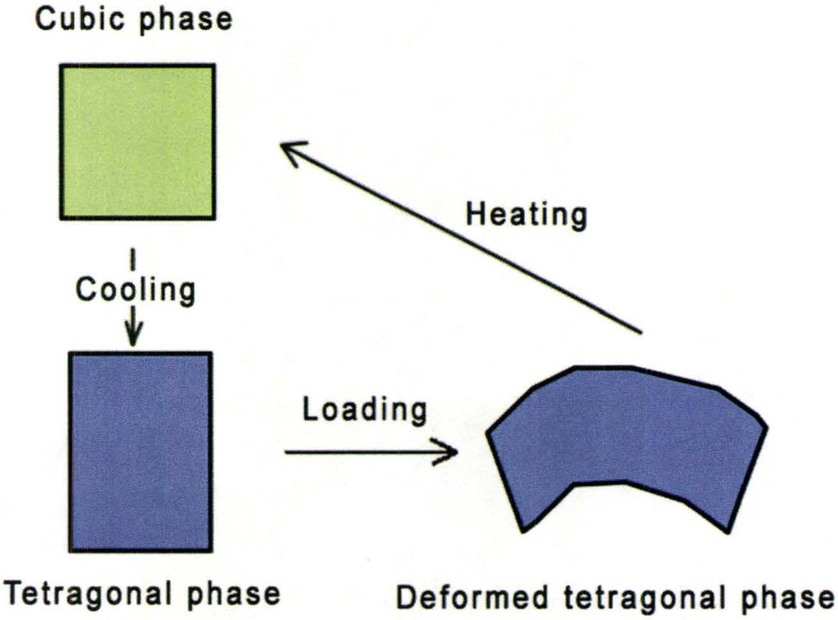

Figure 1.1: Schematic depiction of the shape memory process

as the magnetic shape memory effect (MSM). This finding opens the door to a new field of applications where fast actuation and energy generation become possible. Among these MSM alloys the most promising results have been obtained with the Ni-Mn-Ga ternary system which exhibits magnetic field induced strains of ∼9.5% (Sozinov *et al.*, 2002b), a value significantly larger than the strains observed in other fast-response actuation materials such as piezoelectric and magnetostrictive materials (Park & Shrout, 1997; Li *et al.*, 2008; Pasquale, 2003). Operating frequencies of several thousand hertz have been achieved with ferromagnetic Ni-Mn-Ga actuators (Suorsa *et al.*, 2004; Marioni *et al.*, 2003). These distinctive features make the Ni-Mn-Ga alloys an intriguing system to study.

Ni-Mn-Ga alloys, in addition to their shape memory effect, show a strong magnetocaloric effect (MCE) while being magnetized or demagnetized. The effect is associated with a large adiabatic temperature change and thus can be applied to potential refrigeration technologies. Such a technology may eliminate the need for energetically inefficient compressors and volatile liquid refrigerants which are ozone-depleting and linked to global-warming. Therefore, Ni-Mn-Ga alloys may provide more environmentally friendly cooling technologies as compared to the conventional gas compression technology (Gschneidner & Pecharsky, 2000). Figure 1.2 depicts a typical magnetic refrigeration cycle. An isolated magnetic refrigerant element is subjected to a magnetic field which is ramped up from a low to a high value. The field aligns the magnetic dipoles in the refrigerant element and lowers its magnetic entropy. Since the material is isolated, the drop in the magnetic entropy is compensated for by the increase of the lattice entropy, leading to an increase in temperature of the refrigerant element. The generated heat is then removed by attaching to the refrigerant a cooled water sink. During the heat transfer the magnetic field is kept constant to prevent the dipoles from being misaligned. Once the refrigerant element is sufficiently cooled, the coolant is removed, leaving the refrigerant isolated. Switching off the magnetic field disorders the magnetic dipoles through the consumption of thermal energy and lowers the temperature of the magnetic refrigerant material. The cooled refrigerant element is then thermally linked to the environment to be cooled where it absorbs heat. The whole process benefits from a large magnetic entropy change or an adiabatic temperature change in the magnetic refrigerant substance during the magnetization and demagnetization process.

One of the most broadly investigated magnetic refrigerant materials is gadolinium which shows a magnetic entropy change of approximately -12 J/kg-K near room temperature for a magnetic field change from 0 to 5 T (Gschneidner & Pecharsky, 2000). The gadolinium-based compound, $Gd_5(Si_{1-x}Ge_x)_4$, has been recognized as the best material available today for magnetic refrigeration. The $Gd_5(Si_{1-x}Ge_x)_4$ with x=0.25 demonstrates a giant magnetic

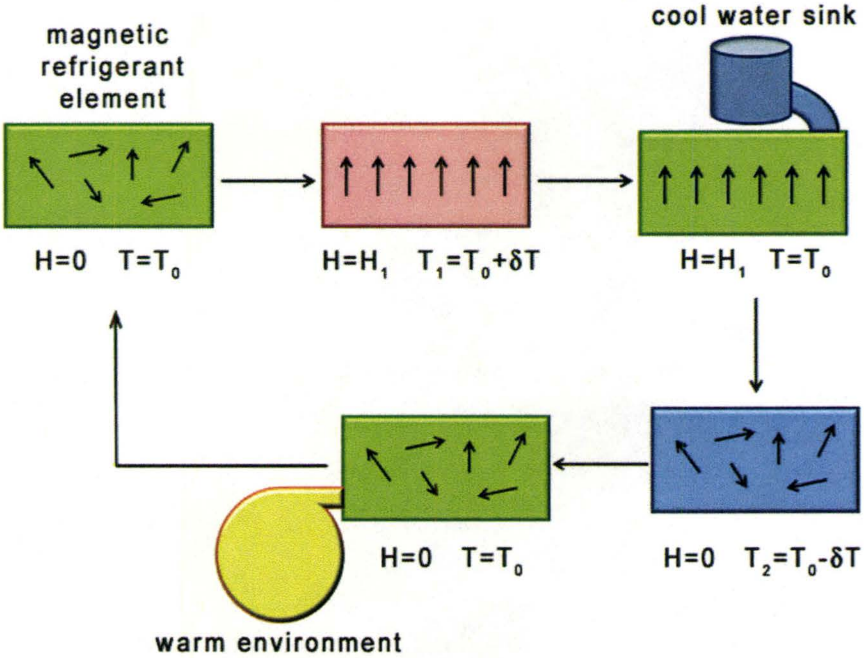

Figure 1.2: Refrigeration cycle of a magnetic refrigerant element showing the mechanism for magnetic refrigeration.

entropy change of -70 J/kg-K at 140 K for a field change of 5 T (Pecharsky & Gschneidner, 1997), a value seven times larger than gadolinium. Recently, a giant magnetic entropy change of -86 J/kg-K for fields ramped to 5 T has been reported for a magnetic shape memory Ni-Mn-Ga single crystal at 312.75 K (Pasquale *et al.*, 2005), which is comparable to that observed for $Gd_5(Si_{1-x}Ge_x)_4$. In addition, a direct measurement of the adiabatic temperature change has been carried out on a $Ni_{2.19}Mn_{0.81}Ga$ polycrystalline sample, which yields a temperature change of 1.1 K/T at 336 K (Khovaylo *et al.*, 2008). These results demonstrate the incredible potential of the Ni-Mn-Ga system as a magnetic refrigerant substance.

While progress has been considerable in terms of the bulk Ni-Mn-Ga alloys, advances in thin film properties and devices have been slow. This is despite the fact that such films are excellent candidates for micrometer-scale applications. Compared with the bulk material, thin films have the advantages of having better ductility (Kohl *et al.*, 2006), a higher power density, and a lower driving field. Various techniques have been applied for film preparation, including sputtering (Thomas *et al.*, 2008a; Porsch *et al.*, 2008), pulsed laser deposition (Hakola *et al.*, 2004a; Golub *et al.*, 2004; Zhang *et al.*, 2009), molecular beam epitaxy (Dong *et al.*, 2000), and flash evaporation (Dubowik *et al.*, 2004). However, the quality of the films produced thus far has varied widely. Although shape memory and micro-actuation behavior has been demonstrated in free-standing films (Dong *et al.*, 2004; Ohtsuka *et al.*, 2006), a vast majority of the results available in the literature reveal that films affixed to a rigid substrate show no discernable magnetically induced strain. In terms of the magnetocaloric effect, there exists only one report describing this effect for Ni-Mn-Ga thin films, which was published very recently (Recarte *et al.*, 2009). The challenge is therefore to grow uniform, defect-free, and highly textured films with a grain size large enough to accommodate internal twinning, a microstructure important for obtaining the shape change in this material.

In an effort to address these challenges, the current research had the objective of developing a growth pathway that allowed for the optimization of both the crystallinity and microstructure of the films and achieve MSM and/or MCE functionalities for these films. This objective has been fulfilled through a high temperature *in-situ* deposition process where the loss of the volatile elements (i.e. Mn and Ga) at elevated temperatures due to their high vapour pressure is compensated for by using a target enriched with these elements. The films prepared in this manner show a high degree of crystallinity with micrometer-sized grains, a well-controlled texture, and a heavily twinned microstructure which is highly desired for the MSM effect. Systematic characterization of the thermal, magnetic, and transport properties reveals that these films can transform freely between the high and low temperature phases associated with the MSM effect. The films' saturation magnetization is comparable to that of the bulk Ni-Mn-Ga crystals. The most important is the fact that the as-grown films show evidence of a reduced magnetic field induced strain (MFIS), indicative of a MSM capability. Distinctive to the films is the fact that the MFIS shows self-activated reversibility, a feature circumventing the need for an external stimulus, and thus, greatly enhancing the compactness and affordability of the micro-scale devices. While the phenomenon was first observed by a German group in 2008 for films deposited on (001)MgO and (001)$SrTiO_3$ using a sputtering method (Heczko *et al.*, 2008; Thomas *et al.*, 2008a), the contribution of this thesis work is to provide a systematic study of the effect, characterize its temperature dependency, correlate the behavior to the observed crystallographic and magnetic domain structure, and propose a mechanism for the self-reversibility.

Another significant contribution of the present work is the understanding of a large magnetocaloric effect (MCE) in the aforementioned films, which is an important step towards the development of the magnetic devices to be used for micro-length-scale refrigeration applications. The effect is attributed to the concurrent structural and magnetic phase transitions. The MCE observed here is particularly strong at low fields, yielding a magnetic entropy change of -1.4 J/kg-K at 355 K for a magnetic field change of only 0.5 T. Detailed characterization of the temperature dependent magnetic, structural, and transport properties indicate that the maximum magnetic entropy change occurs at the temperature where the austenitic and martensitic phases coexist at equal volume fractions, rather than at the Curie or martensitic transformation start temperatures as reported in the literature (Gschneidner & Pecharsky, 2000; Zhou *et al.*, 2005a). Consistent with this finding is the temperature dependence of the magnetic entropy change where the position of the peak is dependent upon whether a heating or cooling sequence is used. A 3 K temperature hysteresis has been observed between the two thermal paths. An in-depth study of these features allows for an understanding of the role each phase transition plays in determining the level of enhancement to a standard MCE which is governed only by a ferromagnetic phase transition.

To help readers to get a better understanding of the topics discussed in this thesis, a review of the fundamentals of the magnetic shape memory effect, the magnetically induced strain, and the magnetocaloric effect, as well as the basic properties of the Ni-Mn-Ga ternary system is provided before introducing any experimental results; this will be done in the next chapter. The acronyms and abbreviations used in this work are listed in table 1.1.

Table 1.1: Listing of the acronyms and abbreviations used in the body of this thesis.

AFM	atomic force microscopy
BF	TEM bright-field image
DF	TEM dark-field image
DP	diffraction pattern
MCE	magnetocaloric effect
MESP	metal coated etched silicon probe
MFIS	magnetic field induced strain
MFM	magnetic force microscopy
MIR	magnetic field induced reorientations of martensitic twin variants
MPMS	magnetic property measurement system
MSM	magnetic shape memory effect
PLD	pulsed laser deposition
RC	refrigerant capacity
SEM	scanning electron microscopy
SME	shape memory effect
SPM	scanning probe microscopy
SQUID	superconducting quantum interference device
TEM	transmission electron microscopy
XEDS	X-ray energy dispersive spectroscopy
XRD	X-ray diffraction
XRD^3	three-dimensional X-ray diffraction

Chapter 2

Literature Review

This chapter provides fundamental knowledge regarding the magnetic shape memory effect (MSM) as well as the structure and properties of Ni-Mn-Ga bulk materials, which will help readers understand the characteristics of the Ni-Mn-Ga shape memory thin films described in subsequent chapters. The first part of the chapter describes the mechanism behind the MSM effect, which is followed by a review of the physical properties of Ni-Mn-Ga ternary alloys. The third section details a specific feature of the magnetic shape memory alloys, which relies on the interaction between twin-related structural domains in an external magnetic field. This feature appears to be an important prerequisite for the MSM effect. The fourth section is dedicated to the underlying physics of the magnetocaloric effect, a property that can be used in various magnetic refrigeration applications. The last section introduces the progess achieved in the development and the understanding of the Ni-Mn-Ga thin films.

2.1 Ferromagnetic Shape Memory Alloys

The shape memory effect (SME) is reliant upon a reversible structural phase transformation, where the material transforms from a high temperature cubic phase to a low temperature tetragonal phase followed by plastic deformation at a low temperature. Upon heating, the deformed material transforms back to the cubic phase through reverse phase transformation and recovers its original shape. The structural phase transformation responsible for the SME is a martensitic transformation; the high and low temperature phases are referred to as the austenitic and martensitic phase.

The martensitic transformation is a special structural phase transformation. It is diffusionless and proceeds through a cooperative displacement (shear) of the atoms in the austenitic phase. The amount of the atomic displacement is quite small, usually less than a single atomic spacing (Christian, 1987). Due to the shearing process, there exists a rigorous crystallographic relationship between the lattices of the martensitic and the austenitic phases. The degree of transformation is temperature dependent and the whole process is characterized by four critical temperatures M_s, M_f, A_s, and A_f, which correspond to the start and finish temperatures for the martensitic and austenitic transformations. These temperatures can be determined at the position where the temperature dependence of some physical properties, e.g. electrical resistivity or heat capacity, exhibit deviation from their normal behaviour, as shown in figure 2.1.

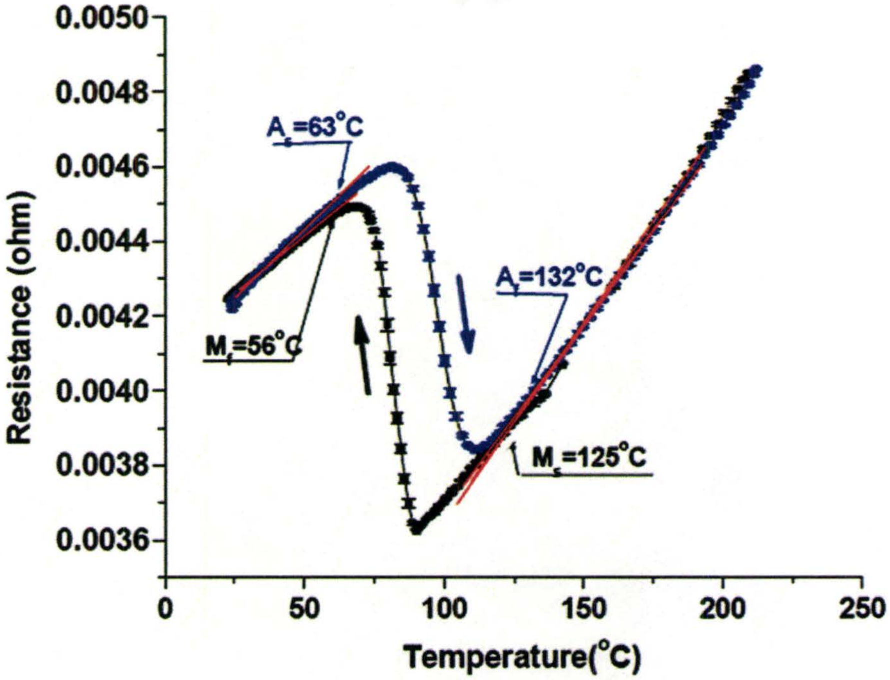

Figure 2.1: Resistance versus temperature curve for a polycrystalline Cu-15.0Zn-8.2Al (at.%) sample showing a reversible martensitic phase transformation. The characteristic temperatures are determined at the position where the slope of the resistance curve starts to change (Zhang, 2003).

2.1.1 Thermoelastic Martensitic Phase Transformation

Not all materials that go through the martensitic phase transformation show a shape memory effect. The effect is only achievable through a particular type of martensitic transformation, i.e. a thermoelastic martensitic transformation, which has a number of distinctive features (Christian, 1987):

- For a thermoelastic martensitic transformation, the martensite grows and vanishes continuously with changing temperature, while it grows almost instantaneously to its final size for the general martensitic transformation.

- The martensite crystals shrink along the same path when they transform back to the austenitic phase during the reverse thermoelastic martensitic transformation, which is usually not achievable in the general martensitic transformation.
- Materials that undergo a thermoelastic transformation have an ordered austentic crystal structure while those that go through the general martensitic transformation often have a disordered austenitic phase.
- Due to the ordered structure, the interfacial energy between the martensitic and austenitic phases generated during the thermoelastic martensitic transformation is much smaller by comparison to the general martensitic transformation. A smaller driving force is therefore associated with the thermoelastic transformation.

2.1.2 Shape Memory Effect

The mechanism behind the shape memory effect has been introduced in Chapter 1. Here, the shape recovery process is discussed in more detail. As shown in figure 2.2, the shape memory effect is accomplished in three steps: (1) the sample is firstly cooled to transform from a high symmetry austenitic phase to a low symmetry martensitic phase; (2) the material is then deformed in the martensitic phase under an external load; (3) the shape recovery ensues as the sample is transformed back to the austenitic phase upon heating through the reverse martensitic transformation. As mentioned previously, there exists an inherent and precise crystallographic relationship between the lattices of the martensitic and the austenitic phase. The relationship is established during the small shuffling of the neighboring atoms in the forward martensitic transformation in step (1). This lattice correspondence guarantees the shape recovery in the reverse phase transformation during step

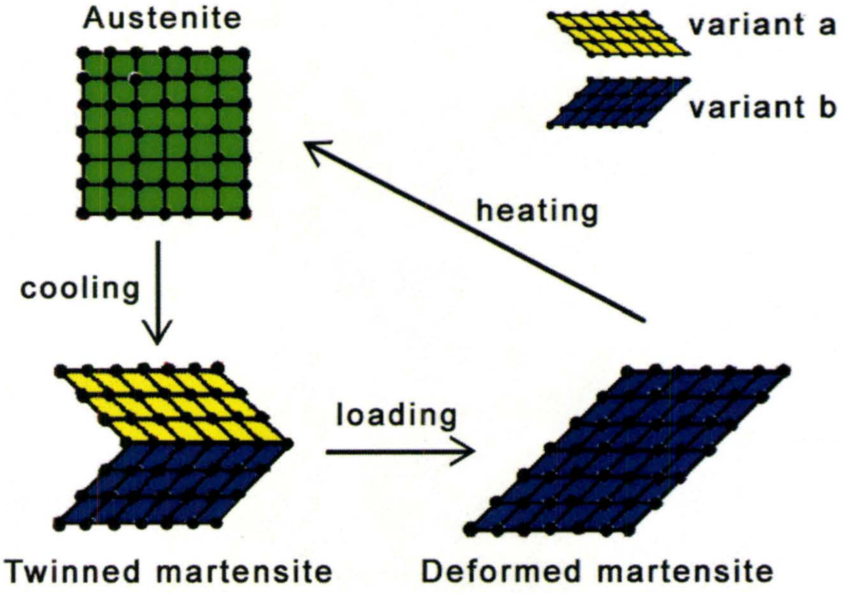

Figure 2.2: Schematic representation of the mechanism governing a shape memory effect. (Adapted from (Ryhanen, 1999))

(3). The deformation of the sample is usually performed in the martensitic phase because it is more ductile and more easily deformed than the austenitic phase due to its heavily twinned nature.

When the transformation from the cubic austenitic to the non-cubic martensitic phase initiates, small martensitic crystals form within an austenitic matrix. These crystals, which have identical structures but different orientations, are referred to as variants. As shown in figure 2.2, the adjacent variants are twin-related to accommodate the transformation strain. Sometimes four variants will exist in a side-by-side arrangement to form a diamond-shaped structure where the twinning relationship is established between any two adjacent variants (Funakubo, 1987). The heavily twinned structure effectively reduces the elastic energy resulting from the phase transformation. Due to the large elastic limit of the martensitic phase a plastic strain is seldom induced in the phase transformation process (Vasil'ev *et al.*, 1999). Upon application of an external load, the differently oriented martensitic variants transform between one another through twin boundary motion, which gives rise to a large shape change in the martensitic phase.

2.1.3 Magnetic Shape Memory Effect

Recently, the shape memory behaviour was observed in ferromagnetic Heusler alloys where the shape-changes could be induced by a magnetic field, giving rise to a magnetic shape memory (MSM) effect.

The MSM effect is also dependent upon a reversible thermoelastic martensitic transformation, as is the case for the conventional SME. However, during MSM the deformation in the martensitic phase is stimulated by a magnetic field, rather than a mechanical load, although the latter can also be used to induce the shape memory effect. The deformation is accomplished through a process where the magnetic-field-favourable variants grow at the expense of the unfavourable ones by means of twin boundary motion, i.e. the magnetically induced martensitic variant reorientation (MIR). The effect is strongly dependent upon the coupling between the structural and magnetic subsystems. To realize MSM function, the materials have to have a high saturation magnetization, a high magnetic anisotropy, and a low twinning stress (Wilson *et al.*, 2007). A key feature of the MSM is the MIR effect; the effect will be discussed separately in Section 2.3.

2.1.4 Large Magnetic Field Induced Strain

As described previously, a detwinning process is triggered when the martensitic variants are subjected to an external magnetic field where the variants transform from one to the other leading to a deformation strain. Optimization of the effect has yielded magnetic field induced strains of 9.5% in a single crystal martensite in a magnetic field of less than 1 Tesla (Sozinov *et al.*, 2002b). The mechanism for the large magnetic field induced strain (MFIS) is shown in figure 2.3. The sample is initially mechanically loaded such that it contains a single martensite variant (i.e. Variant A). The variant has a tetragonal unit cell with a tetragonality smaller than one ($c/a<1$). Its magnetic easy axis is oriented along the short c-axis (i.e. crystallographic [001] direction) of the unit cell. When a lateral magnetic field (H) is applied, the variants whose c-axis is along the field direction (i.e. Variant B) nucleate inside the original variant (i.e. Variant A) to reduce the magnetic Zeeman energy. The newly generated variants form a twin relationship with the original variants. When the magnetic field strength exceeds a critical value, the new variants grow at the expense of the original ones through twin boundary propagation. Finally, the entire sample transforms to the newly generated variants. Since the unit cells of Variant A and Variant B are perpendicular to one another, the total effect is analogous to rotating the sample by 90° to create a strain of $\varepsilon=a/c-1$ in the vertical direction. Apparently, the magnitude of the field-induced strain is dependent upon the tetragonality of the martensitic unit cell, which is typically several percent, a value significantly larger than the strains observed in fast-response piezoelectric (Park & Shrout, 1997; Li *et al.*, 2008) and magnetostrictive materials (Pasquale, 2003).

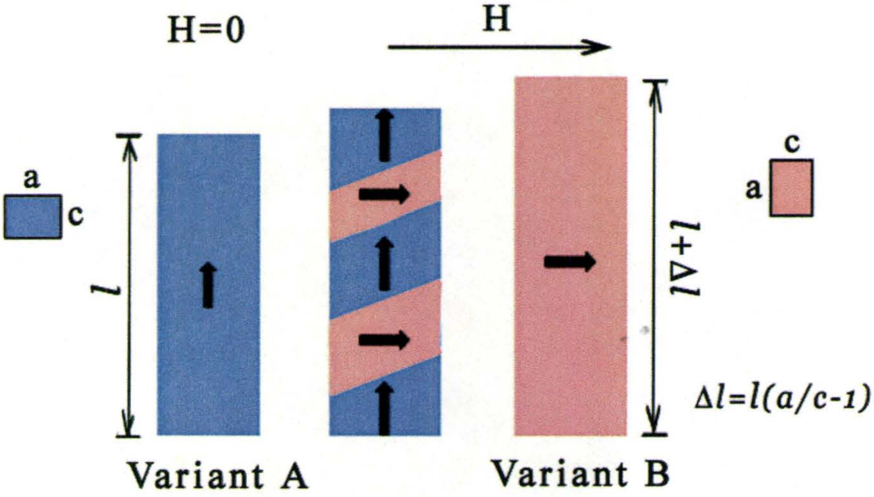

Figure 2.3: Mechanism for the large magnetic field induced strain in ferromagnetic shape memory alloys. The application of a lateral magnetic field converts martensitic Variant A to Variant B and induces an elongation of $\Delta l = (a/c - 1)l$ in the vertical direction. Here a and c are the lattice constants of the unit cell of the martensite and l is the vertical dimension of the crystal. The direction of the external magnetic field and the magnetic easy axes of Variants A and B are denoted by arrows.

2.2 Ni-Mn-Ga Ternary System

In 1984, Webster and co-workers observed a reversible martensitic transformation in a Ni_2MnGa compound which was accompanied by an abrupt change of magnetization (Webster *et al.*, 1984). This discovery allowed for the possibility of achieving SME in this material. Ten years later, Ullakko and his co-workers obtained a strain of 0.2% in an unstressed Ni_2MnGa single crystal using an external magnetic field of 8 kOe (Ullakko *et al.*, 1996). This finding introduced the concept of the ferromagnetic shape memory effect and initiated the intensive studies on Ni-Mn-Ga ternary alloys which followed over the course of the next decade.

2.2.1 Ni_2MnGa Intermetallic Compound

The Ni_2MnGa intermetallic compound is the prototype for the Ni-Mn-Ga ternary alloys. It has been found that all the off-stoichiometric Ni-Mn-Ga alloys that show a shape memory effect have compositions close to Ni_2MnGa. Thus, understanding the crystal structure, phase transformation, and magnetic properties of the stoichiometric Ni_2MnGa compound is helpful when studying the various properties of the non-stoichiometric Ni-Mn-Ga alloys. Therefore, the Ni_2MnGa compound is introduced first in this subsection which is followed by a more general discussion of the Ni-Mn-Ga alloys.

2.2.1.1 Phase Transitions

The melting temperature of the Ni_2MnGa compound is 1382 K (Overholser *et al.*, 1999). Solidified from liquid, the material forms a partially disordered B2' structure. Upon further cooling, it experiences three structural phase transformations. The first one is a disorder-order phase transformation where the partially disordered B2' phase transforms to an ordered austenitic phase at 1071 K (Khovailo *et al.*, 2001). This phase transition is followed by a pre-martensitic transformation at 260 K and a martensitic transformation at 200 K (Khovailo *et al.*, 2001; Brown *et al.*, 2002, 2008). The martensitic phase is stable over a wide range of measured temperatures down to as low as 4 K.

In addition to the structural phase transformations, the Ni_2MnGa compound also undergoes a paramagnetic to ferromagnetic phase transition in the austenitic phase. The Curie temperature is 376 K (Khovailo *et al.*, 2001). The ferromagnetic Ni_2MnGa unit cell has a

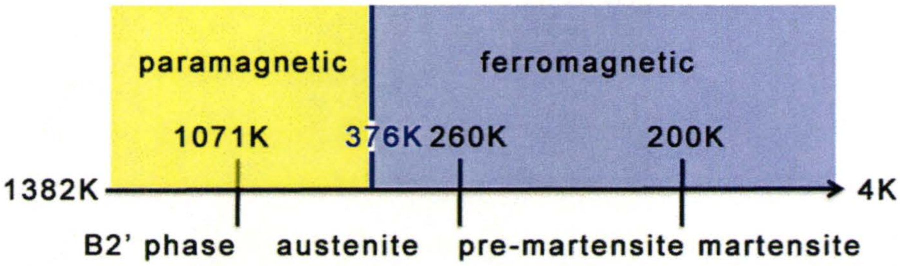

Figure 2.4: Phase transformations in Ni_2MnGa compound.

saturation magnetic moment of 4.05 μB, where the moment is localized primarily on the manganese atoms (Webster *et al.*, 1984; Ayuela *et al.*, 1999; Kulkova *et al.*, 2006) due to the entirely unoccupied manganese spin-down 3d-states (Kubler *et al.*, 1983). The local moments for manganese and nickel are 3.35 μB and 0.35 μB, respectively (Kulkova *et al.*, 2006). The sequence of all phase transformations is plotted on the temperature axis shown in figure 2.4.

2.2.1.2 Crystal Structure

Ni_2MnGa belongs to a group of materials referred to as the Heusler alloys. Its austenitic phase has a cubic $L2_1$ structure with the lattice constant of a=5.82 Å (Brown *et al.*, 2002; Webster *et al.*, 1984; Vasil'ev *et al.*, 2003). The structure, shown in figure 2.5, can be considered as four interpenetrating f.c.c. sublattices each offset by (1/4, 1/4, 1/4) (Webster *et al.*, 1984). Within each f.c.c. sublattice, the nickel atoms are located at the atomic site (0,0,0) and (1/2, 1/2, 1/2) while gallium and manganese atoms occupy the sites (1/4, 1/4, 1/4) and (3/4, 3/4, 3/4), respectively.

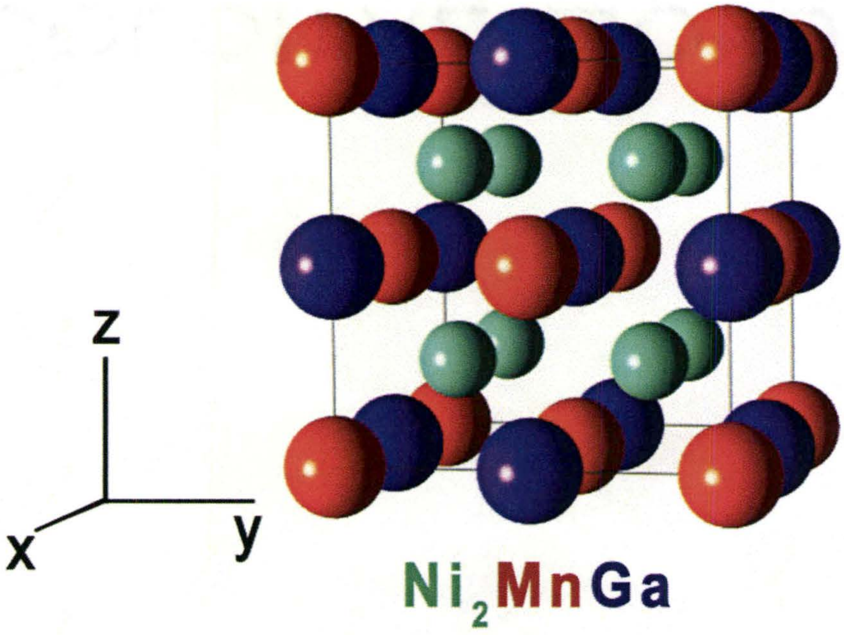

Figure 2.5: Cubic L2_1 structure of the Ni$_2$MnGa austenitic phase. The Ni (cyan), Mn (orange), and Ga (purple) atoms are located at the atomic sites (1/4, 1/4, 1/4), (0, 0, 0), and (1/2, 1/2, 1/2), respectively.

The martensitic phase, which is stable below 200 K, has an orthorhombic crystal structure with a=4.2152 Å, b=29.3016 Å and c=5.5570 Å (Brown *et al.*, 2002). Neutron diffraction reveals that the structure is a superlattice with a 7-fold modulation. The lattice correspondence between the martensitic and the austenitic phases is given as (Brown *et al.*, 2002): $(100)[010]_{\text{martensite}}//(110)[1\bar{1}0]_{\text{austenite}}$, where $a_{\text{martensite}} = \frac{1}{\sqrt{2}}a_{\text{austenite}}$ and $b_{\text{martensite}} = \frac{7}{\sqrt{2}}b_{\text{austenite}}$. Figure 2.6 shows the orthorhombic unit cell of the 7-layer martensite and figure 2.7 illustrates the lattice correspondence between the martensitic and the austenitic phase.

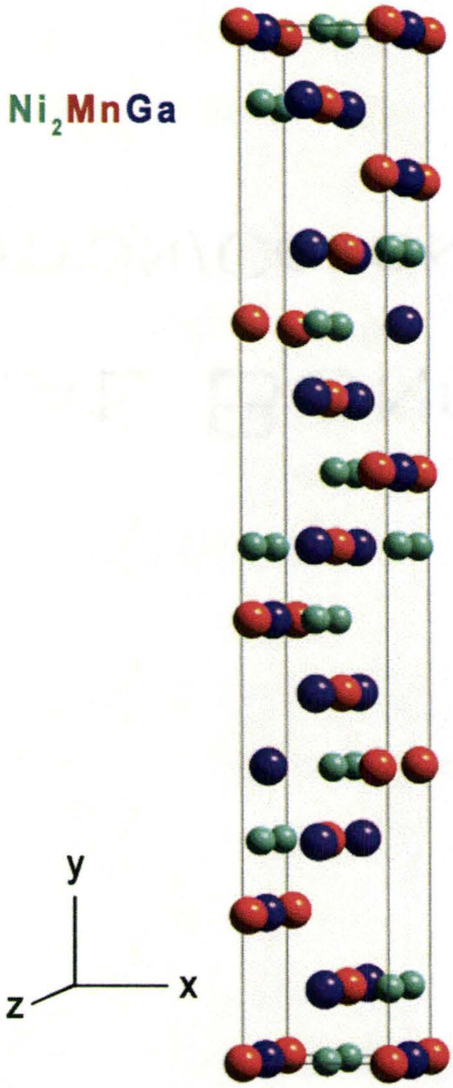

Figure 2.6: Crystal structure of the Ni_2MnGa martensitic phase, showing an orthorhombic unit cell. The Ni, Mn, and Ga atoms are depicted in cyan, orange, and purple, respectively.

A precursor phase has been observed in the temperature range of 200∼260 K which occurs before actual martensitic transformation. Associated with this premartensitic transformation is a superlattice structure which shows a 3-fold stacking periodicity along the b-axis (Brown *et al.*, 2002). The lattice correspondence between the austenitic and the pre-

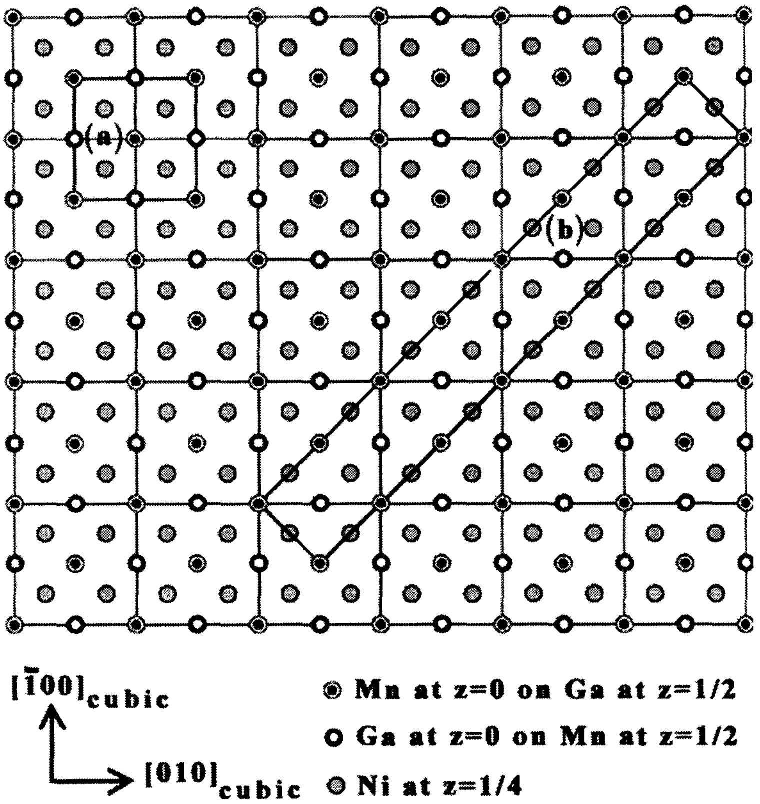

Figure 2.7: Lattice correspondences between the (a) austenitic and (b) martensitic phase for the Ni_2MnGa compound as projected from the cubic [001] direction. Miller indices at the lower left corner show the orientation of the cubic austenitic phase (Adapted from Brown *et al.* (2002)).

Table 2.1: Crystal structure and the temperature range where the various phases exist for Ni_2MnGa compound.

Phase	Temperature range	Crystal structure	Lattice parameter (Å)
austenite	260-1071 K	Cubic $L2_1$	a=5.825 *
pre-martensite	200-260 K	Orthorhombic (3-fold modulation)	a=4.119, b=12.357, c=5.825**
martensite	4-200 K	Orthorhombic (7-fold modulation)	a=4.2152, b=29.3016, c=5.5570***

*(Webster *et al.*, 1984) **(Brown *et al.*, 2008) ***(Brown *et al.*, 2002)

martensitic phase is $a_{\text{ortho}} = \frac{1}{\sqrt{2}}a_{\text{cubic}}$, $b_{\text{ortho}} = \frac{3}{\sqrt{2}}b_{\text{cubic}}$, $c_{\text{ortho}} = c_{\text{cubic}}$. The crystal structure and the temperature range of each phase is summarized in table 2.1.

2.2.2 Ni-Mn-Ga Alloys with Off-Stoichiometry Composition

Due to the wide range of accessible compositions, the physical properties of the off-stoichiometric Ni-Mn-Ga alloys are more complicated than the prototypical Ni_2MnGa compound. However, predicting the main properties for a given alloy composition is still possible since many of the properties are dependent upon the valence electron concentration (e/a), i.e. the number of valence electrons per formula unit divided by the number of atoms. For Ni-Mn-Ga alloys, the e/a ratio is calculated using the following electronic configurations: Ni ($3d^8 4s^2$), Mn ($3d^5 4s^2$), and Ga ($4s^2 4p^1$). These give rise to 10, 7, and 3 valence electrons for Ni, Mn, and Ga, respectively (Chernenko, 1999; Jin *et al.*, 2002; Tsuchiya *et al.*, 2000).

2.2.2.1 Dependence of Martensitic Transformation on Valence Electron Concentration

Experimental observations reveal that the martensitic transformation temperature (i.e. the M_s temperature) deviates substantially with the alloy composition (Tsuchiya *et al.*, 2000). Analysis of the data in terms of valence electron concentration (e/a) reveals that the M_s temperature is nearly a linear function of the e/a ratio (Chernenko *et al.*, 2002; Chernenko, 1999; Jin *et al.*, 2002; Vasil'ev *et al.*, 1999), as shown in figure 2.8 and 2.9. Jin *et al.* (Jin *et al.*, 2002) established an empirical formula for the M_s temperature using the atomic

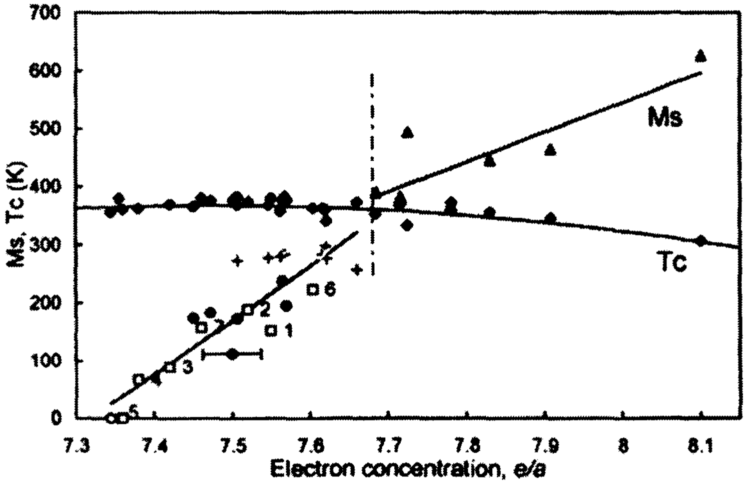

Figure 2.8: Valence electron concentration (e/a) dependencies of the martensitic transformation temperature (M_s) and Curie temperature (T_c) for $Ni_{2+x+y}Mn_{1-x}Ga_{1-y}$ alloys (Chernenko, 1999). The diamonds represent the T_c temperature while all the other symbols correspond to the M_s temperature.

percentage of manganese and gallium: M_s=1960-21.1Mn%-49.2Ga%. The formula makes it possible to design a Ni-Mn-Ga alloy which functions at a chosen working temperature, i.e. the M_S temperature. It has also been pointed out that the martensitic transformation temperature can be further tuned by adjusting the preparation route through alteration to such variables as annealing or deformation procedure (Soderberg *et al.*, 2008).

2.2.2.2 Composition Dependence of the Ferromagnetic Transition

Unlike the martensitic transition temperature, the Curie temperature (T_c) is not strongly dependent upon the composition and e/a ratio (Vasil'ev *et al.*, 2003; Chernenko, 1999). As is shown in figure 2.8, the T_c temperature is nearly constant in the e/a interval of $7.3 \leq e/a \leq 7.6$,

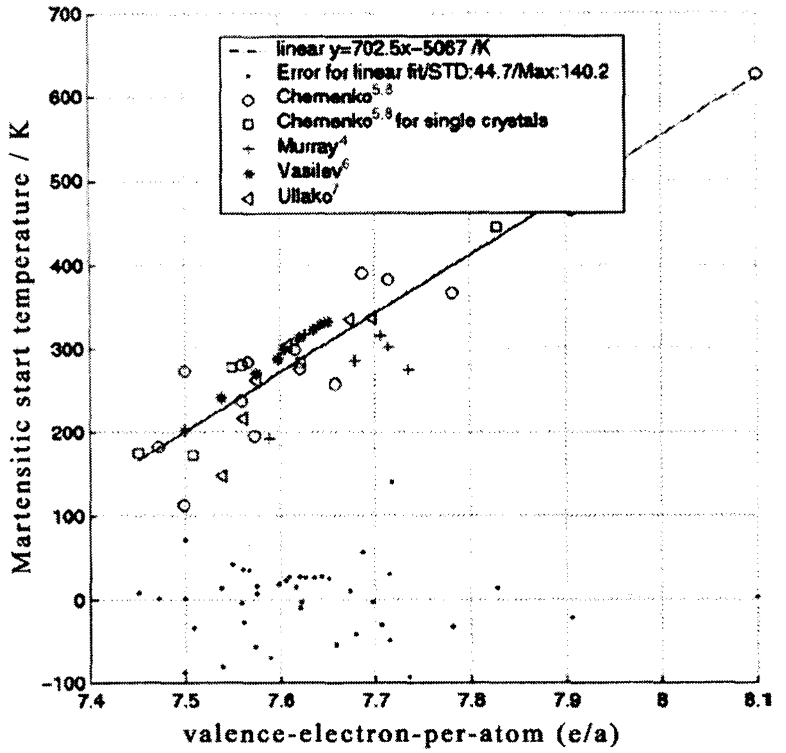

Figure 2.9: Relationship between the martensitic transformation temperature (M_s) and the valence electron concentration (e/a) based on a linear regression: M_s=702.5(e/a)-5067 K (Jin *et al.*, 2002)

whereas it slightly decreases at higher e/a values. Jin *et al.* (Jin *et al.*, 2002) examined a variety of compositions and found that the T_C temperature is relatively stable over a wide range of compositional variation (i.e. Mn: 20~35 at.%, Ga: 16~27 at.%).

Systematic characterization of the phase transformations in two composition series $Ni_{2+x}Mn_{1-x}Ga$ ($0<x\leq0.2$) and $Ni_{2-x}Mn_{1+x/2}Ga_{1+x/2}$ ($0<x\leq0.1$) indicates that any Ni-Mn-Ga alloys having a composition deviating from the stoichiometric composition will show a Curie temperature which is lower than that for the Ni_2MnGa compound (Vasil'ev *et al.*, 1999; Bozhko *et al.*, 1999; Wang *et al.*, 2001b). When Ni is substituted for Mn the saturation magnetization decreases due to the magnetic dilution effect as well as a weaken-

ing of Mn-Mn exchange interaction caused by the increased Mn-Mn distance (Wang *et al.*, 2001b). While Mn replaces Ni or Ga, the nearest Mn-Mn distance in the off-stoichiometric Ni-Mn-Ga alloys is shorter than that in Ni_2MnGa compound. This induces an antiferromagnetic coupling among the neighboring Mn atoms, and thus, also deteriorates the ferromagnetism (Kanomata *et al.*, 1987; Wang *et al.*, 2001b). It has been found that the T_c temperature decreases at a lower rate in the $Ni_{2-x}Mn_{1+x/2}Ga_{1+x/2}$ system as compared to the $Ni_{2+x}Mn_{1-x}Ga$ series, a response indicative of the conduction electrons provided by Ga and Ni also playing an important role in determining the magnetic properties (Wang *et al.*, 2001b).

The existence of both a structural and a magnetic transition enriches the nature of the magnetic and magnetoelastic phenomena for the Ni-Mn-Ga alloys. Specific physical behaviours for a given alloy composition depends to a large extent on which transformation occurs first. Since the transformation temperature for both transitions are dependent upon the valence electron concentration, Chernenko *et al.* (Chernenko, 1999) classified the Ni-Mn-Ga alloys of various compositions into three categories according to their e/a ratio, where the sequence of the two phase transformations varies for each category. As shown in figure 2.8, for small e/a ratios (i.e. $e/a<7.7$) the martensitic transformation temperature is far below the Curie temperature while the reverse tendency occurs for larger ratios (i.e. $e/a>7.7$). The two transitions overlap within the intermediate range (i.e. $e/a\approx7.7$). The above behaviours are corroborated by the experimental observation of Borisenko et al. (Borisenko *et al.*, 2005) who pointed out that the martensitic transformation takes place in the ferromagnetic state for $e/a<7.6$ and in the paramagnetic state for $e/a>7.7$, as shown in the Ni-Mn-Ga ternary phase diagram (figure 2.10).

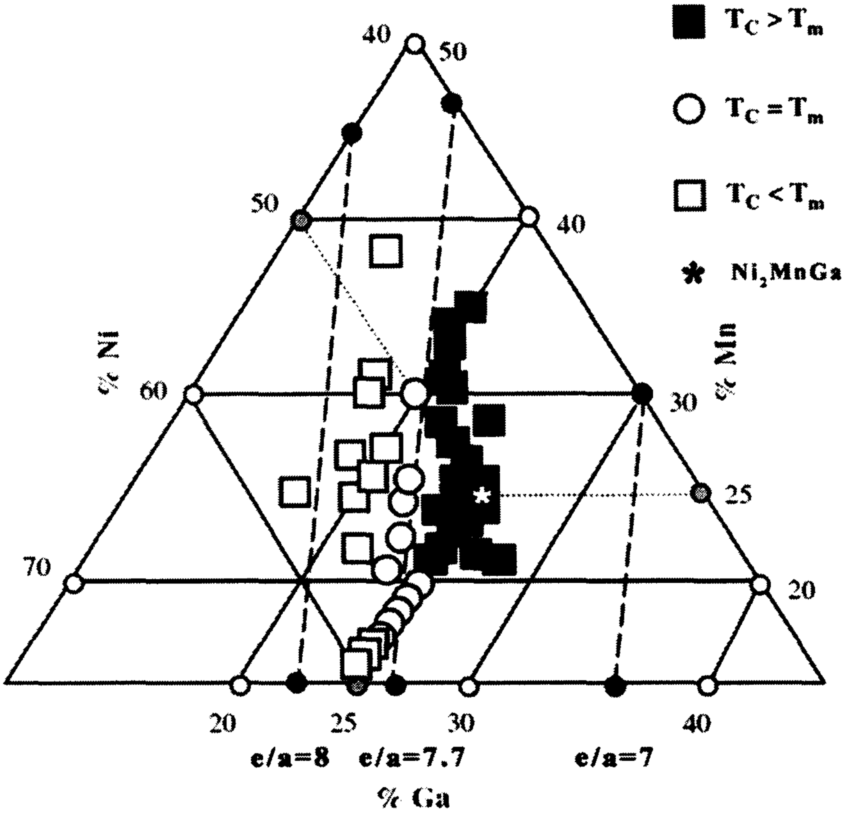

Figure 2.10: Ternary phase diagram of Ni-Mn-Ga alloys showing three distinctive regions where the martensitic transformation takes place above, close to, and below the ferromagnetic ordering temperature (Borisenko *et al.*, 2005)

As a final note, it is pointed out that the Curie temperature could be different for the austenitic and martensitic phase due to the difference in the intensity of the spin interaction stemming from the various interatomic distances in the two crystal structures (Chernenko *et al.*, 2003).

2.2.2.3 Magnetic Properties

As mentioned in Section 2.1.3, a large magnetocrystalline anisotropy is a prerequisite for attaining the magnetic shape memory effect. The magnetization in a magnetic material prefers to lie along a particular crystallographic axis (i.e. magnetic easy axis). It is, thus, easy for the material to be magnetized if the external magnetic field is applied along this axis. Magnetizing the material from all other directions will be more difficult than from the direction of the easy axis. Magnetocrystalline anisotropy is the energy density needed to align the magnetization from the non-easy to easy axis. It arises from the interaction between the spins and the crystal lattice and thus is different for different crystal structures.

The ferromagnetic austenite has three equivalent magnetic easy axes that superimpose on the crystallographic <100> directions. The martensitic phase, however, has only one easy magnetization axis that, in most cases, points along the [001] direction of the lattice (Webster *et al.*, 1984). However, it has also been reported that the martensite crystal having a 2-fold modulation shows a [100] oriented easy-axis (Okamoto *et al.*, 2006). The martensite, thus, has a much larger magnetocrystalline anisotropy, a value two orders of magnitude higher than that of the austenite (Tickle & James, 1999). The value of the magnetocrystalline anisotropy for the martensitic phase is usually obtained experimentally by estimating the area enclosed by the two magnetization curves measured along the easy and hard magnetic axes, respectively (i.e. along the crystallographic [001] and [100] directions, respectively) (Okamoto *et al.*, 2006; Tickle & James, 1999). A typical value of 10^5 J/m^3 has been reported for martensite having various compositions and structures (Okamoto *et al.*, 2006; Tickle & James, 1999; Heczko *et al.*, 2000; Shanina *et al.*, 2001; Albertini *et al.*, 2001; Heczko *et al.*, 2002). The magnetocrystalline anisotropy is a function of tempera-

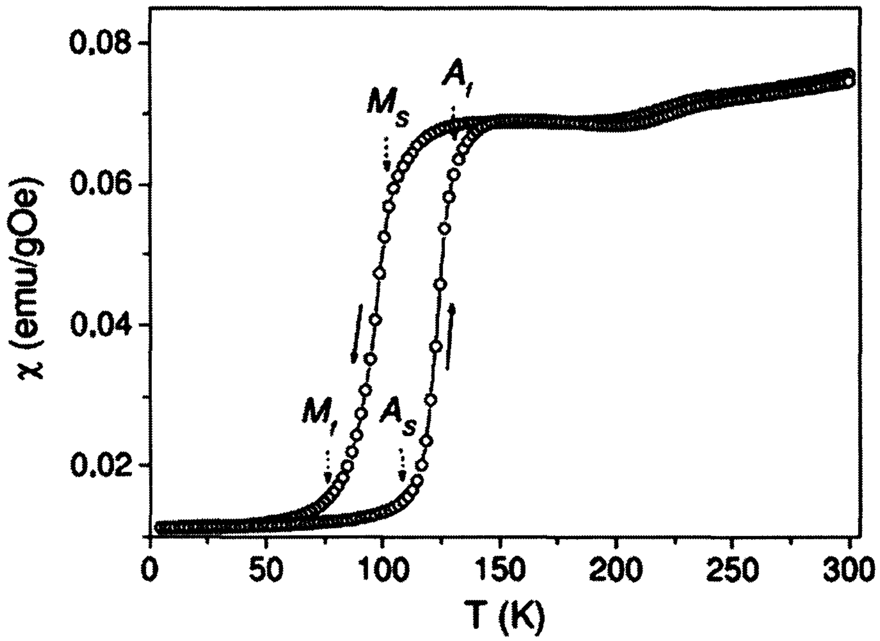

Figure 2.11: Temperature dependence of the AC magnetic susceptibility, χ, for a polycrystalline $Ni_{49.7}Mn_{24.1}Ga_{26.2}$ alloy. The drop in the susceptibility at the onset of the martensitic phase transformation is due to the higher magnetocrystalline anisotropy of this phase (Gomez-Polo *et al.*, 2009). The data plotted is the real part of the AC susceptibility.

ture, which increases as the temperature is lowered (Okamoto *et al.*, 2006; Heczko *et al.*, 2002).

Due to a larger magnetocrystalline anisotropy, the martensitic phase is more difficult to magnetize under a weak magnetic field than the austenitic phase. Figure 2.11 shows the temperature dependence of the magnetic susceptibility (Gomez-Polo *et al.*, 2009). The drop of the susceptibility at the onset of the martensitic transformation is associated with the increase in the magnetocrystalline anisotropy in the martensitic phase. In addition to large anisotropy, the martensitic phase has been reported to have a much larger saturation magnetization regardless of the compositions (Zhou *et al.*, 2005a).

2.3 Magnetically Induced Martensitic Variant Reorientation

Magnetically induced martensitic variant reorientation (MIR) is a magneto-mechanical process that depends upon the interplay between the differently oriented martensitic variants in an external magnetic field. In the absence of an external field, the magnetic moments of the martensitic variants are pinned to the easy magnetization axis which, in many cases, is the short c-axis of a tetragonal or orthorhombic unit cell (Pasquale, 2003; Jiang *et al.*, 2002). When a magnetic field is applied, the moment of each variant tends to align with the field to reduce the Zeeman energy, $E_{\text{Zeeman}} = \overline{M} \cdot \overline{H}$. The alignment is achieved through the growth of the variants whose easy magnetization axis is close to the field direction at the expense of their twin-related counterparts by means of twin boundary motion. The motion occurs when the magnetic field strength reaches a critical value where the variation in the magnetic energy between differently oriented twin variants exceeds the mechanical energy needed for the displacements of the atoms in the vicinity of the twin boundary (Ullakko *et al.*, 1996). To activate such a process, two conditions have to be satisfied: (i) a strong magnetocrystalline anisotropy and (ii) a low twinning stress. The first condition ensures the pinning of the magnetic moment of an individual variant to the magnetic easy axis. The second condition, combined with the first one, ensures that the twin boundary motion is activated in a moderate field which is much smaller than that needed for the alignment of the magnetic moment solely by moment rotation. Further evidence has shown that the twin boundary motion is energetically more favourable than the magnetic domain wall movement since the latter has been found to be absent during the MIR process (Lai *et al.*, 2007). For single crystals, a single variant state can be obtained at the end of the process, which is retained even after the field is removed.

This reorientation process can give rise to both an abrupt increase in the magnetization and shape changes (Heczko, 2005). Figure 2.12 shows a typical magnetization loop together with a strain-field curve of a Ni-Mn-Ga martensite single crystal undertaking the MIR process. Before the magnetization measurement, the sample is loaded under a vertical stress to form a single variant state with the magnetization (or the crystallographic c-axis) pointing to the vertical direction. Application of a lateral magnetic field with increasing strength initially causes the magnetization of the variant to deviate from the easy axis and then initiates the MIR process when the field strength reaches a critical value, H_{MIR}. At this critical activation field, the magnetic energy exceeds the elastic energy associated with the twin boundary motion. The excess energy drives the nucleation of new variants in the material, which form a twin-relationship with the original variant. The easy magnetization axis (i.e. crystallographic c-axis) of the newly generated variants is along the external magnetic field direction, which is orthogonal to the c-axis of the initial variant. The growth of the newly formed variants results in an abrupt increase in magnetization due to the high degree of alignment of the magnetization of the new variants with the field. As shown in figure 2.12, a magnetization increment (ΔM) of about 50% of the saturation magnetization has been induced in the MIR process. Simultaneously observed is a strain of 5.5% generated in the vertical direction, which is attributed to the mechanism described in Section 2.1.4. For the subsequent reduction of field strength, the magnetization reversal does not follow the initial path, but instead takes the path where the easy magnetization axis aligns in the direction of the field. This indicates that the sample retains the structure after reorientation, which does not change when subjected to an inverse magnetic field as shown in the third and second quadrant of the magnetization and strain curve, respectively.

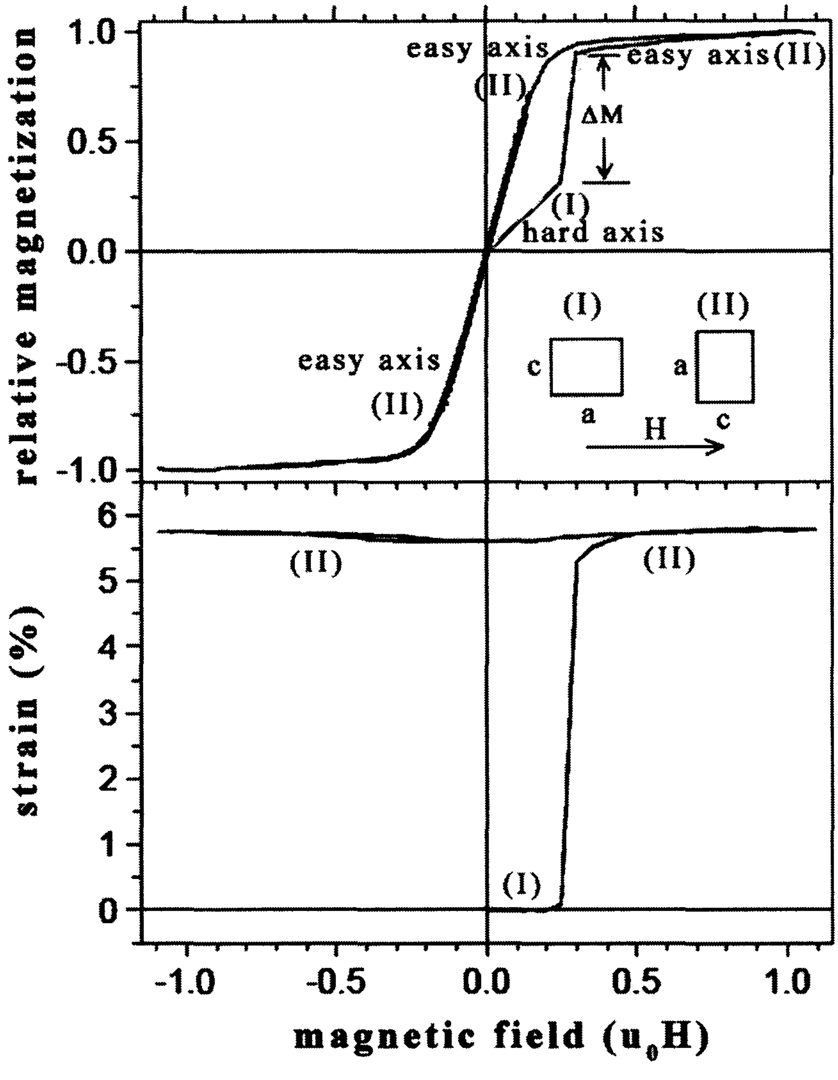

Figure 2.12: Typical magnetization loop (top) together with a strain-field curve (bottom) for a Ni-Mn-Ga martensite single crystal undergoing the MIR process. The magnetization takes the path with the hard and easy magnetization axis before and after the MIR process, respectively, which gives rise to a magnetization increment of ΔM. The unit cell of the initial and newly generated variants with respect to the magnetic field direction are depicted and labeled as (I) and (II) in the magnetization and strain curves (Heczko, 2005; Wilson *et al.*, 2007).

To obtain a fully reversible strain, a compressive restoring force has to be applied orthogonal to the field direction (Heczko, 2005). Such a stress can nucleate the original variant with the c-axis in the stress direction and cause a drop in both magnetization and strain. The magnitude of the restoring force is required to be larger than the twinning stress, but smaller than the stress exerted by the magnetic field (Straka & Heczko, 2006). If the force is low compared to the twinning stress, the reverse MIR is partially fulfilled and the sample contains variants with c-axis along both vertical and lateral directions at zero field. When the field is applied in the opposite direction, only those variants whose c-axes are perpendicular to the field experience the MIR effect while those with c-axes parallel to the field are unaffected. This results in a smaller magnetization hysteresis and less strain. When the external force is higher than the stresses exerted by the magnetic field, the field-favourable variants are not able to nucleate. As a consequence, the MIR process is suppressed. The three cases are illustrated in figure 2.13 where the sample shows a fully reversible, partially reversible, and absent MIR effect under a 1.4 MPa, 0.6 MPa, and 3 MPa compressive stress, respectively. Of note is the fact that even for a fully restored MIR process, hysteresis has been observed in the activation fields between the magnetizing and demagnetizing processes, bringing extra hysteresis in both magnetization and strain curves. The source of the hysteresis can be understood from the following inequalities:

$$\sigma_{mag}^{MIR} \geq \sigma_{tw} + \sigma_{ext} \tag{2.1a}$$

$$\sigma_{ext} \geq \sigma_{mag}^{Reverse-MIR} + \sigma_{tw} \tag{2.1b}$$

Here σ_{mag}^{MIR} and $\sigma_{mag}^{Reverse-MIR}$ are the stresses exerted by the magnetic field in the forward and reverse MIR processes, which are proportional to the magnetic field strength. σ_{tw} and σ_{ext} are the twinning and external restoring stresses, which do not depend upon the magnetization path. Inequality (2.1a) is responsible for the forward MIR process where the magnetic force has to be large enough to overcome the twinning and the external stresses to activate the MIR process. Inequality (2.1b) describes the reverse MIR process in which a large external stress is needed to nucleate and enlarge the variants whose c-axes are orthogonal to the magnetic field. Rewriting the above inequalities one obtains:

$$\sigma_{mag}^{MIR} \geq \sigma_{tw} + \sigma_{ext} \tag{2.2a}$$

$$\sigma_{mag}^{Reverse-MIR} \leq \sigma_{ext} - \sigma_{tw} \tag{2.2b}$$

It is apparent from inequalities (2.2a) and (2.2b) that $\sigma_{mag}^{Reverse-MIR}$ is smaller than σ_{mag}^{MIR}, a situation indicative of a lower magnetic field strength for the reverse MIR compared with the forward MIR and, thus, a hysteresis between the two processes.

It has also been determined that the minimum magnetic field required to activate the MIR process increases with decreasing temperature and that the MIR effect can only occur in a limited temperature range (Pasquale *et al.*, 2002; Liu *et al.*, 2002; Heczko & Straka, 2003; Peterson *et al.*, 2008; Wang *et al.*, 2001a). Liu *et al.* (Liu *et al.*, 2002) reported a MIR effect for $Ni_{50}Mn_{27.5}Ga_{22.5}$ (at.%) for temperatures as low as 166 K while Cui *et al.* (Cui *et al.*, 2005) observed a magnetically induced actuation for a Fe-doped Ni-Mn-Ga alloy in the temperature range of 100∼265 K. These observations indicate decreased twin boundary mobility at low temperatures due to the augmented twinning stress and weakened thermal activation (Heczko & Straka, 2003; Straka *et al.*, 2006; O'Handley *et al.*, 2006). Heczko and Straka argued that the influence from the other temperature dependent magnetic and elastic properties, such as tetragonality (c/a) and the anisotropy constant (K_u), are of less significance (Heczko & Straka, 2003; Straka *et al.*, 2006).

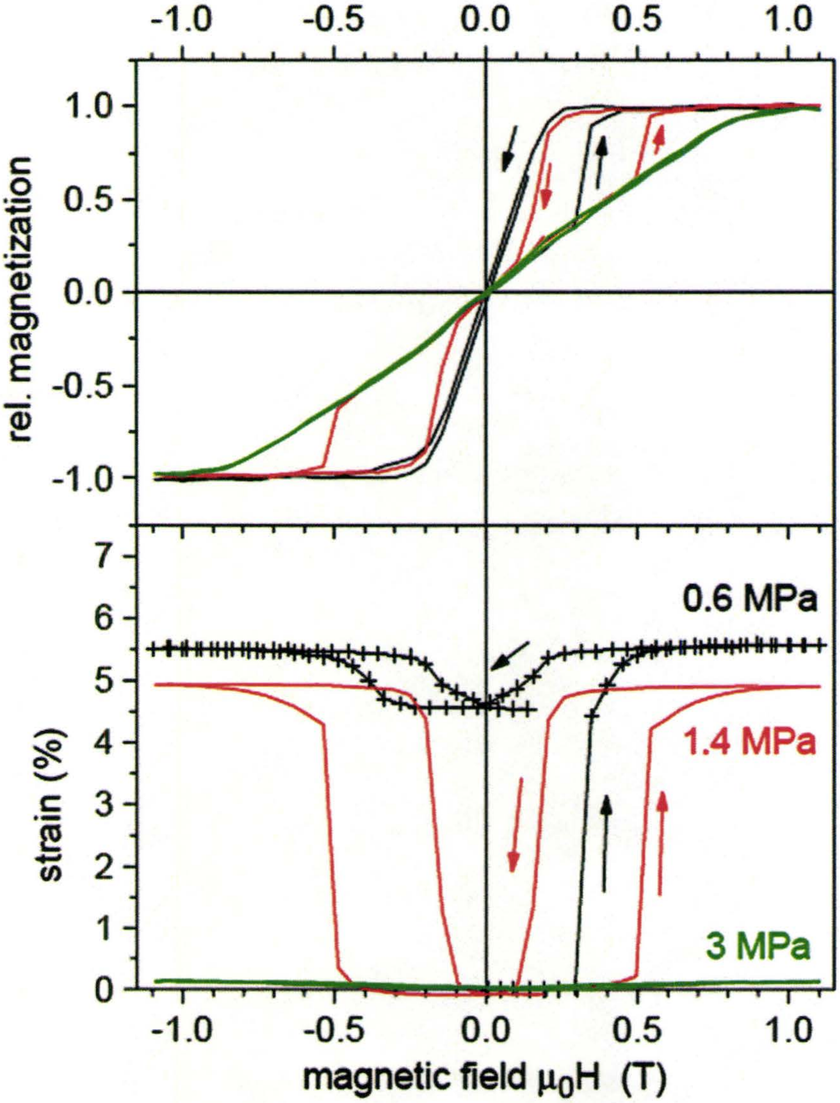

Figure 2.13: Magnetization loops and field-induced strain for a Ni-Mn-Ga martensite single crystal under various loads at room temperature. The sample goes through a partially reversible, fully reversible, and the absence of a MIR process for the 0.6 MPa (black), 1.4 MPa (red), and 3 MPa (green) external restoring stresses, respectively. The sense of application and removal of the magnetic field is denoted by the arrows (Heczko, 2005).

2.4 Magnetocaloric Effect

The magnetocaloric effect (MCE) is a phenomenon related to the change of entropy and temperature of a solid due to a varying magnetic field, which is usually used to reach low temperatures in a condition of adiabatic demagnetization. The effect is intrinsic to any magnetic material but is more pronounced in ferromagnets. Adiabatic application of a magnetic field to an isolated ferromagnet aligns the spins in the magnet and, thus, reduces the magnetic entropy. Since the entropy of an isolated system has a constant value, the drop in the magnetic entropy is compensated for by an increase in the lattice entropy. On the contrary, adiabatic removal of the magnetic field increases the magnetic entropy but decreases the lattice entropy, resulting in a drop in the magnet's temperature.

Two processes will occur when a magnet is subjected to a magnetic field with varying strength: an adiabatic temperature change and an isothermal entropy change (Gschneidner & Pecharsky, 2000). Both occur at a constant pressure and are involved in a full refrigeration cycle (see figure 1.2 in Chapter 1). The first process occurs for an isolated magnet where the total entropy remains constant when the magnetic field is altered. The adiabatic temperature change of the magnet is then characterized as:

$$\Delta T_{ad}(T)_{\Delta H} = (T(S)_{H_F} - T(S)_{H_I})_S \tag{2.3}$$

Where $T(S)_{H_F}$ and $T(S)_{H_I}$ are the temperature of the magnet at the initial and final magnetic field, respectively.

During the second process the magnet is connected to an outside environment and stays at a constant temperature when the magnetic field changes from the initial field strength to the final strength (i.e. from H_I to H_F). The magnetic entropy change resulting from this process is defined as:

$$\Delta S_M(T)_{\Delta H} = (S(T)_{H_F} - S(T)_{H_I})_T \tag{2.4}$$

where $\Delta H = H_F - H_I$ is the change in the magnetic field strength and $S(T)_{H_F}$ and $S(T)_{H_I}$ are the initial and final magnetic entropy of the magnet. The total heat transfer, q, between the cold and hot ends of a refrigerator is, thus, calculated as:

$$q = -\int_{T_1}^{T_2} \Delta S_M(T)_{\Delta H} dT \tag{2.5}$$

where T_1 and T_2 correspond to the temperatures of the cold and hot ends, respectively. The negative sign before the integral indicates that the heat is transferred from the hot end to the cold end.

In terms of the experimental measurements, the adiabatic temperature change ΔT_{ad} is measured directly while the isothermal entropy change ΔS_M is usually estimated from the magnetization isotherms using Maxwell relation (Morrish, 1965):

$$(\frac{\partial S_M(T,H)}{\partial H})_T = (\frac{\partial M(T,H)}{\partial T})_H \tag{2.6}$$

which after integration gives (Pecharsky & Gschneidner, 1999a):

$$\Delta S(T,H)_{\Delta H} = \int_{H_I}^{H_F} (\frac{\partial M(T,H)}{\partial T})_H dH \tag{2.7}$$

For magnetization measurements made at discrete field and temperature intervals, the above equation can be numerically solved using the approximate equation (McMichael *et al.*, 1993):

$$\Delta S(T_0,H)_{\Delta H} \approx \frac{1}{\Delta T}\left[\int_{H_I}^{H_F} M(T_2,H)_H dH - \int_{H_I}^{H_F} M(T_1,H)_H dH\right] \tag{2.8}$$

where the temperature interval ΔT and the average midpoint temperature (T_0) of the interval are given by:

$$\Delta T = T_2 - T_1 \tag{2.9}$$

$$T_0 = \frac{T_1 + T_2}{2} \tag{2.10}$$

From equation (2.8) it is apparent that the entropy change occurring over the ΔT temperature interval, which is assigned to the temperature T_0, is the area between the magnetization isotherms obtained at T_1 and T_2 divided by ΔT.

It is known from the above equations that ΔS_M is a function of temperature and magnetic field change, as well as being material dependent. Since ΔS_M is proportional to the derivative of the magnetization with respect to temperature, i.e. $\frac{\partial M}{\partial T}$ (equation (2.7)), the largest magnetic entropy change is usually observed in the vicinity of the magnetic ordering where the magnetization is changing rapidly with temperature. This is the reason why most ferromagnetic materials show MCE behaviour when they undergo a ferromagnetic phase transition upon cooling. The effect has also been observed for materials that undergo a first-order structural phase transformation where the high and low temperature phases show different magnetic properties. The MCE could be greatly enhanced if the structural and magnetic phase transitions coexist (Pareti *et al.*, 2003; Long *et al.*, 2005; Khan *et al.*, 2006). This has been shown to be the case for Ni-Mn-Ga single crystals exhibiting a giant

MCE response of $\Delta S=-86$ J/kg-K for $\Delta H=5$ T at 312.75 K (Pasquale *et al.*, 2005).

2.5 Ni-Mn-Ga Thin Films

Since the magnetic field induced strain of 0.2% was first reported in Ni_2MnGa single crystals in 1996 (Ullakko *et al.*, 1996), Ni-Mn-Ga alloys have been intensively studied as magnetic shape memory materials. In order to introduce the magnetic shape memory effect to micro-scale applications considerable efforts have been made to fabricate Ni-Mn-Ga thin films (Ohtsuka & Itagaki, 2000; Wuttig *et al.*, 2000; Isokawa *et al.*, 2001; Tello *et al.*, 2002; Dubowik *et al.*, 2004). Progress in this direction, however, has been slow. Initial efforts resulted in films with poor crystallinity which had no epitaxial relationship with the underlying substrates (Ahn *et al.*, 2001; Golub *et al.*, 2004; Hakola *et al.*, 2004a; Rumpf *et al.*, 2006). The poor quality was attributed to low deposition temperatures ($T \leq 450$ °C) which limited crystallization and grain growth. At high temperatures, the volatility of Mn and Ga led to their preferential loss, giving rise to Ni-rich films.

The first sign of progress was achieved through a deposition pathway where films were produced by a low temperature deposition followed by a high temperature anneal (Chernenko *et al.*, 2005b; Liu *et al.*, 2008). The films prepared using such techniques showed superior magnetic properties and were able to transform between the martensitic and austenitic phase. This early success in film fabrication stimulated an interest in studies of a broad range of films' properties, which included the crystal structure of the martensitic phase (Suzuki *et al.*, 2002), thickness dependence of the martensitic phase transformation (Chernenko *et al.*, 2005b), magnetoresistance (Koike *et al.*, 2007), magnetic domain structure (Chernenko *et al.*, 2005a), magnetic susceptibility (Chernenko *et al.*, 2007), and elastic modulus (Liu *et al.*, 2008). The fabrication of free-standing structures was also made possible by these higher qulity films. The magnetic shape memory effect was observed in a free-standing bridge derived from an epitaxial Ni-Mn-Ga single crystal film (Dong *et al.*, 2004). A microactuator prototype which was designed as a part of a microscanner has been fabricated from the Ni-Mn-Ga free-standing bridges using a micromachining technique (Kohl *et al.*, 2004, 2006; Khelfaoui *et al.*, 2008). These results demonstrate the possibility of fabricating shape memory devices on a micrometer length scale using Ni-Mn-Ga thin films and provide the motivation for optimizing the shape memory effect through improvements to the films properties.

Recently, high temperature *in-situ* deposition was employed to synthesize high quality Ni-Mn-Ga thin films using dc sputtering (Jakob & Elmers, 2007; Porsch *et al.*, 2008; Jenkins *et al.*, 2008) and pulsed laser deposition (Zhang *et al.*, 2009) techniques. Growth temperatures between 500 °C and 650 °C have been applied. The high growth temperatures facilitated the development of films with improved crystallinity and a homogeneous composition (Zhang *et al.*, 2009; Jenkins *et al.*, 2008). The loss of manganese and gallium at high temperatures was compensated for by appropriate enrichments to the target material (Zhang *et al.*, 2009).

Another significant improvement in the development of the functional properties of the Ni-Mn-Ga films was achieved in terms of the effect of the magnetic field induced martensitic variant reorientation (MIR). Very recently, a partial MIR effect was observed in Ni-Mn-Ga polycrystalline films affixed to a rigid substrate (Thomas *et al.*, 2008a; Heczko *et al.*, 2008; Jenkins *et al.*, 2008; Zhang *et al.*, 2009; Buschbeck *et al.*, 2009). This development represents a substantial improvement to the films quality and provides a positive step toward real applications for these materials, since the complex micromachining could potentially be avoided. It has been shown that the MIR phenomenon is reversible (Thomas *et al.*, 2008a; Heczko *et al.*, 2008; Zhang *et al.*, 2009; Buschbeck *et al.*, 2009) where the reversibility is not reliant on an external stimuli. This is in contrast to single crystals, where an external stress applied perpendicular to the magnetic field direction is required to induce the reorientation of twin variants (Murray *et al.*, 2000; Straka & Heczko, 2005; Straka *et al.*, 2006). The critical magnetic field used to activate the effect is only one third the field strength required for single crystals (Heczko & Straka, 2003; Straka *et al.*, 2006). Such a small activation field is attractive from a device perspective, especially in the applications where strong magnetic fields are considered undesirable due to possible interference between the field and the other electronic components. However, the mechanism behind the self-activated reversibility is still the subject of debate. Thomas *et al.* (Thomas *et al.*, 2008a,b) proposed a theory based on the $\{100\}$ oriented orthorhombic Ni-Mn-Ga films. In their theory, the self-reversibility was facilitated by substrate-imposed stresses that developed during the reorientation of the in-plane lattice constants of an orthorhombic unit cell. While this provides an explanation to the $\{100\}$ films, the same description cannot be applied to the behavior observed for the $[101]$ textured films studied in the current thesis project. A detailed discussion of this topic and an alternative mechanism of the MIR effect are provided in Chapter 5.

In summary, ferromagnetic Ni-Mn-Ga shape memory alloys are a group of multifunctional materials. They exhibit a number of peculiar properties which make them attractive candidates for high-frequency actuation-based applications. Ni-Mn-Ga thin films introduce a large number of new possibilities owing to their small length scale. The thin films are more likely to show distinct physical properties than bulk samples since the dimension normal to the surface of the film is significantly less than the biaxial dimensions within the surface. The rest of the thesis will focus on demonstrating the unique nature of Ni-Mn-Ga thin films and providing physical pictures behind these distinctive properties.

Chapter 3

Experimental Methods and Techniques

3.1 Synthesis of Ni-Mn-Ga Thin Films

A number of techniques have been reported within literature for Ni-Mn-Ga film fabrication, including sputtering (Thomas *et al.*, 2008a), pulsed laser deposition (Golub *et al.*, 2004; Hakola *et al.*, 2004a), molecular beam epitaxy (Dong *et al.*, 2000), and flash evaporation (Dubowik *et al.*, 2004). For the current thesis work, the pulsed laser deposition (PLD) technique was applied as it has the advantages of having an accurately controlled growth rate, yielding epitaxially grown films, and allowing congruent transfer of material from target to film.

3.1.1 Deposition Mechanism for the PLD Technique

The elementary physical picture of laser deposition is illustrated in figure 3.1. As the aligned laser beam strikes the target surface the photon energy from the laser pulse is transferred to the kinetic energy of the target's conduction electrons. By electron-phonon interaction, a fraction of the absorbed energy passes to the motion of the atoms or ions in the metallic lattice, causing the target temperature to rise. In the meantime, heat conduction occurs between the surface and the interior of the target. This heated volume has the shape of an elliptical cylinder where the thickness is defined by the thermal diffusion length (L_t) of the metal target and the cross-section is given as the projected area (δA) of the laser beam. If the laser energy is high enough, the solid material within the heated volume melts and evaporates, generating a large pressure gradient. Due to this pressure gradient, the evaporant expands out of the shallow crater at a large flow velocity and forms a plume (Mahan, 2000). The expansion is in the direction normal to the target surface, which is toward the substrate. It ceases at a terminal flow velocity when the density of the plume falls sufficiently. The vapor particles then fly to and condense on the substrate in a style of free molecular flow. The laser pulse may also photoemit electrons from the target surface or photoionize atoms in the plume, giving rise to a plasma.

3.1.2 PLD Instrument

A pulsed laser deposition system is typically made up of five parts: (i) vacuum chamber, (ii) target rotator, (iii) substrate heater, (iv) laser, and (v) laser optics. Background gases are

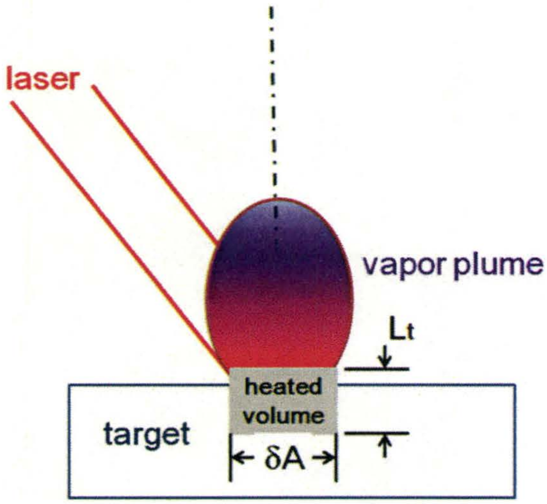

Figure 3.1: An elementary physical picture of laser deposition. A heated volume of size ($\delta A \times L_t$) is generated when a laser pulse strikes the target surface. The solid material within the heated volume melts and evaporates, forming a plume which expends in the direction normal to the target surface (Adapted from (Mahan, 2000)).

often introduced into the chamber during the deposition to either compensate for or reduce the vapour pressure of volatile elements emerging from the surface of the film. The gases can also react with target elements to grow compound thin films. The laser system used in this thesis work is an IPEX-848 excimer laser with a wavelength of 248 nm and a spot size of 2×3 mm^2. The laser lab is affiliated with McMaster University Superconductor Film Group. Figure 3.2 depicts a typical KrF excimer laser system.

3.1.3 Laser Parameters

There are many parameters such as laser fluence, repetition rate, substrate-target distance, and deposition temperature, which can influence the deposition process. Optimization of

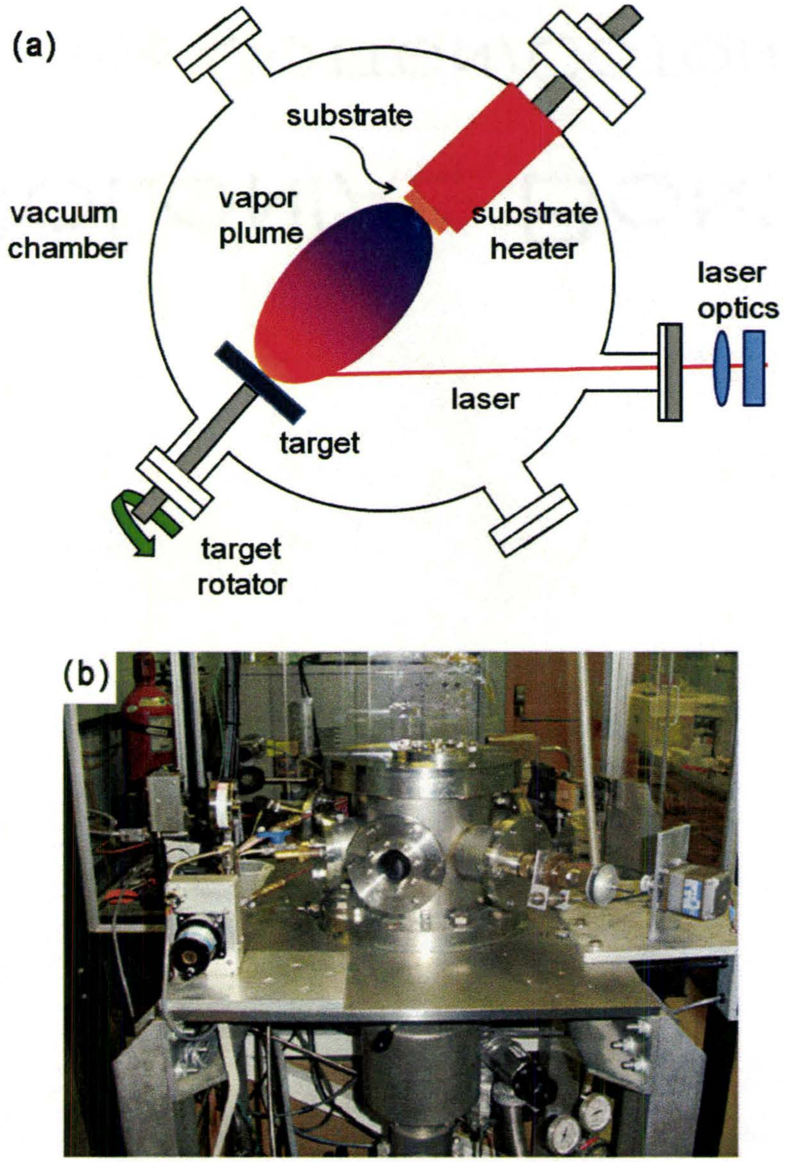

Figure 3.2: (a) Schematic depiction of a pulsed laser deposition system and (b) photograph of the IPEX-848 excimer laser used for Ni-Mn-Ga film growth.

these parameters yields high quality films. A series of deposition temperatures and laser repetition rates have been tested in the current project, through which an optimum experimental condition was attained. The deposition parameters associated with this optimum

Table 3.1: Listing of the deposition parameters used in the current project.

Laser fluence ($J{\cdot}cm^{-2}$)	repetition rate (Hz)	substrate-target distance (mm)	substrate temperature °C
~6	10~13	350	575~650

condition is listed in table 3.1. By using these parameters, a deposition rate of 500 nm h^{-1} or 375 nm h^{-1} has been achieved for films grown on the YSZ or MgO substrate.

3.1.4 Target Development

Laser targets of 1" diameter and 0.25" thickness were prepared (in sample preparation lab affiliated with Brockhouse Institute for Materials Research) through the arc-melting of pure Ni, Mn, and Ga under a protective argon atmosphere. The targets were re-melted several times to improve homogeneity. Figure 3.3 shows the energy dispersive X-ray (EDX) mapping of each constituent element in the prepared Ni-Mn-Ga laser target. The uniform contrast shown in each mapping indicates the uniform spatial distribution of these elements within the target.

During the deposition process, the target surface was vaporized by the high-energy laser beam. To avoid deep cratering at any individual spot, the target was rotated. A progressively deeper circular groove was thus formed over time which led to the deflection of the plasma plume from the vertical path between the substrate and the target, resulting in films with a significant thickness gradient. To avoid this undesirable effect, the target was polished before each deposition. Although the polishing accelerated the erosion of the target material, considerable deposition capacity was still achieved under the current

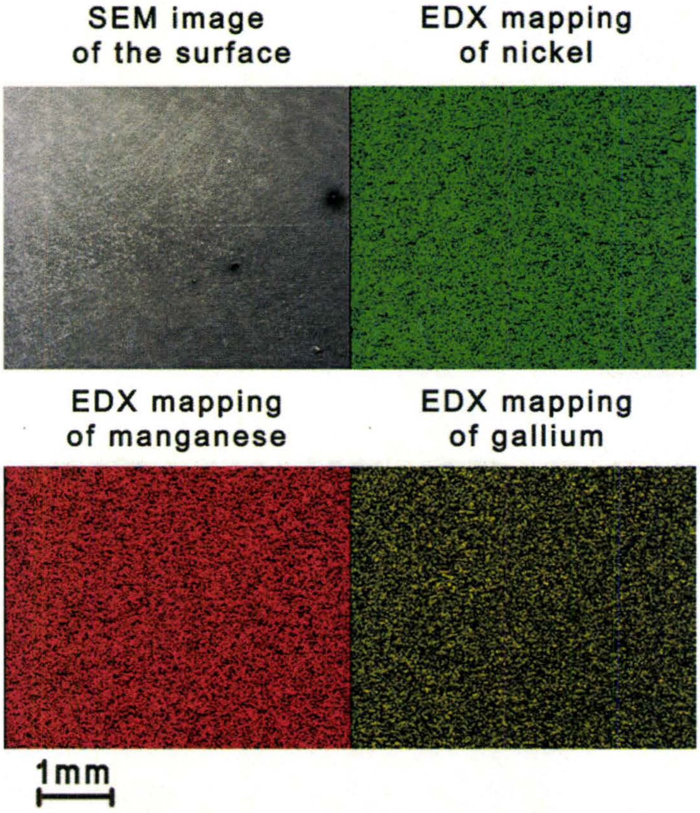

Figure 3.3: SEM image of the surface of the prepared Ni-Mn-Ga laser target and the EDX mapping of each constituent element in the target. The uniform contrast in each mapping indicates the uniform spatial distribution of these elements.

experimental condition, yielding about 200 films per target.

3.2 Thin film Characterization

3.2.1 Phase Identification and Texture Analyses

The crystal structure and texture information are studied with the traditional $\theta - 2\theta$ powder X-ray diffraction technique (XRD) and three-dimensional X-ray diffraction (XRD^3) technique (provided by McMaster Analytical X-ray Diffraction Facility). The $\theta - 2\theta$ XRD is carried out using a Bruker D8 X-ray diffractometer with Cu $K_{\alpha 1}$ radiation. The XRD^3 is performed with a Rigaku RU-200 rotating anode Cu K_{α} x-ray generator, on a Bruker 3-circle D8 goniometer with parallel-focusing mirror optics and a Bruker Smart 6000 CCD detector. -ω and -ϕ scans were used to generate the three-dimensional diffraction pattern. The unit cells of the martensitic and austentic phases were indexed using SMART and RLATT programs from Bruker-AXS (Bruker-AXS, 2009) and the MAX3D (Britten & Guan, 2007) software package. Pole figures were generated with Bruker GADDS (Bruker-AXS, 2009) software.

The principle of the X-ray diffraction is described as follows. When an atom is impacted by an X-ray beam, the electrons around it will oscillate with the same frequency as the incoming X-ray beam, which gives rise to electron waves occurring in various directions. These waves interfere destructively in nearly all directions and will not leave the solid sample. However, since the atoms in a crystalline sample are arranged in a regular pattern, there are several directions where the electron waves can have constructive interference. A large number of the mutually reinforced rays combine into what is called a diffracted beam. The diffracted beam contains the information of the atomic arrangement

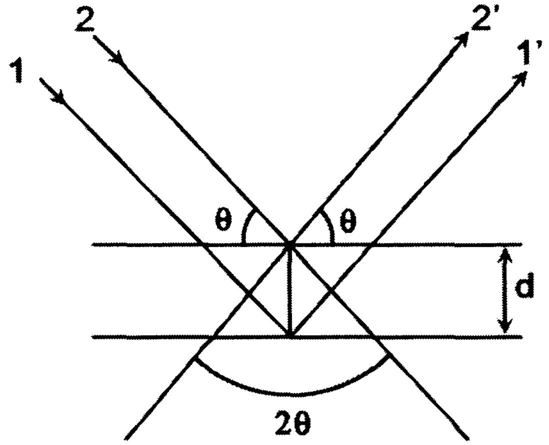

Figure 3.4: Diffraction of X-rays by a crystal at the Bragg condition

in a crystal since it is built up of rays scattered by atoms of the crystal that lie in the path of the incident X-ray beam.

This physical mechanism can be described with *Bragg's law*. The X-ray beam, represented by rays 1 and 2 in figure 3.4, incidents on a pair of parallel planes separated by an interplanar spacing, d. The diffracted beam results only when the angle between the reflected beam and the transmitted beam is twice the incident angle, θ. That is, the incident angle has to satisfy the following relationship:

$$2dsin\theta = n\lambda \tag{3.1}$$

where λ is the wavelength of the incident X-ray beam and n is an integer number. At this condition, the two reflected rays 1' and 2' are completely in phase. *Bragg's law* is the basis of the $\theta - 2\theta$ powder XRD technique.

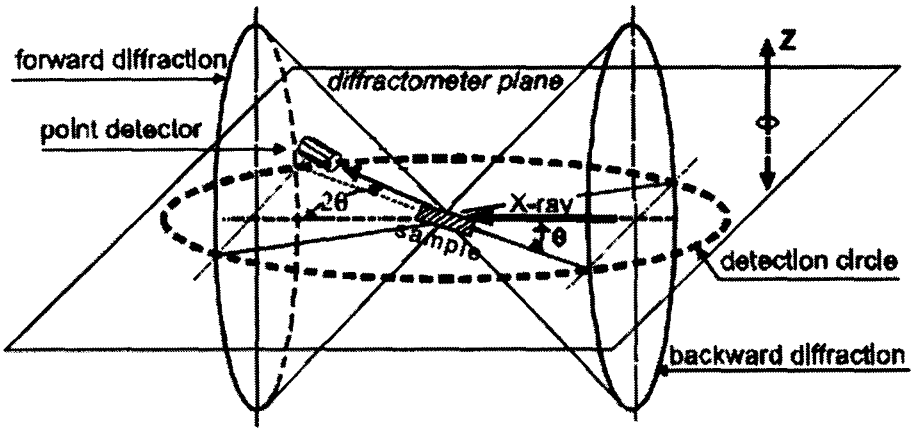

Figure 3.5: Schematic of a $\theta - 2\theta$ setup associated with the powder diffraction equipment (adapted from (Bruker-AXS, 1999)).

In terms of the $\theta - 2\theta$ XRD technique, the X-ray tube is stationary while the sample and detector moves by the angle θ and 2θ, respectively (figure 3.5). A diffraction spectrum is formed from the measured X-ray signals. It consists of a plot of the reflected intensities (I) versus detector angle (2θ). The 2θ value is determined from the shape and size of the unit cell, while the intensities of the reflections depend on the type and location of the atoms in the unit cell. Thus, the crystallographic information of the specimen can be determined exclusively from the I versus 2θ plot.

Although the powder XRD is ideal for characterization and identification of the polycrystalline samples, it gives limited information on single crystals or the highly textured specimens. This is because in powder diffraction, only crystallites having reflecting planes parallel to the specimen surface will contribute to the reflected intensities. For a powder specimen, this is not a problem since all the crystallites are randomly distributed. Each possible reflection from a given set of atomic planes will have an equal probability to be parallel to the sample surface. It is thus possible to detect all the likely reflections. However, for a single crystal, there is only one set of atomic planes that are parallel to the sample surface. Therefore, the powder X-ray spectrum cannot be used as the "finger print identification" for a single crystal specimen. A similar situation is applied for the epitaxial films where all the grains grow along the films' surface normal. In this case, the films are more like a single crystal. Their $\theta - 2\theta$ X-ray spectra contain only information of one set of atomic planes that are parallel to the films' surface.

To circumvent this problem, texture analyses with the help of XRD^3 technique were carried out. For the XRD^3 technique, the area detector is not confined to the diffractometer plane as the case for point detector (figure 3.5), but intersects the diffraction cone to form a conic section as shown in figure 3.6. Therefore, the diffraction data out of the diffractometer plane can also be detected, which are defined by an angle, χ. The rotational scan associated with a two-dimensional area detector, thus, provides a three-dimensional crystallographic information of the material, which is precise enough to determine the structure and texture of the specimen.

The texture is usually described by means of a pole figure which is generated by integrating the diffraction intensity of a given reflection (constant 2θ) at a large number of different angular orientations of the specimen. It is plotted as a contour map of the intensity as a function of the specimen's angular orientation. Since the intensity of a pole (h k l) is proportional to the number of the (h k l) planes in the reflecting condition, the pole figure gives the probability of finding a given crystal plane in a certain specimen orientation.

The radial angle, α, of an (h k l) pole is defined as the angle between the normal to the reflecting plane (h k l) and a physical reference plane in the sample which, in most cases,

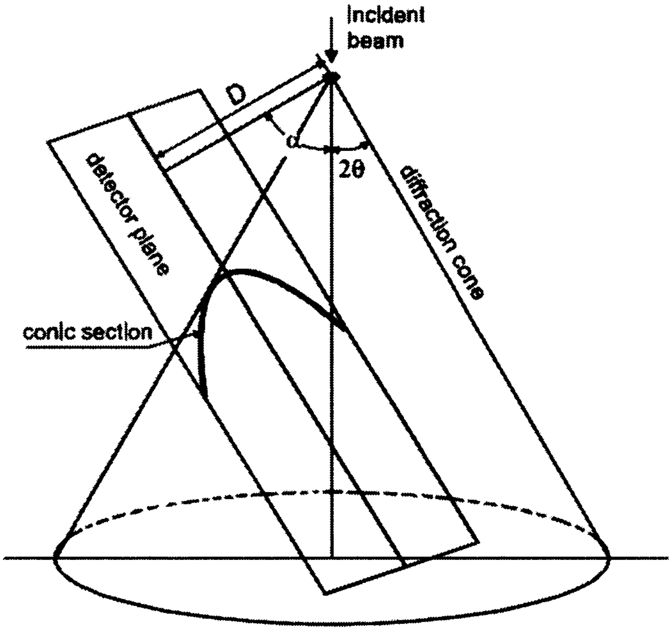

Figure 3.6: Schematic of the detector plane of an area detector. The detector plane intersects the diffraction to form a conic section (adapted from (Bruker-AXS, 1999)).

is the surface plane. The azimuthal angle, β, of an (h k l) pole refers to the angle between the normal to the (h k l) plane and a second reference direction. Figure 3.7(a) illustrates the definition of the radial and azimuthal angle in a pole figure. Figure 3.7(b) shows how an (h k l) plane in a given crystallite is represented in a pole figure. The plane normal is projected onto the pole sphere around the crystallite and intersects the sphere at point A. The connection between the intersecting point A and the south pole will intersect the equatorial plane at point B. This intersecting point B is the pole of plane (h k l) in the pole figure.

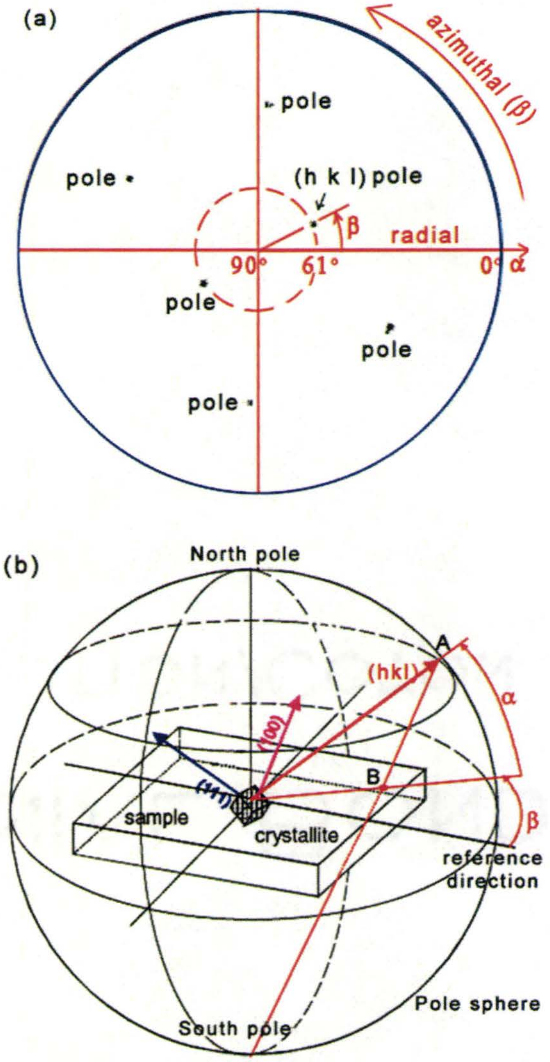

Figure 3.7: The definition of the radial angle, α, and the azimuthal angle, β, in a (a) pole figure and (b) stereographic projection (adapted from (Bruker-AXS, 1999)). Figure 3.7(b) also shows how an (h k l) plane in a crystallite is represented in the pole figure. The plane normal is projected onto the pole sphere around the crystallite and intersects the sphere at point A. The connection between the intersecting point A and the south pole will intersect the equatorial plane at point B. This intersecting point B is the pole of plane (h k l) in the pole figure.

3.2.2 Surface Morphology

The surface morphology of the thin films was observed using the atomic force microscopy (AFM) and the scanning electron microscopy (SEM) provided by Canadian Centre for Electron Microscopy (CCEM). The two techniques are based on different working principles. But both could reach nanometer resolution.

The imaging process within the SEM involves complex interactions of electrons with the atoms of the specimen. When a fine beam of high-energy electrons is scanned across the surface of the specimen, a large amount of backscattered electrons and secondary electrons are generated. These backscattered and secondary electrons are collected by a detector, amplified and displayed on a cathode ray tube or a computer monitor that scans in synchronism.

Topographic contrast arises because the number and trajectory of the backscattered electrons and the number of the secondary electrons depend on the incident angle of the electron beam with respect to the sample surface. Since the electron beam is effectively parallel, the incident angle is only affected by the local surface features of the specimen. Taking secondary electrons as an example, the contrast, C, in the SEM image could be estimated as (Goldstein *et al.*, 2003):

$$C \sim tan(\theta)d\theta \tag{3.2}$$

where θ is the tilt angle of the local specimen surface and $d\theta$ is the difference in the tilt angle, θ, between two local surface regions.

For AFM, the topographic information of the specimen is collected using a microscale cantilever with a sharp tip (Veeco-Instruments, 2003). When the tip is brought into proximity of the sample surface, the force between the tip and the sample causes the cantilever to bend. Since this locally varying deflection directly represents the corrugation of the specimen surface, the surface morphology of the specimen is probed. Such a working mode is referred to as *contact mode*. It has the advantage of high scan speeds and high resolution. However, a lateral shear force is generated when the tip scans across the sample surface, which could bring distortions to the features in the image and scrape the sample surface. To avoid the surface damage to the soft specimen, a non-contact mode can be applied. The tip does not touch the sample, but oscillates above it at a frequency which is slightly larger than the resonance frequency of the cantilever. The oscillation amplitude is modified by the interaction forces between the tip and the sample. However, a constant oscillation is maintained at each data point through a feedback loop when the sample is scanned. The feedback system leads the scanner to move vertically where the moving distance is used to form the topographic image of the sample surface. Drawbacks of the non-contact mode are low lateral resolution and scan speed. The tip could be trapped by a layer of absorbed fluid on top of the sample surface. Due to these disadvantages, applications for non-contact mode are limited while an intermittent mode, i.e. *tapping mode*, is applied instead. For tapping mode, the cantilever is oscillated at a frequency which is slightly below its resonance frequency and the tip gently “taps” the sample at the bottom of its swing.

The AFM and SEM facilities used in the current project are the *JEOL* JSM-7000F SEM and the *Digital Instrument* scanning probe microscope working at tapping mode with a NanoScope IIIa controller.

3.2.3 Microstructure and Composition

The microstructure of the films were characterized using a *Philips* CM12 transmission electron microscope (TEM) operating at 120 kV and a *JEOL* 2010 FEG TEM operating at 200 kV. The composition of the films was measured with X-ray energy dispersive spectroscopy (XEDS) associated with *JEOL* 2010 FEG STEM. The facilities were supplied by Canadian Centre for Electron Microscopy (CCEM).

The TEM can be compared with an optical microscope where the electron source replaces the light source and the magnetic lens replaces the optical lens. Figure 3.8 shows a typical TEM image system. The electron beam is made into parallel by a condenser lens. The parallel beam, after passsing through a thin specimen, is projected as an enlarged image onto a fluorescent screen by an objective lens.

When the electron beam is passing through a crystalline sample, it is diffracted by the crystal planes of the specimen to various well-defined directions. The scattered electron waves from successive parallel planes are subjected to constructive interference if the angle of incidence satisfies the *Bragg's law*, which produces a diffraction pattern (DP). The DP is brought to a focus at the back focal plane of the objective lens. Since the positions and intensities of the diffracted beam are strongly affected by the crystal structure of the specimen, the DP provides the crystallographic information of the specimen. The diffraction contrast is the major source of contrast in TEM images. A bright-field (BF) image is generated when the direct beam is selected to form the image while a dark-field (DF) image is produced when a diffracted beam is used. For the BF image, the area that appears bright in the image corresponds to the specimen region which scatters electrons slightly while the

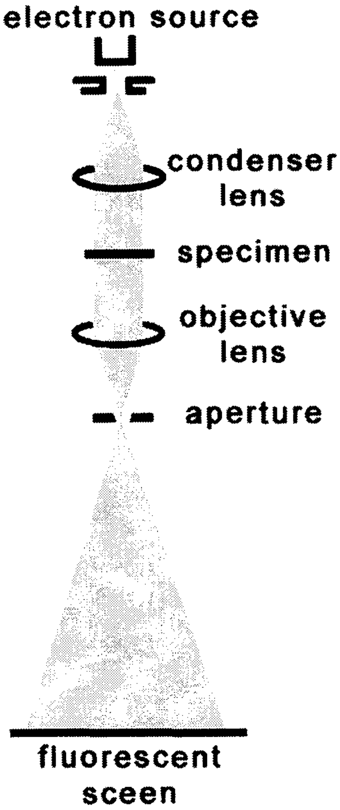

Figure 3.8: A typical TEM system which is made up of four parts: (i) electron source, (ii) magnetic lens, (iii) apertures, and (iv) fluorescent screen (Adapted from FEI, www.fei.com).

dark area corresponds to the region where the electrons are scattered to higher angles and blocked by an aperture. In contrast to the BF image, the bright area in a DF image is the area where the selected diffraction spot is at the *Bragg*' condition. Therefore, the DF image contains specific orientation information and typically shows a higher contrast than the BF image.

The above mentioned electron-specimen interaction describes the elastic scattering of the electron beam where the incident electron loses no energy in the scattering process.

However, there exists a considerable amount of inelastic scattering when the electron beam passes through the specimen. The inelastic scattering also provides important information. One of them is the characteristic X-ray. The generation of X-rays can be understood from the schematic drawing shown in figure 3.9. The high-energy electrons impinge the specimen atom and knock out a core electron from the inner-shell. The ejected electron escapes the attractive field of the nucleus and leaves a hole in the inner shell. The atom is now in a high energy state and will return to its stable stage by filling the missing electron with one from the outer-shells. This electron transfer process results in a release of surplus energy in the form of X-rays. Since the surplus energy is the difference in energy of the two electron shells involved and is unique to each element, the characteristic X-ray can be used for elemental identification. Attaching an X-ray detector and the associated processing electronics to the TEM equipment, the X-ray signals can be collected and processed for both qualitative and quantitative analyses.

The quantitative composition analyses using the X-ray signals are based on the Cliff-Lorimer equation (Williams & Carter, 1996):

$$\frac{C_A}{C_B} = k_{AB}\frac{I_A}{I_B} \tag{3.3}$$

where C_A, C_B, I_A, and I_B are the weight percentage and the X-ray intensities of the element A and B in a binary system AB. The term k_{AB} is a correction factor which is related to the atomic-number, absorption, and fluorescence effect. The k_{AB} factor can in general be determined with considerable accuracy by using standards or first-principle calculation (Williams & Carter, 1996). In the current work, the k-factor was determined with first-principle calculations (Cliff Lorimer thin ratio section) integrated in the *INCA* soft-

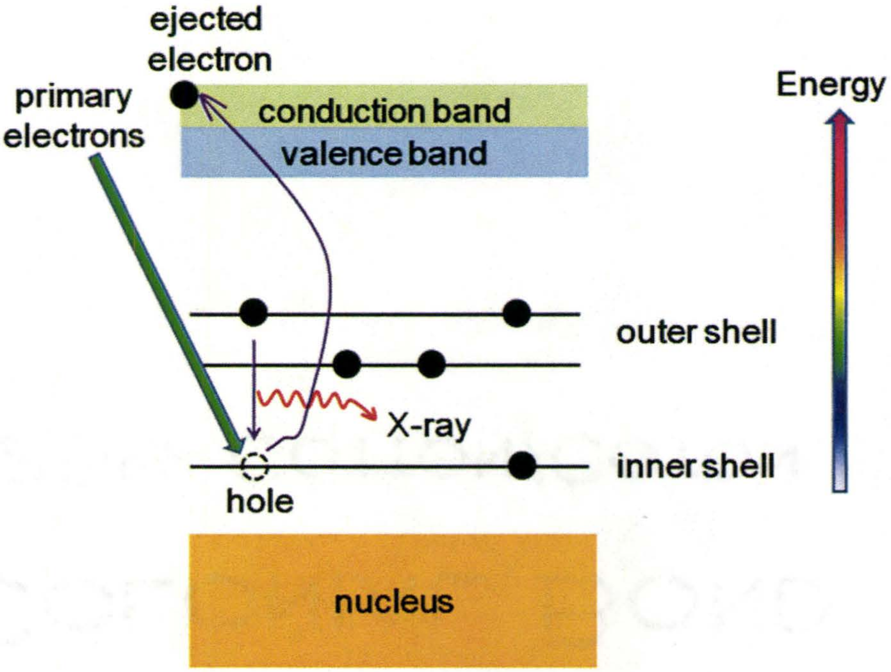

Figure 3.9: The generation of the characteristic X-ray.

ware (*Oxford Instruments*). The X-ray line used was Kα line. To improve the accuracy of absorption and fluorescence correction, the density of the films (ρ = 7.8 g/cm^3) and the thickness of the TEM specimen ($t \approx$ 50 nm) were input into the software. The film's composition listed in the remaining part of the thesis is an average composition of ten to fifteen measurements carried out at different regions. A maximum standard deviation of 0.4% (in atomic percentage) has been observed for each individual element (e.g. the concentration of Ni is within the range of 51% ± 0.4% for films deposited on YSZ substrate), which indicates that the compositional gradient in the films is not significant.

3.2.4 Phase Transformation

The martensitic and ferromagnetic phase transformations were characterized through temperature dependent DC electrical resistivity and magnetization measurements. The resistivity was measured with an in-house developed four-point van der Pauw resistivity apparatus capable of operating between 4 and 410 K. The magnetization measurements were carried out using a Quantum Design MPMS SQUID system (provided by Brockhouse Institute for Materials Research).

In typical resistivity measurements, four electrical leads are attached to a rectangular sample in a manner shown in figure 3.10a. The voltage between leads 1 and 2 is recorded when current is fed between leads 3 and 4. The resistance can be estimated as $R = \frac{V_{12}}{I_{34}}$. To get sufficient accuracy, the distance between Contact 1 and Contact 2 has to be large enough to guarantee that the lines of the current flow are parallel between 1 and 2. This condition, however, is not satisfied for the square shaped thin film samples where the current distribution is unknown. In such a case, van der Pauw method has to be applied. Theoretically, the van der Pauw technique is applicable to specimens in any shape as long as the sample's thickness is uniform and much less than the width and length of the sample.

Figure 3.10b shows the experimental geometry for the van der Pauw measurements. Four tiny gold contacts are attached to the four corners of the films. A current is fed along one edge of the film (e.g. I_{12}) and the voltage is measured across the opposite edge (e.g. V_{34}). A horizontal resistance (i.e. $R_{12,34}$) is then calculated as:

$$R_h = R_{12,34} = \frac{V_{34}}{I_{12}} \tag{3.4}$$

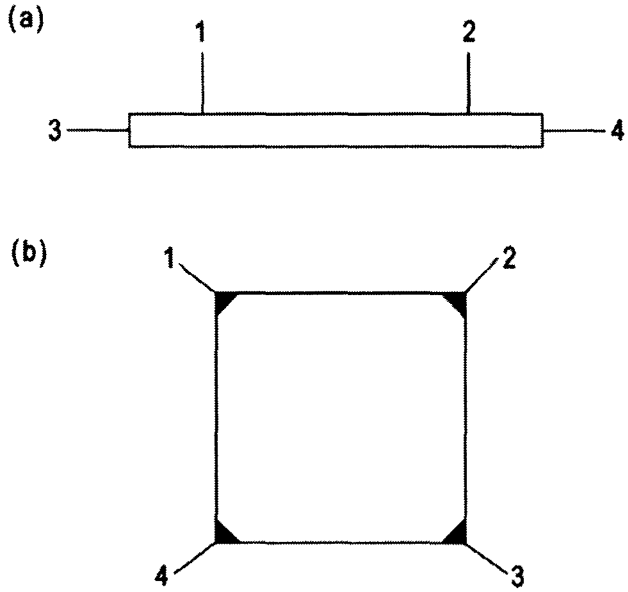

Figure 3.10: Four probe electrical resistance measurement for (a) long rectangular sample and (b) flat sheet sample with a square or rectangular shape. The experimental geometry shown in (b) is based on the van der Pauw method (Adapted from Van der PAUW (1958)).

Taking the same measurements on the other two edges will give a vertical resistance (i.e. $R_v = R_{14,23} = \frac{V_{14}}{I_{23}}$). The actual resistance of the film (R_f) can be derived using the van der Pauw equation (Van der PAUW, 1958):

$$exp(-\pi R_h/R_f) + exp(-\pi R_v/R_f) = 1 \tag{3.5}$$

To improve accuracy and cancel out the Seebeck effect, additional measurements can be made for R_h and R_v by using the reciprocity theorem (i.e. $R_{12,34} = R_{34,12}$) and switching the polarity of the current source and the voltage meter. The average horizontal and vertical resistance obtained in this manner is:

$$R_h = \frac{R_{34,12} + R_{12,34} + R_{43,21} + R_{21,43}}{4} \tag{3.6}$$

$$R_v = \frac{R_{14,23} + R_{23,14} + R_{41,32} + R_{32,41}}{4} \tag{3.7}$$

3.2.5 Magnetic Properties

A *Quantum Design* magnetic property measurement system (MPMS) associated with the superconducting quantum interference device (SQUID) was used to investigate the magnetic properties of the as-grown Ni-Mn-Ga films. The SQUID magnetometer is designed according to the Josephson effect where superconducting electrons are tunneling, across a very narrow insulating link (i.e. Josephson junction), between two superconductors (Cullity & Graham, 2009).

The form of the device is shown in figure 3.11. Two pieces of semi-circular shape superconductors are connected by two insulating links and form a superconducting ring. A measuring current flows through the ring from Point I to Point O where an equivalent amount of current passes through each of the two links. If the ring is subjected to a changing magnetic flux from the specimen, induction current is generated inside the ring. The induced current adds to the measuring current in one link but subtracts in the other. Due to the addition of the induction current, the current flowing through the link could exceed a critical value where tunneling of the electrons across the link becomes impossible. A voltage is then developed across the link. Since the flux enclosed by the superconducting loop must be an integral number of the flux quanta, $\Phi_0 (= 2.067 \times 10^{-15}$ Wb), the superconducting ring prefers to increase the enclosed flux to Φ_0 by switching the polarity of the induced current if the external flux, Φ, is less than Φ_0 but exceeds $\frac{\Phi_0}{2}$ (i.e. $\frac{\Phi_0}{2} < \Phi < \Phi_0$). Therefore, the induced current changes direction every time the flux increases by $\frac{\Phi_0}{2}$. If

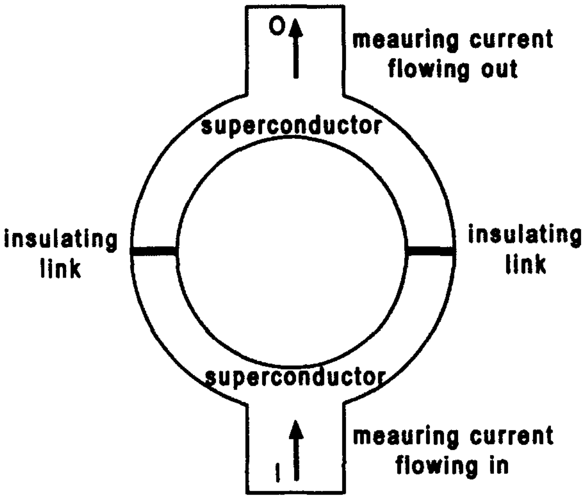

Figure 3.11: Flux sensor of a superconducting quantum interference device (SQUID) (Adapted from (Cullity & Graham, 2009)).

the current is more than the critical current of the superconducting ring, the ring operates in a resistive mode. The developed voltage is a function of the applied magnetic flux and oscillates in a period of Φ_0. Thus, no matter how large the external flux is, the result is a periodic appearance of a voltage between points I and O. Each voltage step is associated with the passage of a single flux quantum Φ_0 across the superconducting loop. The flux from the sample is then estimated from the pulse voltage.

3.2.6 Magnetic Domain Observation

A number of techniques, such as ferromagnetic colloidal solution (Williams *et al.*, 1949), Kerr optical method (Rave *et al.*, 1987), Lorentz microscopy (Lodder, 1983), neutron diffraction topography (Baruchel *et al.*, 1981), and atomic force method (Saenz & Garcia, 1987), can be used for magnetic domain observation. The method used in the current work is magnetic force microscopy (MFM). MFM is a non-destructive technique through which special sample preparation is not necessary. With MFM the magnetic and the topographical information can be collected simultaneously.

An MFM, just like an AFM, is a branch of scanning probe microscopy. The speciality rests with a magnetized tip which is coated with a thin film of a hard or soft magnetic material. The magnetic interaction between the tip and the stray field above the sample leads to a change in the cantilever's resonant frequency and phase. Measurements are taken in two passes across each scanline (Digital-Instruments, 1996). The cantilever is first scanned over the specimen surface in a tapping mode to record the topographical data. It is then raised above the sample surface to perform the second scan. During the second scan, a constant separation between the tip and local surface topography is maintained while the influence of sample's magnetic forces is monitored. Since the amount of shift in the cantilever's resonant frequency is proportional to the vertical gradients in the magnetic forces on the tip, a magnetic microstructure of the sample is thus imaged.

The MFM apparatus used here (provided by Canadian Centre for Electron Microscopy (CCEM)) is a *Digital Instrument* (Digital-Instruments, 2008) scanning probe microscope (SPM) and a NanoScope IIIa controller. A *Veeco Instruments* (Veeco-Instruments, 2009) produced metal coated etched silicon probe (MESP) is utilized as the cantilever tip. The lift scan height for the measurements of the magnetic force gradient is 50 nm.

3.3 Fabrication of Free-Standing Ni-Mn-Ga Films

It has been reported in the literature that the Ni-Mn-Ga films deposited on MgO substrates showed large in-plane strains due to the substrates' constraint (Thomas *et al.*, 2008b). Such observation inspired our idea of using the substrate-imposed stresses to study the effect of the mechanically induced martensitic variants reorganization. The plan was to compare the microstructure of a released film with the one that is affixed to the substrate. A key issue of this study was to design a processing method through which the Ni-Mn-Ga film could be effectively released from the MgO substrate. A common way to do so is to mechanically peel the film off the substrate (Rumpf *et al.*, 2006). This simple method, however, is not applicable to our films since the film clamp the substrate very tightly. Mechanically peeling is thus very likely to destroy the film. Another generally used scheme is to etch off the substrate with a chemical solution, which involves the photolithography technique and the wet chemical etching (Dong *et al.*, 2004; Khelfaoui *et al.*, 2008). A sacrificial-buffer layer at the film-substrate interface is usually required (Dong *et al.*, 2004; Khelfaoui *et al.*, 2008). When this sacrificial layer is etched off the film is freed from the substrate. Difficulties involved in this technique are finding: (i) an appropriate buffer-layer material whose lattice matches the lattices of both Ni-Mn-Ga film and MgO substrate; (ii) a proper solution which can effectively attack the buffer layer. To circumvent these problems, we designed an alternative approach where the sacrificial layer was avoided. The etching solution we employed preferentially attacks the MgO substrate rather than the Ni-Mn-Ga film. Thus the film is undercut without being chemically damaged.

The entire micromachining process employed in the current project is illustrated in figure 3.12. The surface of the Ni-Mn-Ga / (100) MgO composite is first covered with a layer of photoresist. A photolithographic shadow mask, with a bridge pattern, is placed over the sample and exposed to ultraviolet light. The sample is then placed in a developer (sodium hydroxide water solution) where the photoresist is removed only from the areas exposed to the ultraviolet light. This leaves behind a microbridge pattern. The sample is placed in dilute nitric acid where the photoresist protects the patterned area while the exposed Ni-Mn-Ga film is etched away. The net result is that the bridge pattern becomes imprinted into the film. Following this step, the sample is placed in dilute hydrochloric acid. Because this acid preferentially attacks the MgO, the Ni-Mn-Ga bridge will be undercut. Over time, such a process will result in the bridge arm being detached from the substrate while the abutment is still attached and supported by the substrate. Finally, the photoresist is removed with acetone and methanol. The photolithographic processing and associated wet-chemistry was equipped in the Centre for Emerging Device Technologies (CEDT) at McMaster University.

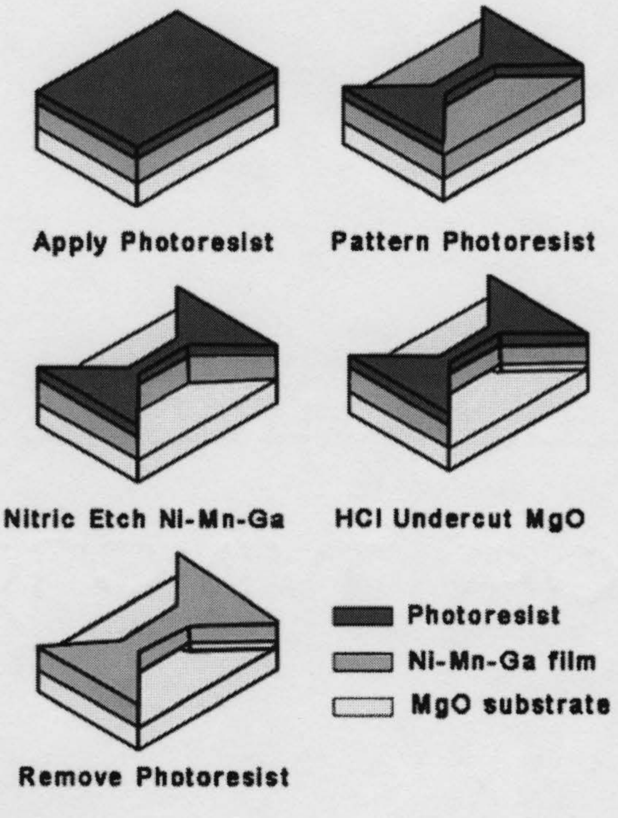

Figure 3.12: Fabrication process for a Ni-Mn-Ga free-standing bridge patterning.

Chapter 4

Synthesis of the Ni-Mn-Ga Films

4.1 Substrate Selection

It has been mentioned in the first chapter that the fabrication of uniform, defect-free, and highly textured films with a grain size large enough to accommodate internal twinning is the prerequisite for achieving magnetic field induced strain and shape memory functionalities in the films. The first consideration for significant improvement in film's microstructure is focused on highly textured epitaxial films deposited on lattice matched substrates. A number of substrates whose lattice parameters are close to that of the Ni-Mn-Ga films were tested. These substrates include (100) NaCl, (100) InP, (100) GaAs, (100) YSZ ($(Zr,Y)O_2$ with ZrO_2:Y_2O_2=92:8), (100) MgO, (110) MgO, (100) $MgAl_2O_4$, and $(11\bar{2}0)$ Al_2O_3. The as-grown films were measured with $\theta - 2\theta$ powder XRD. The XRD results indicate that only those films deposited on (100) MgO and (100) YSZ show good epitaxial relationship with the underlying substrate, exhibiting single growth orientation and high-intensity Bragg reflections in the XRD spectra. Therefore, (100) MgO and (100) YSZ were selected in the current project as the epitaxial templates for film growth. Films grown on those unselected substrates either have undesired crystallographic structures indicated by the XRD measurements or random grain orientations shown as multiple peaks in the powder X-ray profiles.

4.2 Optimization of the Deposition Parameters

The next step toward the fabrication of a high quality film is to optimize the deposition parameters. A wide range of laser repetition rates (i.e. from 10 to 40 Hz) and growth temperatures (i.e. 400$\sim$650°C) were tried out. Our results indicate that a low repetition rate (i.e. $\sim$10 Hz) and a high growth temperature (i.e. $\geq$500°C) are favourable for Ni-Mn-Ga system. At high repetition rate, the incoming adatoms do not have enough time to migrate on the substrate surface and thus attach to the larger atomic clusters, which gives rise to small islands at the initial film growth and polycrystalline films at the end. Furthermore, porosities usually form in the films deposited at relatively high repetition rates since the atomic clusters are not able to fully coalesce between two laser pulses. Figure 4.1 shows an SEM image of a Ni-Mn-Ga film deposited on (100) YSZ at a repetition rate of 30 Hz. A puzzle like surface morphology with a high degree of porosity has been observed due to a high laser repitition rate. Similarly, a low substrate temperature can also lead to poor crystallinity since the mobility of the adatoms and atomic clusters is low. The SEM image in Figure 4.2 was taken from a Ni-Mn-Ga film deposited at 400°C . As shown in the imaging, the grain size of the films is extremely small, which is within the

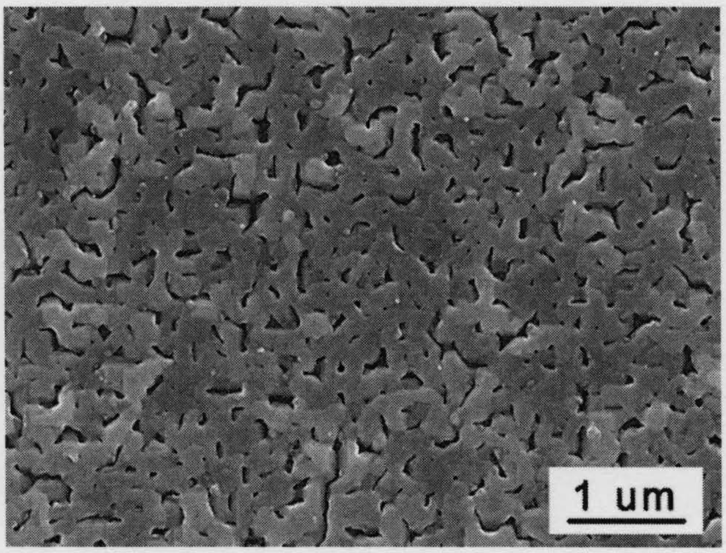

Figure 4.1: SEM image for a Ni-Mn-Ga film deposited on (100) YSZ at 550°C using 30 Hz repetition rate. The film shows a puzzle like surface morphology with a high degree of porosity.

nanometer length scale. These SEM observation reveals that the laser repetition rate and the substrate temperature are two crucial factors for the film growth. A low repetition rate and a high substrate temperature favor both crystallinity and surface morphology of the deposited films. It should be noted that high growth temperatures have also been proved necessary in order for the films to exhibit ferromagnetism (Rumpf *et al.*, 2006; Hakola *et al.*, 2004b).

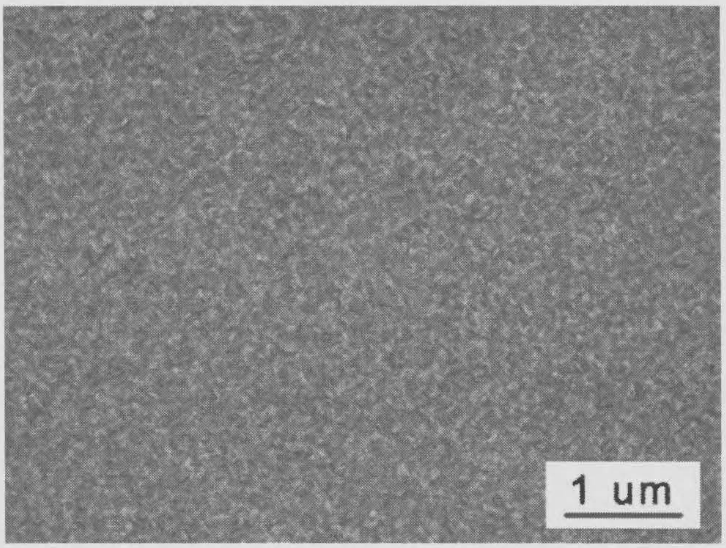

Figure 4.2: SEM image for a Ni-Mn-Ga film deposited on (100) YSZ at 400°C using 10 Hz repetition rate. The grain size of the film is much less than one micrometer.

4.3 Solution to the Loss of Volatile Elements at Elevated Temperatures

By recognizing the effect of the high growth temperature on the quality of the as-grown films, we deposited our Ni-Mn-Ga films in a previously unexplored high temperature regime ($557°C \leq T \leq 650°C$). The SEM observation indicates that the films' grain structure has been significantly improved (figure 4.3).

Unfortunately, the XEDS measurements on these films reveal a significant loss of the volatile elements, such as manganese and gallium. The film composition of $Ni_{68}Mn_{20}Ga_{12}$ (at.%) deviates significantly from the target composition (i.e. $Ni_{49}Mn_{28}Ga_{23}$ (at.%)). Such a Ni-rich phase is, in fact, associated with the cubic $L1_2$ phase (Tello *et al.*, 2002; Colinet & Pasturel, 2002) instead of the desirable $L2_1$ phase (Webster *et al.*, 1984). The powder

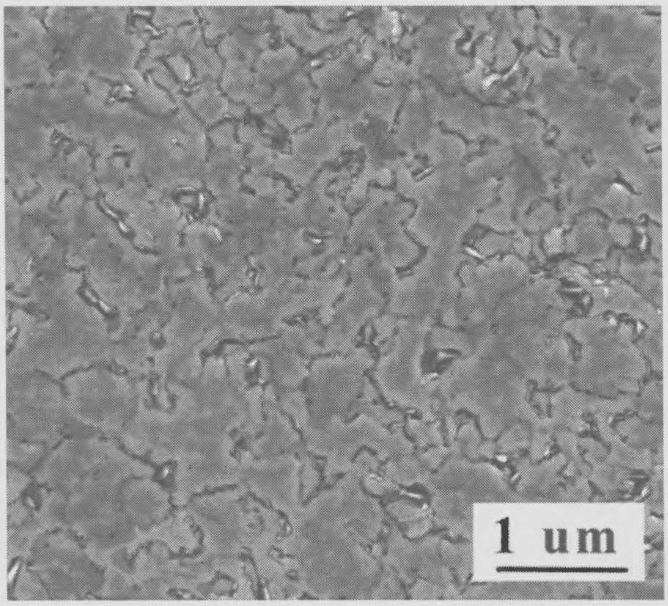

Figure 4.3: SEM image for a Ni-Mn-Ga film deposited at 650°C on (100) YSZ using 10 Hz repetition rate. The film shows a considerable improvement to the grain structure due to the elevated growth temperature.

XRD and XRD^3 measurements indicate that the obtained $L1_2$ phase is highly textured and grows along the [111] direction. Figure 4.4 shows the powder X-ray spectrum of the film. In addition to the X-ray peaks associated with the substrate, the spectrum exhibits a single sharp film peak at $2\theta = 43.5°$ which corresponds to the (111) reflection of the cubic $L1_2$ phase. The XRD^3 dataset is consistent with the powder XRD result. It shows a [111] oriented Ni-Mn-Ga film comprised of four in-plane grain orientations, each separated for 90° in the film plane. The lattice parameter derived from the XRD^3 dataset is a=3.6 Å. Figure 4.5 presents the $\{111\}$ pole figure of the generated $L1_2$ film. To understand this pole pattern, a $\{111\}$ pole figure of a single crystal is first considered. Simply stated, a single crystal $\{111\}$ pole figure should consist of four poles: a pole in the center of the figure, corresponding to the (111) planes, and three poles at a 71° radial angle separated by an azimuthal angle of 120° which correspond to the $(11\bar{1})$, $(1\bar{1}1)$ and $(\bar{1}11)$ planes. The

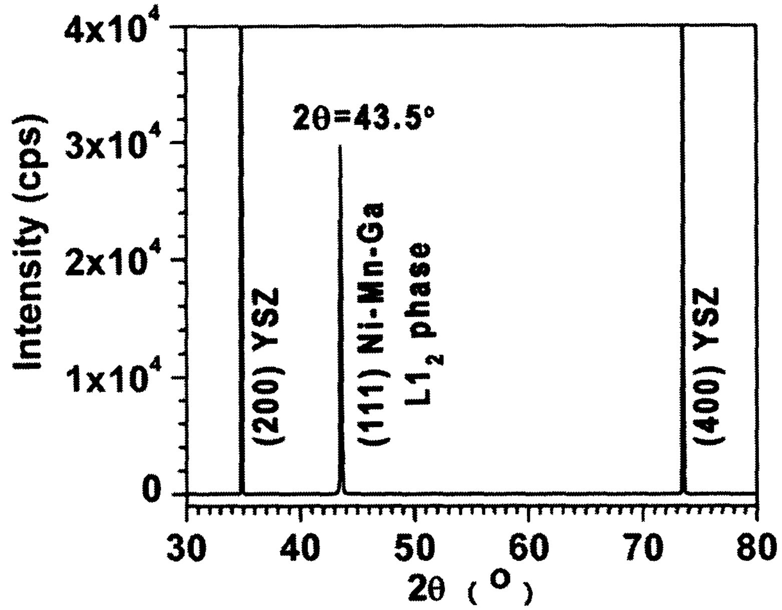

Figure 4.4: $\theta - 2\theta$ X-ray spectrum for a $Ni_{68}Mn_{20}Ga_{12}$ (at.%) film deposited at 650°C on (100) YSZ. The single sharp peak at $2\theta = 43.5°$ corresponds to the (111) reflection of the Ni-Mn-Ga film. The absence of the other film peaks indicates that the film is highly textured and grows along [111] direction.

fact that the $\{111\}$ pole figure shown in figure 4.5 consists of twelve equally spaced poles in the 71° outer ring instead of three, as is the case for a single crystal, indicates that the film is comprised of four identical orientation domains ($12 \div 3 = 4$) with in-plane rotations of 0°, 90°, 180°, and 270°.

The $L1_2$ phase does not have the Heusler type structure and is not known to exhibit a shape memory effect. This phase is originated from the Mn and Ga deficiency at elevated growth temperatures and thus has to be circumvented. The method used in the literature is to produce Ni-Mn-Ga films by a low temperature deposition followed by a high temperature anneal (Chernenko *et al.*, 2005b; Liu *et al.*, 2008; Ohtsuka *et al.*, 2006). This

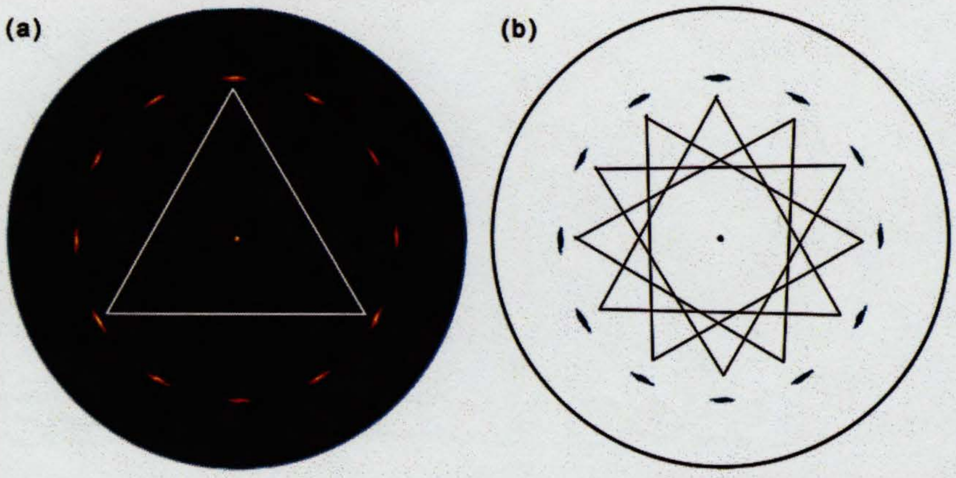

Figure 4.5: (a) {111} pole figure for a $Ni_{68}Mn_{20}Ga_{12}$ (at.%) film deposited at 650°C on (100) YSZ, and (b) the schematic depiction of the {111} pole figure shown in (a). The observed pole pattern is characteristic of a [111] oriented film with four in-plane domain orientations, where a single domain is characterized by the central pole and three poles from the outer ring separated by 120° (denoted by the white triangle in (a)). Note the entire pole figure can be reproduced from four 90° rotations of the single domain pole pattern, as shown in (b).

procedure allows the encapsulation of volatile components at low temperatures while the elevated anneal temperatures promote grain growth. Although the post-deposition annealing yielded Ni-Mn-Ga films with acceptable quality, it is less superior to the method of high temperature *in situ* deposition. A number of factors favor *in situ* processes for cases where a high degree of crystallinity is desired. In this case, the substrate can be a much more effective template, as it allows increased mobility of surface adatoms, compared to bulk diffusion processes. This results in enhanced crystallization at reduced temperatures.

In situ film depositions at temperatures where elemental volatility is high have often relied on the arrival of adatoms in non-stoichiometric proportions at the substrate's surface (Panish & Temkin, 1993). With the proportions chosen to compensate for the loss of volatiles, the correct stoichiometry is preserved. Moreover, in a properly designed process,

Table 4.1: Listing of the target and resulting film compositions as obtained from XEDS measurements. Note that the composition of Target 1 is near that of the film derived from Target 2.

	Target composition (at. %)	Film composition obtained (at. %)
Target 1	$Ni_{49}Mn_{28}Ga_{23}$	$Ni_{68}Mn_{20}Ga_{12}$
Target 2	$Ni_{32}Mn_{44}Ga_{24}$	$Ni_{51}Mn_{29}Ga_{20}$

this stoichiometry is uniform throughout the film, a result that is difficult to achieve with post-growth processing.

To take the advantage of the *in situ* depositions but overcome the problem of the Mn and Ga deficiency at elevated temperatures, we prepared a Ni- and Ga- enriched target. By using such an enriched target, the loss of the volatile elements can be effectively compensated for through excess addition of these elements to the target material. The composition of the enriched target was determined through a fine tuning process where additional Mn and Ga were added to the target until the composition of the resulting films was in the range of the desired composition. Through this process, the composition of $Ni_{32}Mn_{44}Ga_{24}$ (at.%) was finally employed in the enriched target.

Films deposited using the enriched $Ni_{32}Mn_{44}Ga_{24}$ target also show a significant Mn and Ga loss, but due to the initial enrichment of these volatile elements, the resulting film composition ($Ni_{51}Mn_{29}Ga_{20}$ (at.%)) lies in the region corresponding to the Heusler $L2_1$ structure in the ternary Ni-Mn-Ga phase diagram (Tello *et al.*, 2002). In order to better appreciate the impact of the enrichments one should examine table 4.1, which lists the compositions of the original and the enriched targets and the films obtained from them. It should be noted that even though Target 1 has the desired composition for shape memory effects, a film near this composition is only obtained through the use of Target 2.

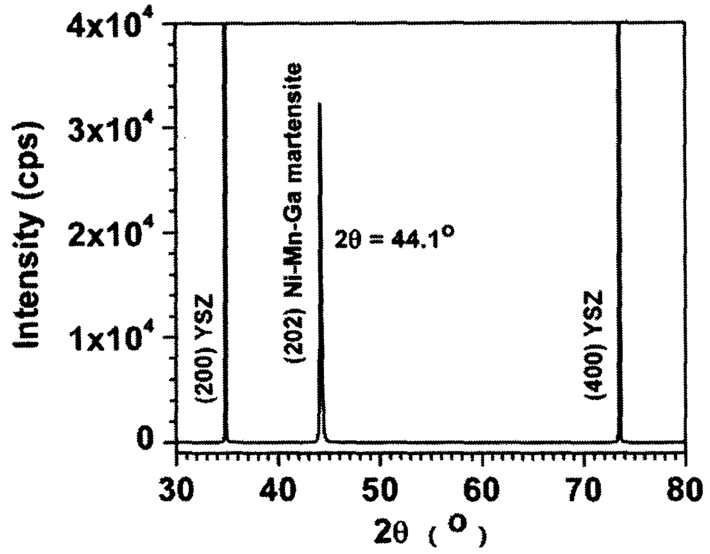

Figure 4.6: $\theta - 2\theta$ X-ray spectrum for a $Ni_{51}Mn_{29}Ga_{20}$ (at.%) film deposited on (100) YSZ using a enriched $Ni_{32}Mn_{44}Ga_{24}$ (at.%) target. The single prominent (202) peak at $2\theta = 44.1°$ indicates a [101] oriented film.

$\theta - 2\theta$ X-ray spectra for those films derived from the enriched $Ni_{32}Mn_{44}Ga_{24}$ (at.%) target show a single prominent film peak at $2\theta = 44.1°$ (figure 4.6), consistent with a [101] oriented martensitic phase. Evident from the SEM imaging (figure 4.7) are the well-connected micrometer-size grains made possible by the elevated deposition temperatures. Atomic force microscopy (AFM) yielded a root mean square (RMS) surface roughness of 5 nm.

The crystallographic information for a $Ni_{51}Mn_{29}Ga_{20}$ (at.%) film was also investigated using XRD^3 measurements. The measurements were taken at a series of temperature from 293 K to 380 K so that the information for both martensitic and austenitic phase could

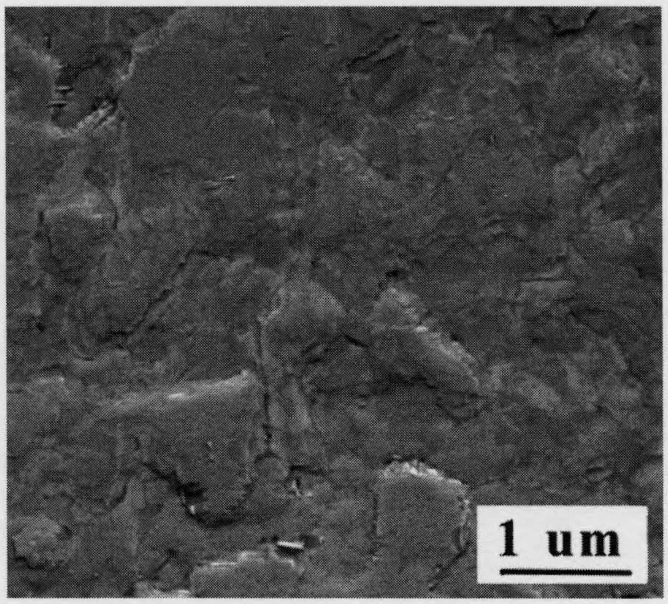

Figure 4.7: SEM image for a $Ni_{51}Mn_{29}Ga_{20}$ (at.%) film deposited on (100) YSZ using an enriched $Ni_{32}Mn_{44}Ga_{24}$ (at.%) target. The film shows well-connected micrometer-size grains made possible by the elevated deposition temperatures

be recorded. The film was first heated above the austenitic transition temperature and then cooled back to room temperature. The room temperature lattice parameters indicate an orthorhombic martensitic phase with a=6.112(4) Å, b=5.885(3) Å, and c=5.527(2) Å, while those obtained at 380 K indicate a cubic austenite phase with a=b=c=5.846(3) Å.

To extract the texture information from the XRD^3 dataset, the $\{400\}$ pole figure was generated for both phases. The $\{400\}$ pole figure for the austenitic phase is illustrated in figure 4.8 and the (400) and (004) pole figures for the martensitic phase is given in figure 4.9. It should be understood that a [101] oriented single crystal cubic material will give rise to a $\{400\}$ pole figure with two peaks at a 45° radial angle separated by an azimuthal angle of 180°. A [101] oriented single crystal orthorhombic material with lattice parameters $a \neq b \neq c$, on the other hand, exhibits (400) and (004) peaks slightly deviated from the 45° radial angle due to the nonequivalent lattice constants. The fact that the high temperature austenitic phase shows four peaks at 45° instead of the two expected for a single crystal is a clear indication that the film is comprised of two in-plane orientation domains offset by 90°. The multiple in-plane orientations are also observed in the martensitic phase. As shown in figure 4.9, the (400) and (004) pole figures for martensitic phase also comprise four reflections for each pole figure. In the (400) pole figure (figure 4.9a), the four poles at 42.2° radial angle (i.e. four poles connected with dashed lines) are associated with the film, while remaining poles originate from the YSZ substrate. The pole configuration indicates that the film is composed of four crystallographic orientations, where each orientation gives rise to a single pole near 42°. The (004) pole figure (figure 4.9b) shows four poles corresponding to these same orientations, except in this case the poles are at a radial angle of approximately 48°. The reason why the martensitic phase consists of four in-plane orientations instead of the two as stated for the austenitic phase will be discussed in chapter 5. The experimental (040) pole figure (not shown here) exhibits no poles because the (040) plane of the film is perpendicular to the surface plane of the substrate. Thus, the poles that do exist lie at the experimentally inaccessible edge of the pole figure (i.e. a radial angle of 0°). It should be noted that the two room temperature results measured before and after heating the sample above 380 K are identical, indicative of a completely reversible martensitic phase transformation.

The microstructure of the $Ni_{51}Mn_{29}Ga_{20}$ (at.%) film was examined with cross-sectional TEM. The bright field image in figure 4.10 shows a highly twinned microstructure. The plate-shaped variants, with widths of 25-100 nm, are distributed throughout the film. Evident from the expanded view (figure 4.10b), showing the straight interface between adjacent variant plates, is the striation contrast from the slip-steps inside each plate. These

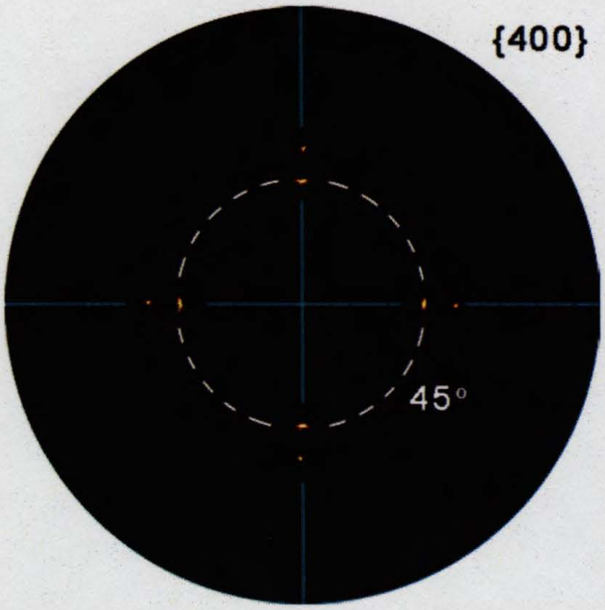

Figure 4.8: {400} pole figure for the austenitic phase of a $Ni_{51}Mn_{29}Ga_{20}$ (at.%) film measured at 380 K. The four poles connected with dashed lines are associated with the {400} reflections from the Ni-Mn-Ga film while the rest are associated with the {222} reflections from the YSZ substrate. The fact that there exist four film peaks at 45° instead of the two expected for a single crystal is a clear indication that the film contains two in-plane orientations offset by 90°.

subfeatures form in the course of the martensitic phase transformation to further relieve the transformation strains generated within the martensitic grains (Bhadeshia & Honeycombe, 2006).

Figure 4.11 shows the room temperature in-plane magnetization loop of the films. As it can be seen from 4.11, the films exhibit a saturation magnetization of 4.2×10^5 A/m, which is comparable to that of a bulk martensitic Ni-Mn-Ga crystal (Sozinov *et al.*, 2002a). Also observed in the loop is a low coercive field of $\mu_0H=0.005$ T, indicating the high film quality.

In summary, the $Ni_{51}Mn_{29}Ga_{20}$ (at.%) films deposited using the Mn and Ga enriched target demonstrate good structural and magnetic properties. The films show the desired

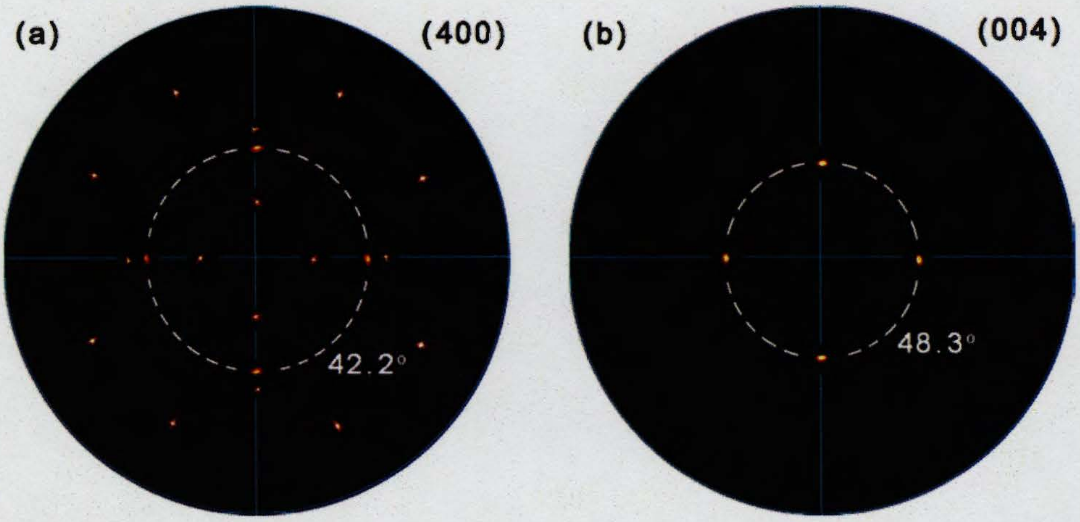

Figure 4.9: Room temperature (a) (400) and (b) (004) pole figures for the martensitic phase of a $Ni_{51}Mn_{29}Ga_{20}$ (at.%) film. In (400) pole figure, the four poles connected with dashed lines are associated with film while the rest are associated with the YSZ substrate. The (400) and (004) poles are slightly deviated from the 45° radial angle, consistent with the orthorhombic crystal structure of the martensitic phase.

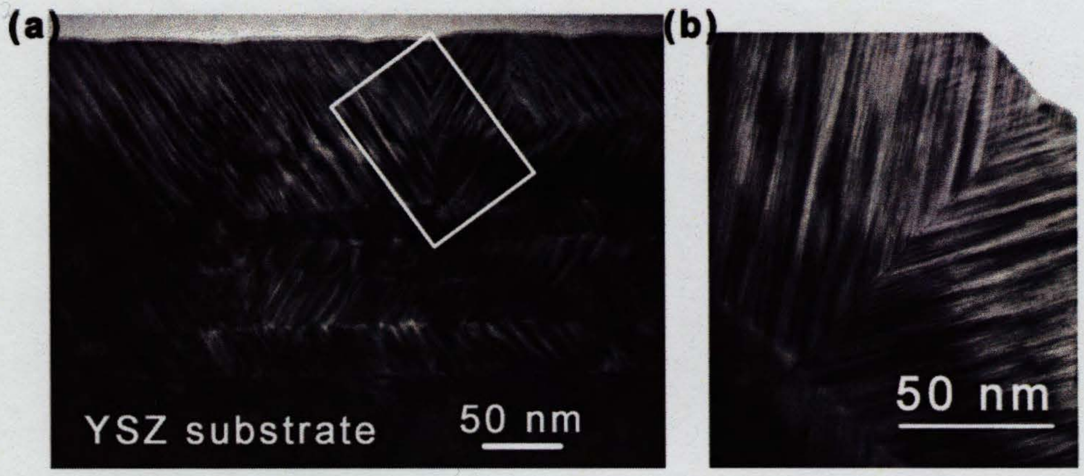

Figure 4.10: TEM bright field images of a $Ni_{51}Mn_{29}Ga_{20}$ (at.%) film showing (a) plate-shaped martensite variants containing, (b) micro-twinned slices. The image in (b) was taken at high magnification from the region in (a) denoted by the rectangle.

shape memory alloy properties of having a well-defined reversible martensitic transformation, a room temperature martensitic phase, and a micrometer-size grain structure. This

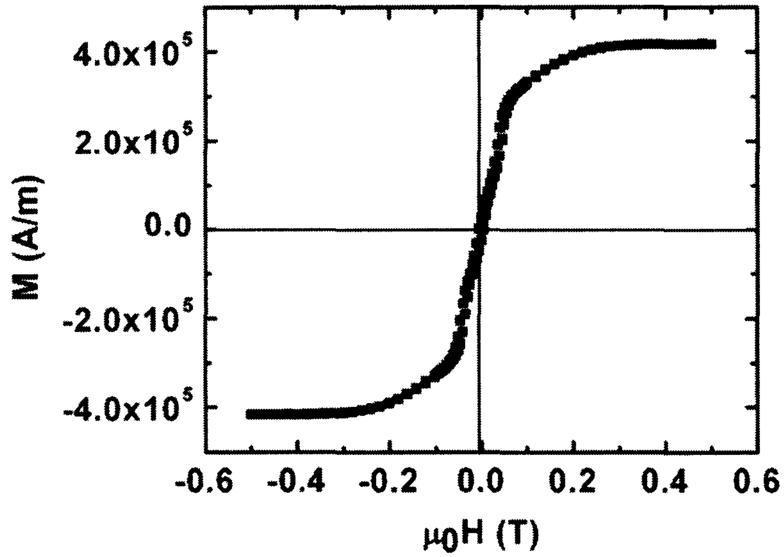

Figure 4.11: The in-plane magnetization of a $Ni_{51}Mn_{29}Ga_{20}$ (at.%) film measured at room temperature showing a saturation magnetization of 4.2×10^5 A/m.

significant improvement in film quality is attributed to the previously unexplored high temperature *in situ* growth regime and the enriched target.

Chapter 5

Magnetically Induced Martensitic Variant Reorientation (MIR) in Ni-Mn-Ga Thin Films

The magnetic shape memory effect relies upon twin boundary motion within a martensitic structure. The motion occurs when the difference in the magnetic energy, due to the various orientations of the magnetic moments in twin related variants, exceeds the mechanical energy needed for the displacements of the atoms in the vicinity of the twin boundary. The optimization of MIR effect has yielded bulk materials exhibiting magnetic field induced strains of $\sim 9.5\%$ (Sozinov *et al.*, 2002b), a value significantly larger than the strains observed in fast-response piezoelectric (Park & Shrout, 1997; Li *et al.*, 2008) and magnetostrictive materials (Pasquale, 2003).

While considerable progress has been made in understanding the MIR effect in bulk Ni-Mn-Ga materials, advances in thin film properties have been slow. A vast majority of the results available in the literature reveal that films affixed to a rigid substrate show no discernable MIR effect, even though they exhibit a well-defined martensitic transformation. Recent advances, however, have resulted in the deposition of films exhibiting a partial MIR effect (Thomas *et al.*, 2008a; Heczko *et al.*, 2008; Jenkins *et al.*, 2008; Zhang *et al.*, 2009; Buschbeck *et al.*, 2009). In contrast to single crystals, the MIR effect in these films showed reversibility even in the absence of external stresses (Thomas *et al.*, 2008a; Heczko *et al.*, 2008; Zhang *et al.*, 2009; Buschbeck *et al.*, 2009). Such observations provide possibilities for broad-based thin film applications. However, the physical origin of the self-activated reversibility is still not well understood.

The only explanation available in the literature is presented by Thomas *et al.* (Thomas *et al.*, 2008a), where the unique nature of the response was attributed to the fact that films are clamped to the substrate. Because of this, a film, unlike its single crystal counterpart, must reorient in a manner which preserves its overall in-plane dimensions. Based on this consideration, Thomas *et al.* described a mode by which the observed reorientation could take place for orthorhombic films with a grain structure containing $\{100\}$ oriented grains. In their mode the variant reorientation was facilitated by having the fraction of unit cells with the b-axis parallel to the field increased at the expense of the unit cells with the a-axis and c-axis in the field direction. In this manner, the overall size would be conserved since two b-axis lattice parameters are approximately equal to the sum of the a- and c-axis lattice parameters. The reorientation was attributed to an overall energy reduction in the applied field due to the fact that the measured anisotropy energy along the a-axis is more than four times as high as that along the b-axis. The self-reversibility was facilitated by substrate-imposed stresses which resisted the reorientation process (Thomas *et al.*, 2008b).

In the course of this thesis work, we have observed a partial self-reversible MIR effect similar to that observed by Thomas *et al.* (Thomas *et al.*, 2008a). The effect was detected in the $Ni_{51}Mn_{29}Ga_{20}$ (at.%) films grown on the (100) YSZ substrate, which show a [101] texture. Through a detailed analysis of the MIR response, combined with a thorough characterization of the film's crystallographic texture, microstructure, and magnetic domain structure, it is concluded that the aforementioned mechanism presented by Thomas *et al.* (Thomas *et al.*, 2008a) for their {100} oriented Ni-Mn-Ga films cannot be applied to the present situation. An alternative mechanism has to be considered for our [101] oriented films. The rest of the chapter will dedicate to this topic.

5.1 Magnetic Field Induced Martensitic Variant Reorientation

The crystallography of the $Ni_{51}Mn_{29}Ga_{20}$ (at.%) films grown on (100) YSZ has been described in Chapter 4. The three-dimensional x-ray (XRD^3) diffraction carried out at room temperature reveals the presence of four orientations of the orthorhombic martensitic phase in the films with lattice parameters a = 6.112(4) Å, b = 5.885(3) Å, and c = 5.527(2) Å. The diffraction dataset obtained at 380 K (figure 4.8) indicates a cubic austenitic phase with a = b = c = 5.846(3) Å. The as-grown films show a strong [101] texture. The temperature dependent x-ray measurements also reveal that films undergo reversible martensitic transformation between 300 K and 370 K. The phase transition temperatures M_s, M_f, A_s, and

A_f, determined by the temperature dependent DC resistivitiy measurement, are M_s = 361 K, M_f = 307 K, A_s = 312 K, and A_f = 370 K (Section 6.1). Coinciding with the structural phase transition was ferromagnetic ordering occurring over a temperature interval ranging from 359 K to 352 K upon cooling (Section 6.2). The room temperature magnetization curve shows a saturation magnetization of 4.2×10^5 A/m (figure 4.11), a value comparable to the bulk Ni-Mn-Ga sample. Also noticed in the magnetization loop but not shown in chapter 4 is an abrupt change in slope near 0.04 T. This phenomenon is a strong indication of the magnetically induced structural reorientation (MIR) of the martensitic variants (Heczko *et al.*, 2008) and will be discussed in detail in this subsection.

5.1.1 MIR Phenomenon

The in-plane magnetization hysteresis loops, i.e. M(H) curves, were measured at a series of temperatures when the films are cooled from the paramagnetic austenitic to the ferromagnetic martensitic phase. Figure 5.1 shows the M(H) curves corresponding to temperatures where there exists (a) pure austenite (372 K), (b) a mixture of austenite and martensite but where the austenite phase dominates (358 K), (c) a mixture of austenite and martensite but where the martensite phase dominates (340 K), and (d) pure martensite (300 K). At 372 K the magnetization curve exhibits the linear response associated with paramagnetic behavior. As the temperature is lowered to 358 K the film undergoes a ferromagnetic transition (T_C = 359 K), which is accompanied by a significantly broader austenite-to-martensite structural phase transition (figure 6.3). Although the ferromagnetic transition leads to a marked increase in magnetization at 358 K compared to the 372 K data, an even greater increase would have been observed if not for the fact that the observed increase is associated with only a partial ferromagnetic ordering. Complete ordering occurs once the sample is cooled to 352 K (figure 6.4). In the presence of a weak martensitic component the resulting magnetization at 358 K is thus dominated by the austenitic phase. The film shows the typical ferromagnetic loop with the small coercive field expected for a magnetically soft austenitic phase that exhibits low magnetic anisotropy (Tickle & James, 1999). At 340 K the ferromagnetic ordering is complete and the martensite phase has become dominant. At this point, the magnetization loop shows a wider hysteresis and a larger coercive field, a response consistent with the high anisotropy of the martensitic phase (Tickle & James, 1999; Jiang *et al.*, 2004). Also observed from the 340 K magnetization curve are abrupt changes in slope for magnetic fields near 0.025 T, which are apparent in both the magnetizing and demagnetizing processes. Such slope changes are easily recognized since the data points are evenly spaced in the magnetic field (μ_0H). The changes in slope, which are even more pronounced for the 300 K magnetization data (i.e., for pure martensite), have previously been attributed to the MIR effect (Thomas *et al.*, 2008a; Heczko *et al.*, 2008; Zhang *et al.*, 2009). Of note is that 340 K is the highest temperature where he MIR effect is observed in the films.

During the magnetization process, the 300 K magnetization curve (figure 5.1(b)) shows a steeper slope in a field range of 0.04 to 0.05 T. These magnetic field values, denoted as H_s and H_f, span a range of fields, H, where twin boundary motion occurs. Such a rise in magnetization slope is analogous to the far more abrupt rise observed for single crystals (Straka *et al.*, 2006; Heczko & Straka, 2003). The difference is likely attributed to the crystallographic texture associated with the film, which adds a polycrystalline character to the response (Gutierrez *et al.*, 2006). In order to quantize the critical field (H_{MIR}) needed to activate the MIR process, while avoiding the ambiguity associated with the range of magnetic fields over which the effect occurs, we define HMIR as the average of the fields corresponding to the onset and endpoint of the transition:

$$H_{MIR} = \frac{H_s + H_f}{2} \tag{5.1}$$

The magnetization increment, Δ M, induced in the entire MIR process is about 17% of the saturation magnetization of 4.2×10^5 A/m. Also evident from the figure is a rapid drop in the magnetization during the demagnetization process. This drop, which corresponds to the restoration of the initial twinning state, also spans a range of magnetic fields, but with an onset that is somewhat lower than H_f. The same phenomenon is also apparent in the third quadrant of the magnetization loop where the magnetic field is applied in the reverse direction. The symmetry in the MIR process implies high twin mobility and a lack of defect pinning sites. Important is the fact that the observed recovery is not reliant on external stimuli as is the case for single crystals, where an external compressive stress applied perpendicular to the magnetic field direction is required to induce reorientation of the twin variants (Murray *et al.*, 2000; Straka & Heczko, 2005; Straka *et al.*, 2006).

5.1.2 Temperature Dependence of the MIR Effect

The temperature dependence of HMIR for the $Ni_{51}Mn_{29}Ga_{20}$ (at.%) films is presented in figure 5.2. The MIR effect is first observed in the magnetization data at 340 K, where the film contains a significant amount of the martensitic phase. As the temperature is lowered further, the activation field HMIR steadily increases, suggesting that it becomes progressively more difficult to activate the MIR process. Such behavior is consistent with that observed

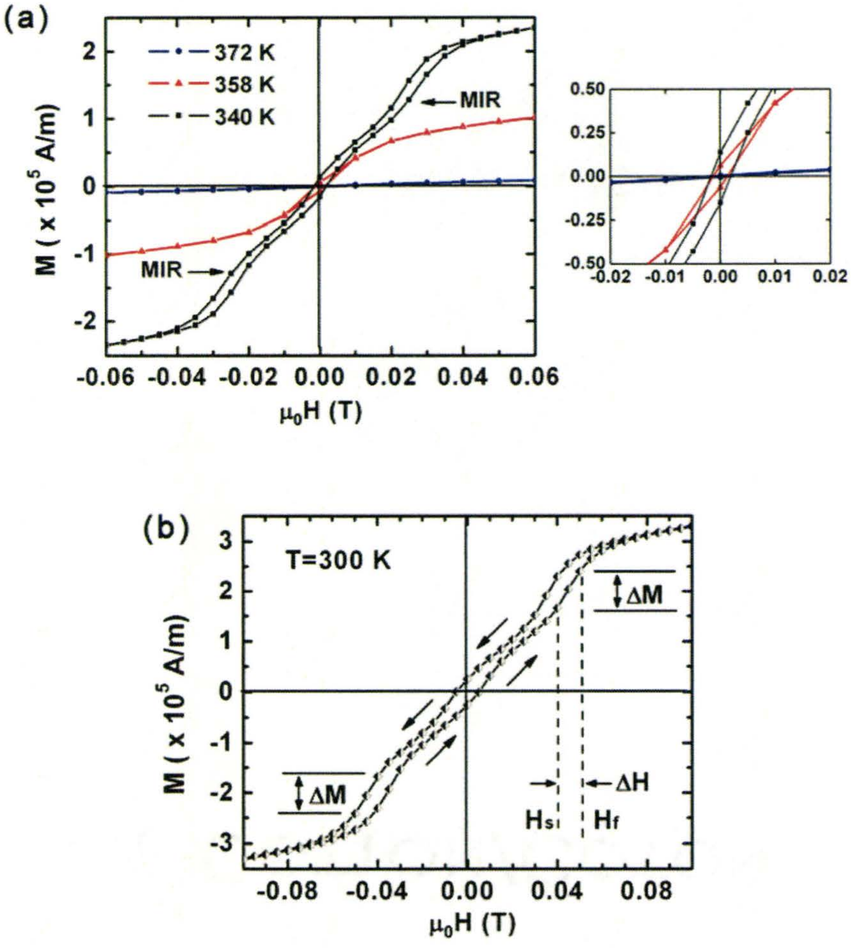

Figure 5.1: The in-plane magnetization hysteresis loops measured through the structural and magnetic phase transitions at (a) 372 K, 358 K, 340K and (b) 300 K, which correspond to pure austenite (blue circles), a mixture of austenite and martensite but where the austenitic phase is dominant (red triangles), a mixture of both phases but where martensitic phase dominates (black squares), and pure martensite (half white and half black diamonds). The MIR phenomenon, characterized by an abrupt increase in the magnetization, is observed at both 300 K and 340 K, where the martensitic phase is either phase-pure or predominating. The change in slope is easily recognized as the data points are evenly spaced in the applied magnetic field. The 300 K magnetization data is shown separately in figure 5.1(b) so as to clearly denote the onset (H_S) and completion (H_f) of the activation fields, as well as the magnetization increment (ΔM) induced by the MIR process. Note that the MIR effect is fully reversible. The inset to figure 5.1(a) gives an enlarged view of the magnetization in the vicinity of the origin (i.e. near $\mu_0 H = 0$). The sense of application and removal of the magnetic field is denoted by the arrows on figure 5.1(b).

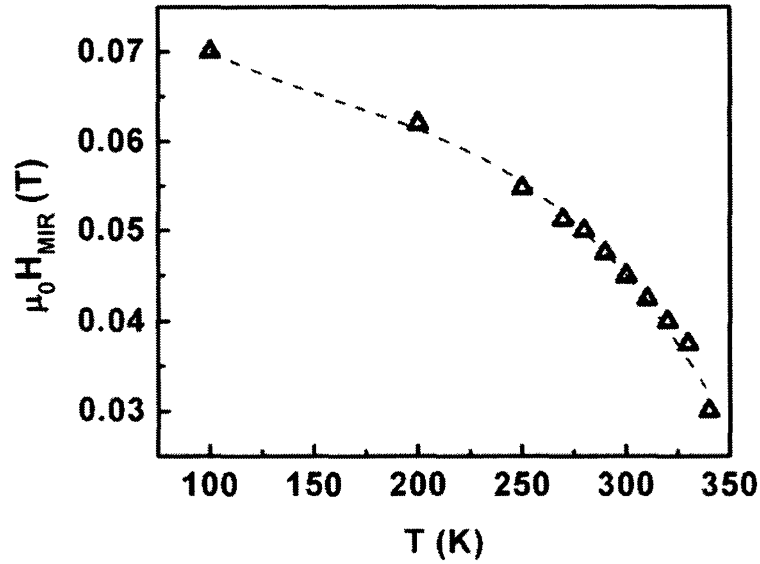

Figure 5.2: The critical magnetic field required to activate the MIR process as a function of temperature for a $Ni_{51}Mn_{29}Ga_{20}$ (at.%) film. HMIR decreases with increasing temperature, a response consistent with a reduction in the twinning stress due to enhanced thermal activation. The dashed line is a guide for the eye.

for single crystals and has been attributed to a drop in the twinning stress at elevated temperatures as well as the increased thermal activation of twin boundary motion (Straka *et al.*, 2006; Heczko & Straka, 2003; Peterson *et al.*, 2008; O'Handley *et al.*, 2006). It has been suggested that the latter effect facilitates the shuffling of atoms in the vicinity of the twin boundary to positions favored by the magnetic field (O'Handley *et al.*, 2006), which would account for the accelerated reduction in the activation field in the range of temperatures between 280 K to 340 K. Straka and coworkers (Straka *et al.*, 2006; Heczko & Straka, 2003) argued that the influence from the other temperature dependent magnetic/elastic properties, such as tetragonality (c/a) and the anisotropy constant (K_u), are of less significance.

5.2 Mechanism for the Self-Activated Reversibility in the MIR Effect

To fully understand the mechanism behind the MIR phenomenon, a comprehensive knowledge of the texture, microstructure and magnetic substructure is required.

5.2.1 Texture

The $\{400\}$ pole figures of both martensitic and austentic phase are presented in chapter 4. The pole configuration indicates that the film is composed of four crystallographic orientations, where each orientation gives rise to a single pole in the $\{400\}$ pole figures (4.9).

In order to obtain a more complete understanding of the crystallographic information, the $\{220\}$ pole figures were also generated, which are shown in figure 5.3. The (202) pole figure exhibits a single pole at a 90° radial angle while no such poles are observed for the $\{220\}$ and $\{022\}$ pole figures. This indicates that the film is exclusively [101] oriented. The $\{220\}$ and $\{022\}$ pole figures each show a ring of eight poles where the rings are at slightly different radial angles due to the orthorhombic nature of the unit cell. The fact that there are eight poles instead of the two expected for a single crystal (shown schematically for the $\{220\}$ pole figure in figure 5.3(b)) indicates that the film is comprised of four unique in-plane orientations. The azimuthal angle between these orientations is 90° as is depicted schematically in figure 5.3(c). The resulting fourfold symmetry is a reflection of the underlying symmetry of [100] cubic YSZ substrate. In such a pole pattern, the two {220} poles from orientation 2 (i.e. those labeled as "2" in figure 5.3(a)) can be rotated 180° into the two {220} poles from orientation 1, indicating the existence of a mirror relationship between these two orientations (i.e. (101) is the mirror plane). If these two orientations form two sets of martensite variants, then twin pairs will form when one variant lies on top of the other. Such an orientational relationship also exists between orientations 3 and 4. Because no such mirror symmetries exist between other orientations (i.e. those offset by 90° azimuthal angle) they cannot share a twinning relationship. It should be noted that the four orientations show similar XRD intensities, a clear indication of the equivalent volume fractions occupied by each orientation. Also noteworthy is the fact that the XRD^3 dataset reveals the presence of residual volumes of the austenite phase (see figure 6.1).

5.2.2 Microstructure

Figure 5.4 shows a cross-sectional TEM image of the $Ni_{51}Mn_{29}Ga_{20}$ (at.%) film. The image shows three distinct grains, each of which is highly twinned and comprised of plate-shaped variants. The two rightmost grains are quite similar in appearance, showing inclined thin slices within each martensite plate. These features likely originate from the micro-twins or slip-steps formed during the martensitic phase transformation. Such a microstructure results in a further reduction of the transformation strain while maintaining the martensitic crystal structure (Bhadeshia & Honeycombe, 2006). The leftmost grain is quite distinctive in appearance, showing no obvious substructures inside the stacked plates. The observation of grains having two distinct morphologies is consistent with the {220} pole figure result (figure 5.3) which shows in-plane crystallographic orientations offset by

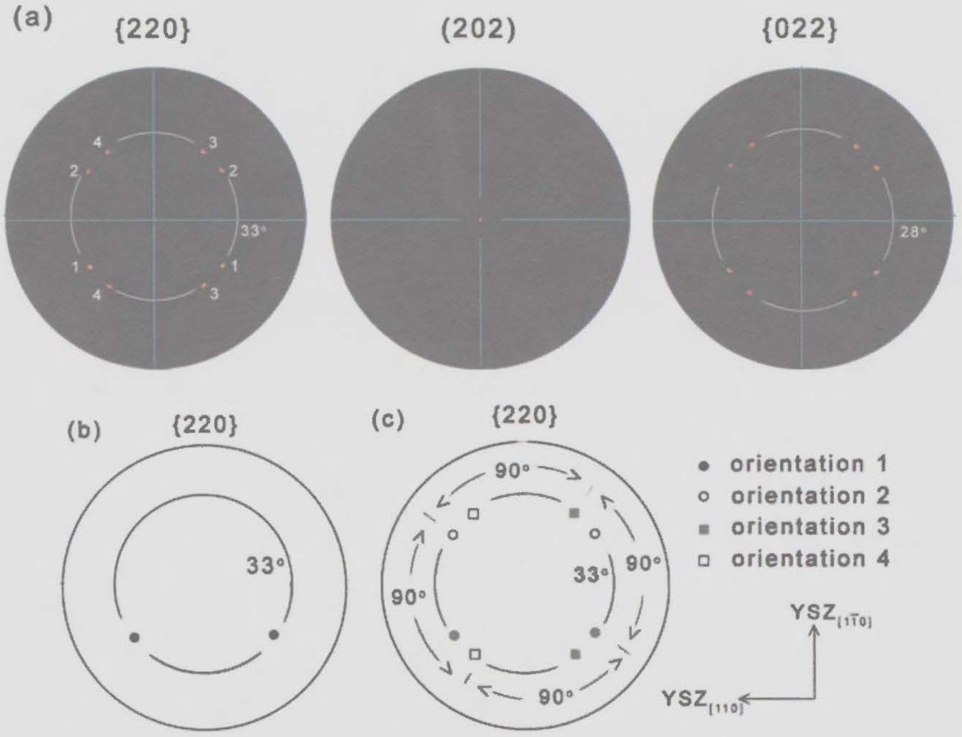

Figure 5.3: (a) The {220} set of pole figures for the martensitic phase of a $Ni_{51}Mn_{29}Ga_{20}$ (at.%) film. The observed patterns are consistent with a [101] oriented film with four in-plane orientations (poles originating from each orientation numbered 1 through 4). (b) A schematic depictions of the 220 pole figure expected for a [101] oriented single crystal. (c) A schematic depiction of the observed {202} pole figure showing four in-plane crystallographic orientations offset from one another by 90°. The Miller indices at the lower right corner of figure 5.3(c) show the orientation of the YSZ substrate relative to all the pole figures shown.

90°. Under such circumstances it is not unexpected for the slip-steps to be observed for one crystallographic orientation while being absent in a secondary orientation where the diffraction condition is not met. Also apparent in the image is a 2-3 nm interfacial layer which extends across the entire cross-section. If such a layer were of the austenite phase, which persists at room temperature due to substrate clamping effects, it would account for the residual levels of austenite detected in the XRD^3 measurements.

Figure 5.4: Bright-field TEM cross-sectional image showing the martensitic microstructure of the $Ni_{51}Mn_{29}Ga_{20}$ (at.%) film. The image shows three distinct grains each of which is comprised of a series of horizontal plates. Of note is the 2-3 nm thick feature at the film-substrate interface which is assigned to the austenite phase. The image was taken with the electron beam parallel to the [110] direction of the YSZ substrate (i.e. $E.B.\|[110]_{YSZ}$). The Miller indices indicating the orientation of the substrate is also provided.

5.2.3 Magnetic Domain Structure

Figure 5.5(a) shows a room temperature MFM image of the surface of the film. The image shows a spatially intricate magnetic domain structure where the out-of-plane component of the magnetization switches from being "in" or "out" of the surface of the film. Figure 5.5(b) is an atomic force microscopy (AFM) image simultaneously collected from the same area. The results indicate that the maze-like pattern represents the magnetic microstructure of the film as no similar topological patterns are observed in the film's surface morphology. Thus, it is expected that the small length-scale spatial undulation is a manifestation of the magnetization ripples associated with the various variants of this magnetic shape memory alloy. Similar MFM patterns of a rippling of the out-of-plane magnetization component

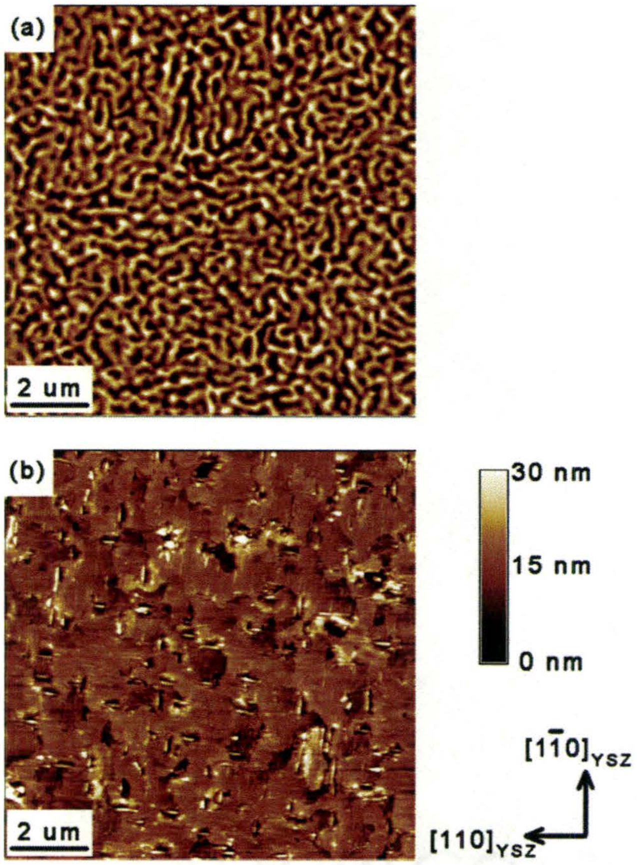

Figure 5.5: (a) MFM and (b) AFM images for a $Ni_{51}Mn_{29}Ga_{20}$ (at.%) film showing the magnetic force gradient and surface topography, respectively. The Miller indices at the lower right corner of figure 5.5(b) show the orientation of the YSZ substrate relative to both the images shown.

have been observed for (110) textured Ni-Mn-Ga films grown on Al_2O_3 (Chernenko *et al.*, 2005a) and MgO (Chernenko *et al.*, 2008) substrates as well as for epitaxial (001) Cu/Ni/Cu multilayers (O'Handley, 2000) and Ni-rich Ni-Fe thin films (Saito *et al.*, 1964).

5.3 Discussion

As previously noted, the $Ni_{51}Mn_{29}Ga_{20}$ (at.%) films studied here exhibit a MIR effect which is different from the corresponding effect observed in single crystals in that: (1) the activation field of 0.03∼0.07 T is approximately one-third of the amplitude required in single crystal (Straka *et al.*, 2006; Heczko & Straka, 2003), (2) the resultant increment in magnetization is only about 17% of the saturation magnetization whereas for a single crystal it is typically 50% (Straka *et al.*, 2006; Heczko & Straka, 2003) and (3) the MIR process is self-reversible whereas for single crystals it is reversible only under an external stimuli (Murray *et al.*, 2000; Straka & Heczko, 2005; Straka *et al.*, 2006). It has also been noted that the film microstructure and texture is strongly influenced by the crystallographic orientation of the substrate material, exhibiting a character that is quite different from that observed for single crystals. The present results suggest that these microstructural properties give rise to a unique magnetic domain pattern which, in turn, manifests itself in a distinctive MIR response, as discussed below.

A detailed understanding of the film's microstructure can be ascertained from a comparison of the crystallographic texture results and the TEM images. The texture indicates that the film is comprised of four different crystallographic orientations, where each orientation has its [101] direction normal to the surface of the substrate but offset by 90° in the film plane. These orientations exhibit a fourfold in-plane symmetry and are of significance since orientations offset by 90° have no single crystal analogue. This arrangement is, in fact, inherited from the crystallographic texture associated with the austenite parent phase formed during the deposition process. The parent phase adapts to the underlying four-fold symmetry of the substrate's (001) cubic surface through the formation of two geometrically equivalent grain orientations characterized by $(110)[001]_{film}||(001)[110]_{substrate}$ and $(110)[001]_{film}||(001)[1\bar{1}0]_{substrate}$, as displayed in figure 5.6(a). The subsequent austenite to martensite phase transformation results in martensite twin variants forming in both grain orientations which gives rise to two additional crystallographic orientations. Variants within the individual grains form twins as shown in figure 5.6(b). This twinning relationship is characterized by a pair of martensitic variants connected by a twin boundary, where the variants appear in the $\{220\}$ pole figures (or alternatively $\{400\}$ pole figures shown in figure 4.9) as poles separated by a 180° azimuthal angle (i.e. denoted as orientation 1 and 2 or orientation 3 and 4 in figure 5.6(a)) with the twin boundary corresponding to the (101) mirror plane. Of crucial importance is the fact that the variants formed within one grain orientation do not share a twinning relationship with variants formed within the other grain orientation because the two sets of perpendicularly oriented grains are inherited from the austenitic phase rather than formed through the martensitic transformation. Such an argument is consistent with the texture results indicating that the crystallographic orientations offset by a 90° azimuthal angle do not show mirror symmetry. This description is consistent with the two unique grain-types observed in the TEM cross-sectional image. Also in agreement with this description is the fact that the TEM image shows well-defined straight interfaces between the martensite plates running parallel to the surface of the substrate (see figure 5.4), a feature indicative of the high degree of atomic coherency achieved through a twinning relationship. The fact that these boundaries are parallel to the substrate surface is consistent with the texture results which allow for an inter-variant (101) twin-plane as is schematically depicted in figure 5.6(b).

The two distinct grain types give rise to unique grain boundaries as is shown in figure 5.4. The leftmost grain boundary, which is somewhat jagged in appearance, occurs when

(a) Grain structure for the austenitic phase

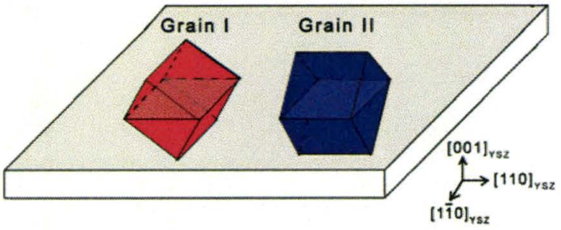

(b) Grain structure for the martensitic phase

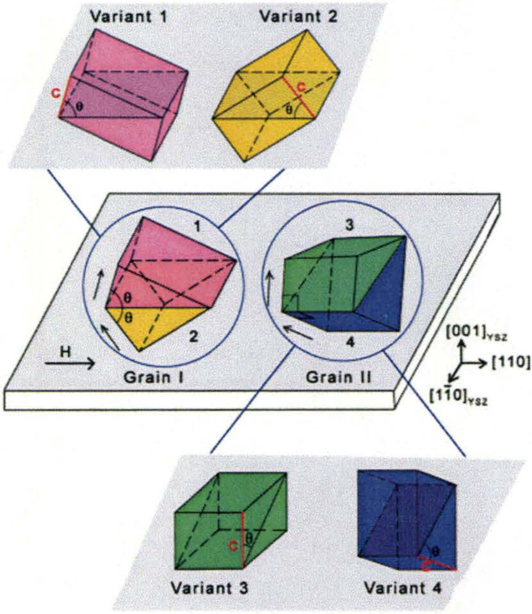

Figure 5.6: Schematic representation of the grain structure for the (a) austenitic phase and (b) martensitic phase in a $Ni_{51}Mn_{29}Ga_{20}$ (at.%) film. For the austenite phase two equivalent grain orientations offset by an in-plane angle of 90° are formed through the adaptation to the substrate's (001) cubic surface. The subsequent martensitic transformation leads to twin variants generated in each grain orientation. Variant 1 and 2 form a twin pair within Grain I while the variant 3 and 4 share a twinning relationship within Grain II. The twin boundary which connects the two twin variants is the (101) plane of the unit cell. The crystallographic orientation of each individual variant is also shown. Unique to each orientation is its c-axis direction as is emphasized in red. The variants are numbered 1 through 4 in (b). The direction of the applied magnetic field as well as the magnetization direction for each variant is denoted by an arrow. The Miller indices at the lower right corner of both (a) and (b) show the orientation of the YSZ substrate relative to all the martensitic variants shown.

two grains offset by a 90° azimuthal angle meet. The rightmost grain boundary, on the other hand, forms a sharp interface normal to the surface of the substrate. This feature is likely the result of a small angle grain boundary formed between the two like-oriented grains.

With the present understanding of the crystallographic texture and microstructure, it is possible to gain insight into the magnetic microstructure of these films. It should, however, be first mentioned that the easy magnetic axis in an orthorhombic martensite is along the shortest c-axis of the unit cell (i.e. along [001]) (Sozinov *et al.*, 2002a). In this scenario, it is apparent from figure 5.6(a) that the direction of the magnetization direction for each variant is neither parallel nor perpendicular to the film's surface, but instead forms the angle (θ). For this arrangement the normal component of the magnetization for any particular variant can point either towards the film's surface or away from it. The maze-like appearance of the MFM image (figure 5.5(a)) is consistent with these arguments as an undulation in the magnetization could form closure domains and thus effectively reduce the magnetostatic energy (O'Handley, 2000; Muller, 1961) through the formation of a ripple domain structure (Saito *et al.*, 1964; Hubert & Schafer, 1998). It should be noted that although the magnetization of these variants are denoted by an upward pointing arrow, it is equally likely that the magnetization direction could also point downward, as is apparent from the ripple domain structure. One can expect that to avoid generating poles at the twin boundary, the two twin-related variants within Grain I or Grain II should have their magnetization directions pointing both up or both down.

The in-plane magnetization hysteresis loops, shown in figure 5.1, reveal that the films exhibit a reversible MIR effect, which is similar to that observed for $\{100\}$ oriented orthorhombic Ni-Mn-Ga films (Thomas *et al.*, 2008a). For this effect to be observed, there must exist a mechanism for promoting reversibility as well as a means by which a reorientation of variants can occur while keeping the film clamped to the underlying substrate. As mentioned previously, the self-reversibility for the MIR effect in a $\{100\}$ oriented film was attributed to substrate-imposed stresses that developed during the reorientation of the in-plane lattice constants of an orthorhombic unit cell (Thomas *et al.*, 2008a,b). These stresses force the film back to its initial state once the field is removed. While this provides a description of the MIR effect in the $\{100\}$ oriented films presented by Thomas *et al.* (Thomas *et al.*, 2008b), the same description cannot be applied to the behavior observed for the [101] films studied here. This is a consequence of the fact that the two variants which convert from one to the other, have an identical epitaxial relationship with the substrate (i.e. $(101)[010]_{film}||(001)[110]_{substrate}$ for Variant 1 and 2, and $(101)[010]_{film}||(001)[1\bar{1}0]_{substrate}$ for Variant 3 and 4, as shown in figure 5.6(b)). Thus, when Variant 1 and 2 (or alternatively Variant 3 and 4) switch from one to the other, no change is required in the in-plane lattice parameters and, as a result, no substrate-imposed stresses will develop. The presence of the 2-3 nm thick austenite layer at the substrate-film interface (figure 5.4) should also help facilitate the MIR process as the layer disconnects the martensite variants from the underlying substrate. As a result, the stresses imposed by the substrate on the martensite grains above the austenite layer are expected to be significantly smaller. In the absence of the substrate-imposed stresses a [101] single crystal film should behave exactly as a single crystal, showing a complete MIR effect which does not display self-reversibility. The fact that a reversible MIR effect is observed requires that a different mechanism comes into play for these [101] oriented Ni-Mn-Ga films. An analysis of the response of the individual variants to an externally applied field reveals that the microstructure itself is the most likely origin of the reversibility.

Labeled on figure 5.6(a) is the direction of the externally applied magnetic field (i.e. $H||[110]_{YSZ}$) relative to the four crystallographically oriented variants. Immediately evident is the fact that the magnetic field direction relative to the magnetization direction varies between variants and in no case are the two directions ever parallel. It is apparent from an examination of the magnetization directions labeled on the individual variants that the magnetization of only one of the twin variants in Grain I has a component parallel to the external field. This component makes this variant more favorable than its twin related counterpart whose same magnetization component is antiparallel to the field. A preferential field selection, however, is not expected to occur between Variants 3 and 4 since neither shows a magnetization component in the direction of the magnetic field. The arrangement described will inevitably lead to a spatially varying MIR response which is dependent on the local microstructural and crystallographic environment.

For the scenario where there exists a twin boundary between Variants 1 and 2 (Grain I in figure 5.6(b)), there will exist a difference in the Zeeman energy between these variants which is given by,

$$\Delta E = 2\mu_0 M_s H \cos\theta \tag{5.2}$$

where μ_0 is the magnetic permeability of free space and M_s is the saturation magnetization, H is magnetic field and θ is an angle between the magnetization direction for a variant and the magnetic field. This difference in energy results in the application of a pressure on the twin boundary which, for fields in excess of H_{MIR}, can drive the twin boundary motion in a manner that favors Variant 1 at the expense of Variant 2. A similar situation has been discussed by O'Handley who pointed out that the field-induced twin boundary motion occurs when strong magnetic anisotropy is present (Handley, 1998). If the Zeeman energy is much smaller than the magnetic anisotropy (i.e. M_sH/2K$_u$ $<<$ 1) then the effect of the field is to move the twin boundaries rather than to rotate the magnetization within unfavorably oriented variants. In an effort to examine whether the films presented here belong to this category, we estimated the Zeeman energy, M_sH, for a MIR-activation field of u_0H_{MIR} = 0.045 T and a saturation magnetization of 4.2×10^5 A/m at 300 K. For this scenario, the value of the Zeeman energy is of the order of 10^4 J/m^3. This value is an order of magnitude smaller than the magnetic anisotropy energy, 2K$_u$, which is on the order of 10^5 J/m^3 (Soderberg *et al.*, 2005). This result indicates that the strong anisotropy assumption used for the films presented in this report is reasonable. The elastic energy introduced by the twin boundary motion, $\sigma\varepsilon/2$, is also estimated for a twinning stress of 2 MPa (Soderberg *et al.*, 2005) and a 5% strain. While a 10 % strain is predicted theoretically for a single crystal with similar lattice parameters (i.e. c/a = 0.9) upon the completion of the MIR process from the single variant state with a field applied parallel to the hard [100]-axis, the 5% value used here is a more reasonable estimation. This reduced value takes into account such factors as the twin variants existing in these textured films before the onset of the MIR process and that the magnetic field was applied parallel to the twin boundary instead of being parallel to the magnetization direction of one of the two variants. The calculation indicates that the elastic energy density is also on the order of 10^4 J/m^3, as is the case for the Zeeman energy. This implies that with an applied field of 0.045 T it is possible to induce twin boundary motion. O'Handley has determined that the magnetic driving force on the twin boundary is strongest when the external field is applied parallel to the twin boundary and bisects the angle between the magnetization of the twin variants under consideration (Handley, 1998). This geometry accurately describes the case presented here. It is also evident that magnetic domain wall motion is absent during the magnetic field-induced twin boundary motion in the Ni-Mn-Ga system (Lai *et al.*, 2007). Considering all these aspects, the MIR effect observed here is very likely induced by the

Zeeman energy difference between the two twin-related variants.

It should be understood that the aforementioned reorientation mechanism is not possible in the second scenario (i.e. for variants in Grain II) shown in figure 5.6(b). In this case, both variants (i.e. Variant 3 and 4 in Fig. 7b) have their c-axes perpendicular to the magnetic field direction and, hence, do not experience any difference in Zeeman energies. As a result, there is no incentive to convert from one orientation to the other through twin boundary motion. It is also considered unlikely that the variants in Grain II experience any MIR effect as a result of being in contact with a variant from Grain I, because there is no twinning relationship between them. Thus the geometrical arrangement of the grain orientations results in 50% of the film's grains being able to participate in the MIR process (i.e. MIR-active) and 50% of the film's grains being MIR-inactive. It should be understood, however, that the inactive variants possess all of the material properties necessary to become MIR-active, as the inactivity arises solely from their crystallographic orientation relative to the applied magnetic field. For the MIR-active grains, one of the two variants will be oriented favorably with respect to the field while the other will have an incentive to reorient when the magnetic field is applied, resulting in a maximum of 25% of the film variants reorienting.

The presence of these MIR-inactive variants also accounts for the small increase in magnetization during the reorientation process when compared to single crystals. The fact that the magnetic reorientation is confined to preexisting twin-related variants within individual grains also accounts for the relatively small MIR activation field compared to the field reported for single crystals. By contrast, the samples used in the single crystal experiments were magnetically or mechanically forced to become a single variant in order to achieve the maximum possible strain from the MIR effect (Murray *et al.*, 2000; Straka &

Heczko, 2005; Straka *et al.*, 2006). In this case the activation field must be large enough to provide the nucleation energy to first produce the twins and then to overcome the stresses induced by the twin boundary motion. The experiments with thin films described here are more akin to stress-induced elastic twinning observed for calcite, where the initial nucleation step was bypassed, which resulted in the deformation being realized using a much smaller load (Williams & Cahn, 1963). The small activation field for the MIR effect observed here is attractive from a device perspective, especially for applications where strong magnetic fields are considered undesirable due to possible interference between the field and other electronic components.

While only 50% of the grains are active in the magnetic reorientation process, the other 50% are not considered to be completely passive in nature. During the process of twin boundary motion, the atoms in those variants undergo twinning shear along the $[10\bar{1}]$ direction, a lateral direction parallel to the substrate's surface. The twinning shear in the active grains must be accommodated by the elastic distortion of inactive grains. This will lead to the development of large elastic stresses in the inactive grains, making them plastically hard elements within the substructure of the film. With no effective means by which to relieve these stresses it is expected that the atoms in active grains are forced back to their initial positions when the external magnetic field is removed. Such a partition of stress between a "hard" parent phase and a "soft" twin, has recently been observed using three-dimensional x-ray diffraction in magnesium alloys subjected to compressive loading (Aydiner *et al.*, 2009). In addition, reversibility of the twinning transformation has been observed in bulk polycrystalline samples of Ni-Mn-Ga where the phenomenon was attributed to a restoring force arising from differently oriented crystallites (Gutierrez *et al.*, 2006). In contrast to the polycrystalline material, the highly textured films appear to be far more effective in the reorientation process, displaying a larger magnetization increment that is induced by a smaller magnetic field. Within this framework a [101] oriented film without MIR-inactive grains should be capable of producing a more complete MIR effect, but the effect would not be completely self-reversible.

Present results suggest that the substrate plays a crucial role in determining the initial crystallographic texture and microstructure of the films, but plays a more passive role in controlling the MIR response. The existence of the in-plane grain orientations offset by 90° is a consequence of the adaptation of the [110] oriented Ni-Mn-Ga parent phase to the fourfold symmetry of the YSZ substrate's (001) cubic surface. During the subsequent austenite to martensite phase transformation, the substrate constraints to the austenite lattice lead to a 2$\sim$3 nm residual austenite layer at the film-substrate interface. It suggests that, while the substrate must hinder the degree of atomic shuffling during the martensitic phase transformation the stresses imposed on the martensitic grains above the austenitic layer are significantly weakened. Interfacial stresses are sufficiently relieved through various strain relaxation mechanisms such as dislocations and the grain boundaries. Once the stresses are relieved the substrate becomes less of a factor. This, combined with the fact that each of the four crystallographic orientations share an identical epitaxial relationship with the substrate, makes it highly unlikely that the substrate is producing any appreciable stresses as one variant converts to the other. On the contrary, the shearing of the atoms during twin boundary movement is strongly inhibited at grain boundaries due to the presence of MIR-inactive grains. It is the initial formation of these structures during film growth where the substrate must play a decisive role. This leads to the intriguing possibility of engineering a desired response based on an appropriately chosen substrate material, through graphoepitaxy, or through the promotion of a step-flow growth mode facilitated by a miscut substrate. Successful implementation of such strategies could lead to the ability to tune the film's structural and magnetic microstructure towards a particular application where, for example, MIR-inactive grains could be included or excluded to achieve either self-activated reversibility or allow a more complete, but irreversible, MIR effect.

Chapter 6

Magnetocaloric Effect in Ni-Mn-Ga Thin Films

The shape memory effect in ferromagnetic shape memory alloys is reliant upon two phase transitions: (1) an austenite to martensite structural transition and (2) a paramagnetic to ferromagnetic transition. Once the alloy is cooled to temperatures where it is both ferromagnetic and martensitic, it can exhibit a large deformation when exposed to an external magnetic field. Shape recovery ensues if the sample is subsequently transformed back to the austenitic phase upon heating through the reverse structural phase transition. In addition to the ferromagnetic shape memory effect, the magnetic transition can also induce a negative magnetic entropy change near the Curie temperature, a phenomenon commonly referred to as the magnetocaloric effect (MCE) (Gschneidner & Pecharsky, 2000).

The strength of the MCE effect in the Ni-Mn-Ga system is highly dependent on the relative positions of the characteristic temperatures associated with the aforementioned structural and magnetic phase transitions (Pareti *et al.*, 2003). It has been determined that the characteristic temperatures are related to the electron to atom ratio (e/a) corresponding to a particular alloy composition. For small ratios (i.e. e/a < 7.7) the start temperature for the martensitic transition (M_s) is far below the Curie temperature (T_c) while the reverse tendency occurs for larger ratios (i.e. e/a > 7.7) (Chernenko, 1999). The behavior in the intermediate range (i.e. e/a ≈ 7.7), where the two transitions overlap (Chernenko, 1999; Borisenko *et al.*, 2005), is by far the most distinctive and complex. It is for these compositions, and within the temperature interval where the phase transitions occur, that give rise to the largest MCE (Pareti *et al.*, 2003; Zhou *et al.*, 2004; Long *et al.*, 2005; Khan *et al.*, 2006). The considerable changes to the entropy that occur during the magnetizing or demagnetizing of MCE materials can be utilized in refrigeration cycles (Wood & Potter, 1985). The refrigeration process takes advantage of the fact that the entropy of the spin system will increase as it undergoes adiabatic demagnetization, whereby cooling occurs as the required entropy is extracted from the crystalline lattice. Giant MCE responses with $\Delta S =$ -86 J/kg-K have been reported (Pasquale *et al.*, 2005) in bulk Ni-Mn-Ga crystals at 312.75 K for magnetic fields ramped to 5 T, demonstrating the promise of these alloys as magnetic refrigerant materials. While research in this direction has progressed considerably for bulk Ni-Mn-Ga alloys, there exist no reports characterizing the effect for thin films. This is despite the fact that films are excellent candidates for micro-length-scale magnetic refrigeration applications such as spot cooling in microelectromechanical systems (MEMS) (Gass *et al.*, 2008) and micro energy storage devices (Morelli *et al.*, 1996).

In our $Ni_{51}Mn_{29}Ga_{20}$ (at.%) films, an overlap of the magnetic and martensitic phase transformations was observed, suggesting the possibility of a large MCE. In this chapter, we make a systematic characterization of the coexisting magnetic and structural phase transformations as well as the magnetic entropy change associated with these transitions. An understanding of the role each phase transition plays in determining the level of enhancement to a standard MCE governed only by the ferromagnetic phase transition is given.

6.1 Martensitic Phase Transformation

The structural phase transition for the $Ni_{51}Mn_{29}Ga_{20}$ (at.%) films was directly observed using the three dimentional XRD technique (XRD^3). The analysis of the intensities of the (400) and (004) martensite and the (400) austenite reflections during the heating and cooling sequence allows for the characterization of the structural phase transitions based on the relative intensities of these diffraction peaks. Figure 6.1 shows the progression of the peak intensities as the film is heated from 233 to 371 K and then cooled back down to 233 K. Observed at the high and low temperature extremes of the sequence is a response dominated by the cubic austenitic and orthorhombic martensitic phases, respectively. Between these two extremes there exists a mixed response of varying degree which characterizes the phase coexistence, a feature typical for a first-order phase transition. The back and forth transformations between the martensitic and austenitic phases, and the associated hysteresis, are quite apparent. Noteworthy is the fact that even at the lowest temperature there exist residual amounts of the austenitic phase. This observation is consistent with the room-temperature transmission electron microscopy images which show a 2-3 nm thick austenite layer at the film-substrate interface (figure 5.4). Also evident from the data is the complete reversibility of the martensitic transformation.

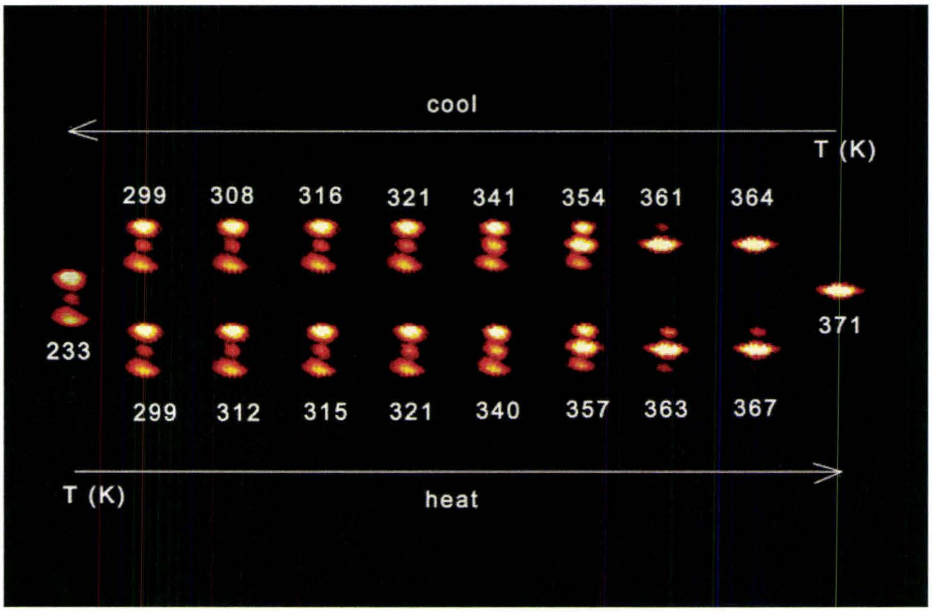

Figure 6.1: XRD[3] data showing the structural phase transition for a $Ni_{51}Mn_{29}Ga_{20}$ (at.%) film as the temperature is cycled back and forth through the martensite-austenite phase transition. The data at 371 K shows only a single (400) peak for cubic austenitic phase while the 233 K data shows the (400)/(004) peak splitting expected for the orthorhombic martensitic phase. Occurring between these two temperature extremes is a first-order martensitic phase transformation where one phase gradually transforms into the other. In this temperature regime, all three peaks are visible due to the austenite-martensite phase coexistence. Note that the phase transition is completely reversible and exhibits a hysteresis. Also noteworthy is the existence of an extremely weak peak between the two martensite peaks at 233 K, a feature consistent with residual levels of the austenitic phase.

Extracted from the data in figure 6.1 were the volume fractions for the austenitic and martensitic phases over the entire heating-cooling cycle. The values were determined by comparing the integrated peak intensities in the two-phase regions to those obtained at high and low temperatures where a single phase dominates (i.e., 371 K and 299 K). This methodology yields temperature dependent volume fractions for the austenitic (f_A) and martensitic (f_M) phases which are given by:

$$f_A(T) = \frac{I_A(T)}{I_A(371K)}, \quad f_M(T) = \frac{I_M(T)}{I_M(299K)} \tag{6.1}$$

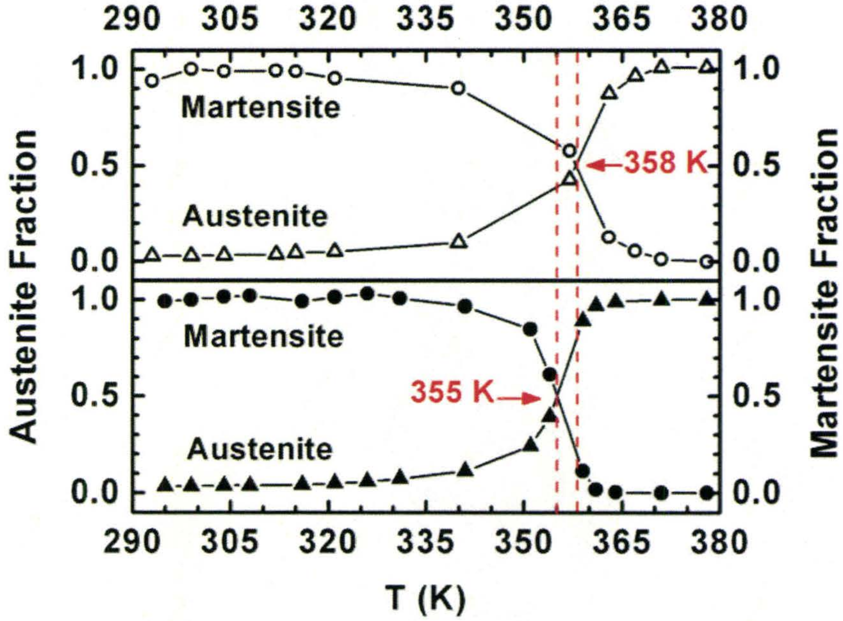

Figure 6.2: Temperature dependence of the volume fractions for the martensitic (circles) and austenitic (triangles) phases during the heating (top) and cooling (bottom) processes. The dashed lines denote the temperatures corresponding to T_{50}^{cool} = 355 K and T_{50}^{heat} = 358 K (i.e. where the volume fractions for the two phases are equal). The fact that these values are offset by about 3 K is a clear indication of the hysteresis in the phase transformation. The line connecting the data points is a guide for the eye.

where I_A and I_M are the integrated intensities of the (400) pole from the austenitic phase and the (040) pole from martensitic phase, respectively. Figure 6.2 shows the temperature dependence of the austenite and martensite volume fractions as obtained from the XRD measurements for both the heating and cooling sequences. The data reveal a hysteresis in the first-order martensitic phase transformation and allows for the extraction of the values T_{50}^{cool} = 355 K and T_{50}^{heat} = 358 K, which define the temperatures where the film is comprised of equal amounts of the austenitic and martensitic phases during the cooling and heating sequences, respectively.

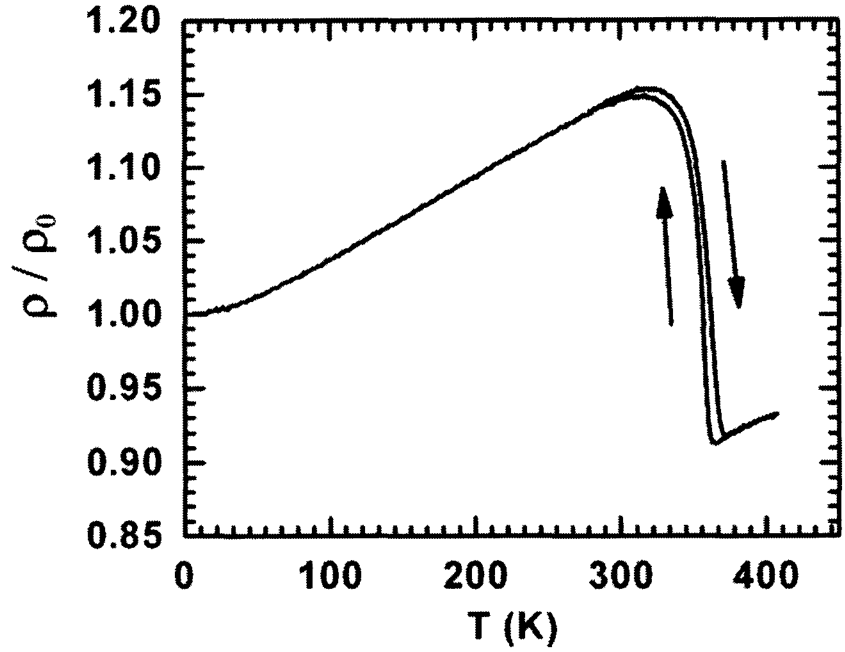

Figure 6.3: Temperature dependent DC resistivity measured using the van der Pauw technique. The characteristics show a reversible martensitic transformation in the temperature range of 307 to 370 K. All values were normalized to the resistivity (ρ_0) of the films at 7 K.

The temperature dependence of the resistivity for the $Ni_{51}Mn_{29}Ga_{20}$ (at.%) films was measured for temperatures between 7 and 400 K. The results shown in figure 6.3 reveal a well defined hysteretic feature extending from 307 to 370 K which is consistent with the martensitic phase transformation observed with XRD[3]. Using the deviation from linearity in the slope of the resistivity-temperature characteristics as a criterion for the beginning and ending of the phase transformation, the martensite to austenite transformation start (M_s) and finish (M_f) temperatures, as well as the austenite to martensite transformation start (A_s) and finish (A_f) temperatures, were determined to be M_s = 361 K, M_f = 307 K, A_s = 312 K and A_f = 370 K. With no other resistivity anomaly present in the data down to 7 K it is likely that films have no inter-martensitic transformations.

6.2 Ferromagnetic Phase Transition

Temperature dependent DC magnetization measurements, carried out in a magnetic field of μ_0H = 0.005 T, were used to probe the ferromagnetic phase transition. The results, shown in figure 6.4, reveal the existence of a ferromagnetic transition in the temperature range between 352 and 360 K, which shows a hysteresis between the cooling and heating sequences as well as a Hopkinson-like peak (Chernenko *et al.*, 2005b). The peak, centered around 352 K, has a lower maximum value in the heating process than it does in the cooling sequence. There does exist, however, a cross-over point at 356 K demarcating a 7 K temperature interval where the observed magnetization during the heating sequence is somewhat higher. Of the utmost importance is the fact that the magnetic phase transition overlaps with the structural transition observed in the XRD[3] and resistivity measurements. This scenario, while only rarely reported for Ni-Mn-Ga films, has been attributed to the composition of the alloy (Jin *et al.*, 2002) and is responsible for the observed hysteresis in the temperature interval of the magnetic transition.

While the overlap in the structural and magnetic phase transitions complicates the magnetization data considerably, it is still possible to extract the Curie temperature, (T_c^A), through suitable processing of the dataset. This temperature is typically obtained from the inflection point in the magnetization's temperature dependence, but such a procedure is ineffective here due to the complex shape of the magnetization curve (figure 6.4). An alternative method relies on an Arrott plot (Arrott, 1957) which determines the Curie temperature from the measured magnetization isotherms. The method requires that the magnetization be plotted in the form of M^2 versus H/M where a linear extrapolation of the high

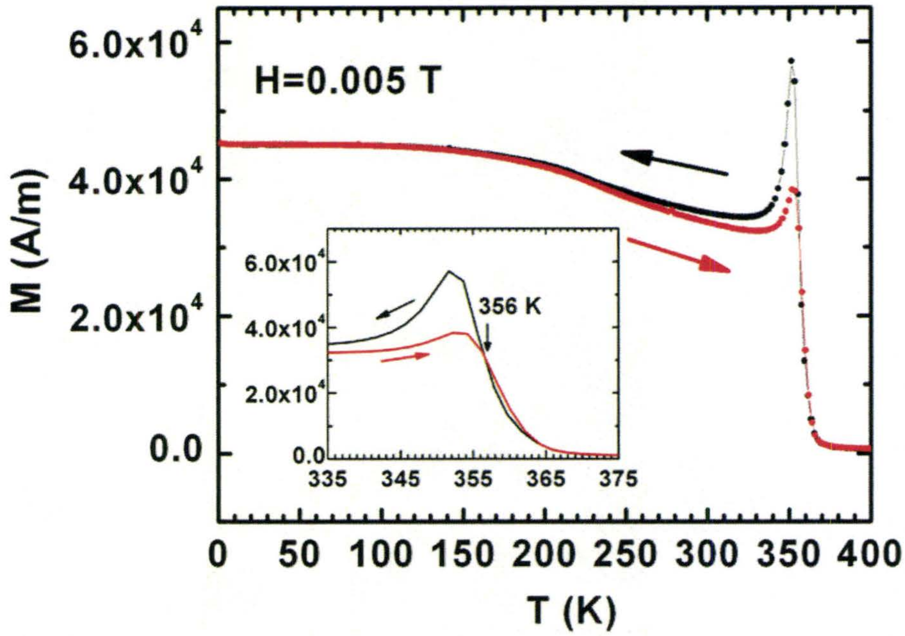

Figure 6.4: Temperature dependent DC magnetization for a $Ni_{51}Mn_{29}Ga_{20}$ (at.%) film in an external magnetic field of 0.005 T, for both the cooling (black) and heating (red) sequences. The magnetization curves show a Hopkinson-like peak near 352 K and a hysteresis between the cooling and heating sequences due to the concurrent structural and magnetic phase transitions. The inset shows an expanded view for the temperature interval across the magnetic phase transition, which reveals a cross-over in the magnetization curves at 356 K.

field data to the zero magnetic field yields the square of the spontaneous magnetization, M_0^2. In the ferromagnetic region (i.e. $T < T_c$), M_0^2 is positive (Aharoni, 1996) while in the paramagnetic region (i.e. $T > T_c$) it is negative (i.e. the M^2 versus H/M curve intercept the H/M-axis) (Aharoni, 1996). At $T = T_c$ the spontaneous magnetization is zero and, thus, the M^2 versus H/M curve passes through the origin. The low field data is excluded from the extrapolation because it represents an averaged response over differently oriented magnetic domains (Aharoni, 1996).

In this study, the magnetization isotherms used to generate the Arrott plots were measured in a cooling sequence (figure 6.5) since the onset of ferromagnetism is more accurately determined than is its disappearance (Arrott, 1957). It is also noted that the Curie temperature of the martensitic phase, T_c^M, differs significantly from that of the austenitic phase (Chernenko *et al.*, 2003; Khovaylo *et al.*, 2005) due to the different crystal structure of the two phases. This is not surprising since the spin exchange interactions, responsible for the magnetic ordering, are dependent upon the Mn-Mn interatomic distances in the unit cell. And the Mn-Mn interatomic distances are different for the austenitic and martensitic lattices (Chernenko *et al.*, 2003). The T_c temperature determined here through the Arrott plots is the Curie temperature of the austenitic phase, T_c^A, since the magnetization isotherms used are measured at the temperatures where austenite is the predominant phase (i.e. those measured at $T > 355$ K). In fact, for the films studied here, the Curie temperature of the martensitic phase, T_c^M, is a virtual temperature since it is well above the temperatures where the martensitic phase persists. This is apparent from the temperature dependent DC magnetization (figure 6.4) which does not show any anomalies below the martensitic transformation finish temperature of 307 K. Such a virtual transition temperature can still be estimated through orthodox Landau theory (Chernenko *et al.*, 2003) but this aspect is beyond the scope of this paper. The important point being made here is that the two phases spontaneously magnetize at different temperatures and the magnetic transition that overlaps with the martensitic transformation is the one exhibited by the austenitic phase. To determine the Curie temperature of the austenitic phase, T_c^A, the M^2 versus H/M curves were measured in the temperature range of 356 $\sim$ 362 K, where the austenitic phase predominates ($T_{50}^{cool} = 355$ K), as shown in figure 6.6. At 360 and 362 K, the linear extrapolation of the high field data ($\mu_0 H > 0.4$ T) intercepts the H/M-axis while at 356 and 358 K it intercepts the M^2-axis. This indicates that the T_c^A temperature is around 359 K. This value is consistent with that observed for bulk Ni-Mn-Ga samples of similar composition

(Ullakko *et al.*, 2001). For the purpose of comparison, the 352 K and 354 K isotherms, where the response is dominated by the martensitic phase, are also presented in figure 6.6. The fact that these two curves exhibit very different curvatures at high fields as compared to the 356 ~ 362 K data is consistent with the argument that the martensitic and austenitic phase each has a different magnetic response and Curie temperature.

It should be noted that the Arrott plot is based on the equation of state (Arrott & Noakes, 1967): $(H/M)^{1/\gamma} = (T-T_c)/T_1 + (M/M_1)^{1/\beta}$. By plotting M^2 versus H/M, it is assumed that the critical exponents γ and β follow mean field theory (i.e. $\gamma = 1$, $\beta = 1/2$). The 356 ~ 360 K plots shown in figure 6.6, however, display curvature even at high fields, indicating that the actual critical exponents for the austenitic phase of the Ni-Mn-Ga system deviate from mean field values. The degree of deviation is not significant since these plots are still parallel at higher fields (μ_0H > 0.4 T). To estimate the deviation between the actual Curie temperature and the one derived from the mean field model, various critical exponents have been examined in the range defined by the mean field ($\gamma = 1$, $\beta = 1/2$) and Heisenberg model ($\gamma = 1.386$, $\beta = 0.365$) (Pramanik & Banerjee, 2009). These two models, for the most part, define the range of γ and β values for crystalline ferromagnets. From this examination it is found that the T_c values obtained always fall within the temperature range of 357 ~ 359 K. This indicates that mean field theory does not significantly overestimate the Curie temperature and validates the 359 K onset for the ferromagnetic ordering of the austenitic phase. It is noted that this trial-and-error process is not the standard method used for determining the critical exponents. The correct method requires a fit of the experimental data to the equation of state (Arrott & Noakes, 1967) and power-law dependence (Stanley, 1971) using the iterative approach described by Pramanik and Banerjee (Pramanik & Banerjee, 2009). Unfortunately, such an iterative process is not possible

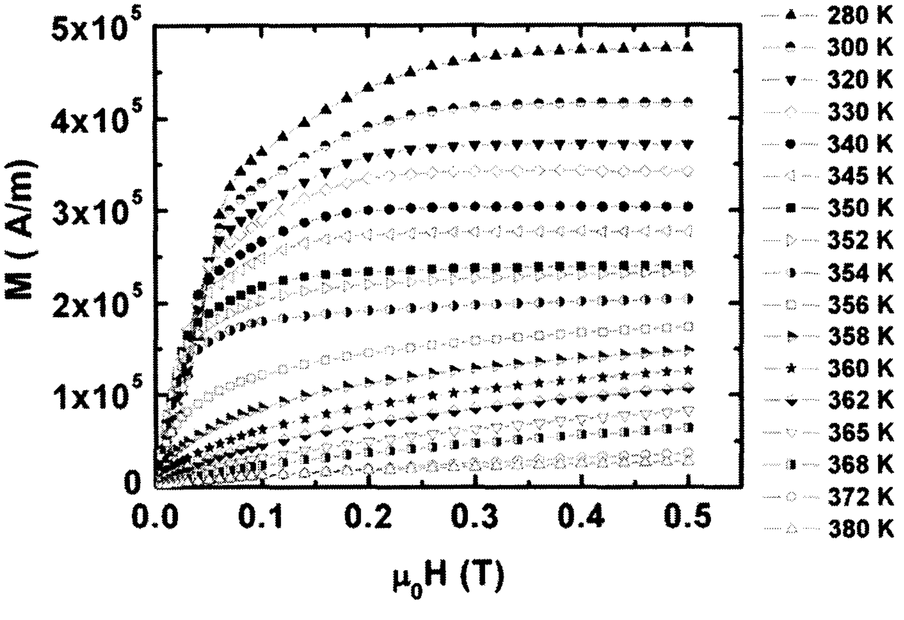

Figure 6.5: The isothermal magnetization curves for a $Ni_{51}Mn_{29}Ga_{20}$ (at.%) film measured at different temperatures, which extend through the magnetostructural phase transformation.

here due to the coexistence of the martensitic transformation. As a result of the overlapped structural and magnetic transition, nearly all of the magnetization isotherms measured below the T_c temperature contain a strong signal from the martensitic phase and, thus, cannot be used in the fitting procedure for the estimation of the Curie temperature of the austenitic phase. While it is not customary to use the trial-and-error process described above, it does provide a means by which to evaluate the mean field value.

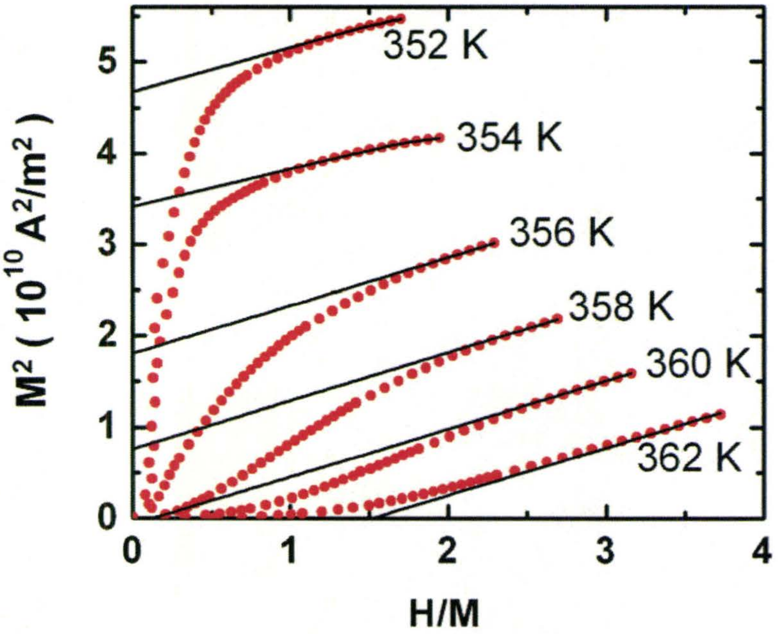

Figure 6.6: M^2 versus H/M plots for a $Ni_{51}Mn_{29}Ga_{20}$ (at.%) film derived from isothermal magnetization data for temperatures between 352 K and 362 K. A linear extrapolation of the high field data for 356 ~ 362 K curves were used to estimate the Curie temperature of the austenitic phase. The fact that M_0^2 is positive at 358 K but negative at 360 K indicates the onset of the ferromagnetic transition of the austenitic phase near 359 K.

6.3 Summary of the Martensitic and Magnetic Phase Transitions

The previous two subsections presented the measurements and procedures used for the determination of the critical temperatures of the two overlapped phase transitions in the films. For clarity, these parameters are summarized in table 6.1. From table 6.1, it is possible to construct the sequence by which the structural and magnetic phase transitions unfold upon transforming from the paramagnetic austenite (PA) to the ferromagnetic martensite (FM) phase or *vice versa.* These two sequences given by:

$$FM \leftarrow M_f \leftarrow T_{50}^{cool} \leftarrow T_c^A \leftarrow M_s \leftarrow PA \quad \text{(cooling)} \tag{6.2}$$

$$FM \rightarrow A_f \rightarrow T_{50}^{heat} \rightarrow T_c^A \rightarrow A_f \rightarrow PA \quad \text{(heating)} \tag{6.3}$$

allow for an understanding of the temperature dependent magnetization shown in figure 6.4. With T_c^A and M_s being extremely close to one another, the cooling sequence through the phase transition begins with the nearly simultaneous emergence of the martensitic phase and the onset of the austenite's ferromagnetic transition. At this point, the magnetization of the film is dominated by the paramagnetic austenitic phase rather than the ferromagnetic martensitic phase and, thus, shows a small value. As the temperature is lowered, but while still remaining above T_{50}^{cool}, the austenitic phase continues to dominate due to its larger volume fraction. This dominance manifests itself as the steep rise in the magnetization, a consequence of increased ferromagnetic ordering in the austenitic phase. This tendency continues upon the further cooling of the sample down to 352 K, whereupon the ferromagnetic transition of the austenitic phase completes. Due to the completion of the austenite's ferromagnetic ordering and the increasing dominance of martensite volume fraction (T_{50}^{cool} = 355 K), the magnetic signal from the martensitic phase becomes quite pronounced as is evident from the drop in magnetization below 352 K. Such a drop in magnetization is attributed to the high magnetocrystalline anisotropy of the martensitic phase as compared to the austenitic phase (Tickle & James, 1999), which makes it significantly more difficult for the martensitic phase to be magnetized in the small magnetic field of μ_0H = 0.005 T used for this measurement. This rapid decrease of the magnetization continues until the volume fraction of the martensitic phase approaches 100%. A further reduction to the temperature, once all the phase transitions are complete, results in the monotonically increasing

Table 6.1: The critical temperatures associated with the structural and magnetic phase transitions for a $Ni_{51}Mn_{29}Ga_{20}$ (at.%) film.

M_s	M_f	A_s	A_f	T_c^A	T_c^M	T_{50}^{cool}	T_{50}^{heat}
361 K	307 K	312 K	370 K	359 K	>>361 K	355 K	358 K

magnetization expected for a pure ferromagnetic phase. When the film is heated from 2 K through the reverse transitions, the magnetization behavior is changed due to the higher volume fraction of the martensitic phase in the film, producing the hysteresis in the structural phase transition region. The lower magnetization peak at 352 K is a consequence of the smaller volume fraction of the austenitic phase at that temperature upon heating. For temperatures higher than T_{50}^{heat} (table 6.1), where there exists a significant volume fraction of the austenitic phase, the phase has lost much of its ferromagnetic ordering. The martensitic phase, on the other hand, remains ferromagnetic as long as it exists, due to its much higher Curie temperature. The occurrence of the crossover between the heating and cooling magnetization curves at 356 K (see inset to figure 6.1) is a manifestation of the low level of ferromagnetic ordering of the austenitic phase at temperatures above 356 K and the presence of the high volume fraction of the ferromagnetic martensitic phase in the film upon heating.

6.4 Magnetic Entropy Change

The overlapping magnetic and structural phase transitions provide the prerequisite condition for the occurrence of a large magnetocaloric effect. The effect, which depends upon both the magnitude of the applied magnetic field (H) and the temperature (T), gives rise to a change in magnetic entropy, which in turn provides a measure of the cooling capacity. A magnetic field induced entropy change, $\Delta S(T,H)_{\Delta H}$, produced under isobaric conditions can be estimated from the magnetization isotherms using the Maxwell relationship given by (Pecharsky & Gschneidner, 1999b):

$$\Delta S(T,H)_{\Delta H} = \int_0^H \left(\frac{\partial M(T,H)}{\partial T}\right)_H dH \tag{6.4}$$

For magnetization measurements made at discrete field and temperature intervals the above equation can be numerically solved using the approximate equation (McMichael *et al.*, 1993):

$$\Delta S(T,H)_{\Delta H} = \frac{1}{\Delta T}\left[\int_0^H M(T_2,H)_H dH - \int_0^H M(T_1,H)_H dH\right] \tag{6.5}$$

where the temperature interval (ΔT) and the average midpoint temperature (T_0) of the interval are given by:

$$\Delta T = T_2 - T_1, \quad T_0 = \frac{T_1 + T_2}{2} \tag{6.6}$$

From equation (6.5) it is apparent that the entropy change occurring over the (ΔT) temperature interval, which is assigned to the temperature T_0, is the area between the magnetization isotherms (figure 6.5) obtained at T_1 and T_2 divided by ΔT. Figure 6.7(a) shows a plot of the temperature dependent magnetic entropy change, calculated in this manner, as the sample is cooled through the phase transitions for magnetic field intervals ranging from 0.1 to 0.5 T. For each interval the negative of the magnetic entropy change shows a narrow peak with a maximum at 355 K and a peak width characterized by a full width at half maximum (FWHM) of approximately 6 K. Figure 6.7(b) shows the corresponding plot for the case where the sample is heated through the transition instead of being cooled. In this case, the negative of the magnetic entropy change shows a similar response except that the peak

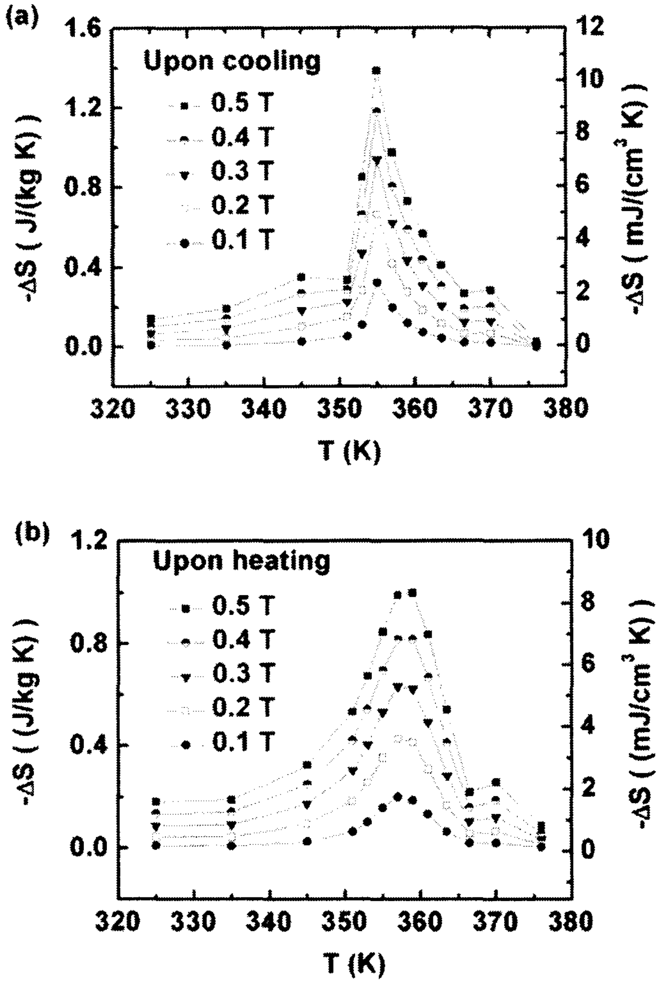

Figure 6.7: The negative magnetic entropy change as a function of temperature for a $Ni_{51}Mn_{29}Ga_{20}$ (at.%) film derived from magnetization data using magnetic field intervals ranging from 0.1 to 0.5 T upon (a) cooling and (b) heating through the phase transitions. Note that upon cooling the peaks in $-\Delta S$ are significantly larger and are shifted to a lower temperature. The dataset is also given in units of (mJ/(cm^3 K)) to facilitate comparisons with data obtained for other magnetic refrigerant materials reported in the literature.

position is shifted to 358 K and the height of the maximum is significantly reduced for each value of the magnetic field.

A second, more important, criterion for magnetocaloric materials is the refrigerant capacity (RC). The RC value is a direct measure of the heat transferred from the cooled volume to the hot reservoir in a refrigeration cycle (Wood & Potter, 1985). The RC values for the $Ni_{51}Mn_{29}Ga_{20}$ (at.%) thin films described here can be estimated using standard procedures. The two most commonly used procedures (Gorria *et al.*, 2008; Provenzano *et al.*, 2004) involve: (1) the numerical integration of the area under the ΔS versus T peak over the integration limits T_{c1} and T_{h1} (i.e. the temperatures associated with the peak's FWHM):

$$RC = \int_{T_{c1}}^{T_{h1}} \Delta S(T,H)dT \tag{6.7}$$

and (2) by the maximum area under the ΔS versus T peak which can be confined to a rectangular box extending from temperatures denoted as T_{c2} and T_{h2}. Figure 6.8 graphically depicts the areas used for both procedures for a film which has undergone either a cooling (figure 6.8(a)) or heating (figure 6.8(b)) sequence at a field of 0.5 T. From the data it is apparent that the refrigerant capacity depends upon the sequence used. During cooling, the first and second procedures yield RC values of 7.6 J/kg and 7.3 J/kg, respectively, while for the heating sequence the same procedures yield values of 9.1 J/kg and 7.1 J/kg. The values presented are not adjusted for hysteresis losses, as is customary for MCE materials such as $Gd_2Ge_2Si_2$ where losses can account for as much as 20% of the response (Provenzano *et al.*, 2004). Based on our magnetization data, the hysteresis losses do not exceed 3% for the $Ni_{51}Mn_{29}Ga_{20}$ (at.%) films. While there is a considerable spread in the RC values obtained, all of these values are somewhat smaller than the established values for typical MCE materials under similar magnetic fields (Gschneidner & Pecharsky, 2000). The lower values stem not from the amplitude of the ΔS vs. T peak, but from a smaller FWHM.

A closer examination of the magnetization data reveals that the magnetic entropy change

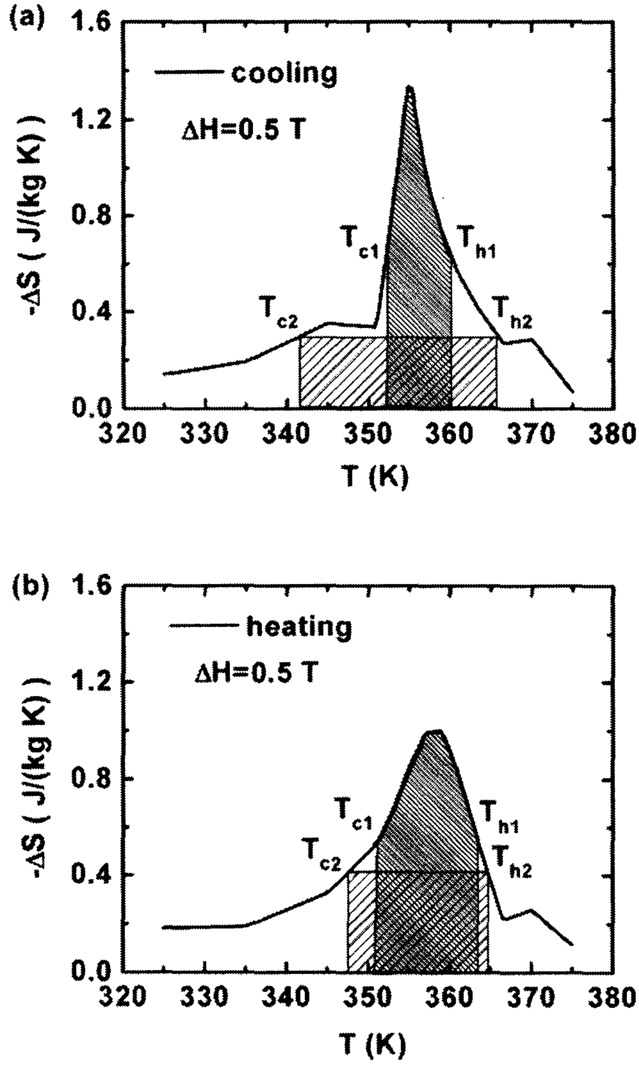

Figure 6.8: The entropy change as a function of temperature for the (a) cooling and (b) heating sequences where the densely and sparsely shaded areas under each curve provide a measure of the refrigerant capacity using the two methodologies defined in the text. The temperature limits for the two integration areas are labeled as T_c and T_h.

shows positive values at extremely low magnetic fields ($\mu_0H < 0.07$ T), as is shown in figure 6.9. As it can been seen from figure 6.9(a), the temperature dependent change in entropy displays a prominent peak originating from the MCE. The expanded view in figure

6.9(b), makes it apparent that -ΔS becomes negative (i.e. ΔS has a positive value) at lower temperatures for field values smaller than 0.07 T. The value of the positive ΔS is significantly smaller than the negative magnetic entropy change associated with the MCE effect (see figure 6.7). An examination of equation (6.5) reveals that a positive response of the magnetic entropy change originates from a smaller magnetization at lower temperatures. Because ΔT (= T_2 - T_1) is negative upon cooling (i.e. T_1 is greater than T_2) the sign of ΔS must be determined from the amplitudes of the magnetization at T_1 and T_2, showing positive values for $M(T_2) < M(T_1)$ and negative values for $M(T_2) > M(T_1)$. For the case of a standard MCE the latter is expected (figure 6.7) and, as a consequence, the negative values for -ΔS (i.e. $\Delta S > 0$) shown in figure 6.9(b) are not anticipated. This suggests that the positive entropy observed in figure 6.9(b) must be related to some other effects. A possible source of the positive entropy change could be the magnetic field induced reorientations (MIR) of the martensitic twin variants. Since the MIR effect was also observed at low magnetic fields ($\mu_0 H < 0.07$ T for T > 100 K) in the films studied, it is very likely that this effect causes some changes in the entropy due to the coupling between the magnetic and crystalline lattices (Planes *et al.*, 2009). Another possible reason for the positive entropy change could be the difference in the magnetic anisotropy energy between the austenitic and martensitic phases as such difference is more pronounced at low magnetic fields. For the convenience of discussion, we use MIR effect as an example to address the positive magnetic entropy change in figure 6.9(b).

To fully appreciate the negative values for $-\Delta$S associated with the MIR effect, a closer inspection of individual isotherms within the context of a MIR-induced phenomenon is required. In the MIR process there exists an activation magnetic field whereupon the magnetic energy is able to overcome the mechanical energy needed to initiate twin boundary

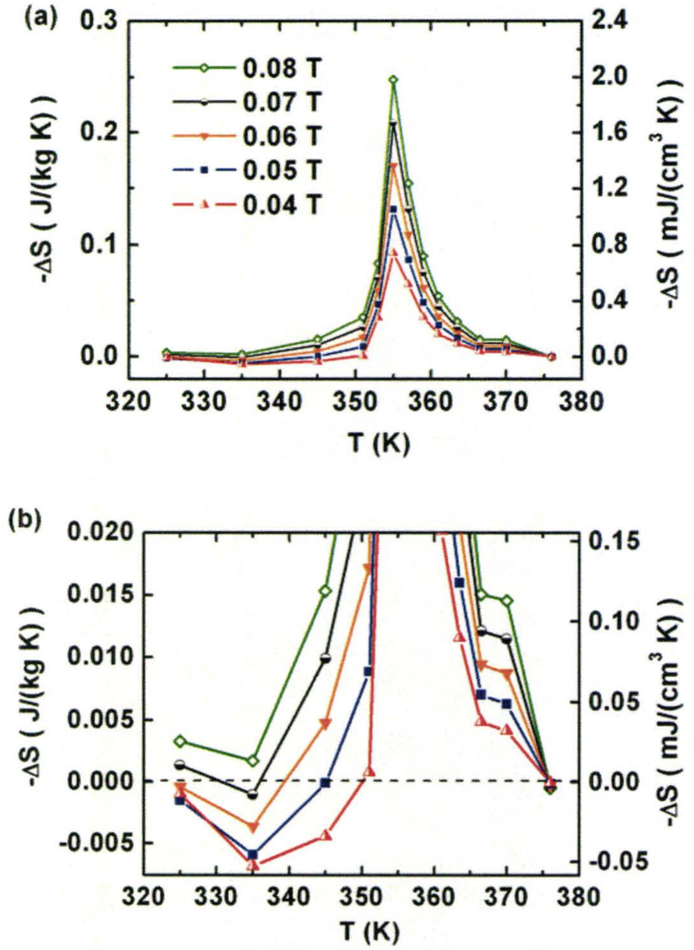

Figure 6.9: Temperature dependence of the magnetic entropy change for a $Ni_{51}Mn_{29}Ga_{20}$ (at.%) film using small magnetic field intervals ($\Delta H \leq 0.08T$). The prominent peak is associated with MCE. (b) Expanded view of the change in negative magnetic entropy ($-\Delta S$) which highlights the sign-change at low temperatures and fields (The dashed line denotes $-\Delta S = 0$). This increase in magnetic entropy (i.e. decrease in $-\Delta S$) likely originates from the magnetically induced reorientation of martensitic twin variants. The legend of (a) also applies to (b).

motion. It has been previously determined that the activation field spans a small range of magnetic fields, extending from an onset value of H_s to an endpoint value of H_f, whereby these values tend toward smaller fields as the temperature is increased (Straka *et al.*, 2006). As an illustration of this behavior, the $T_1 = 300$ K and $T_2 = 320$ K magnetization curves are shown in figure 6.10. The 330 K data exhibits a rapid increase in the slope of the magnetization due to MIR, which extends from an onset field of $\mu_0 H_s^{T_1}$ = 0.025 T to an endpoint field of $\mu_0 H_f^{T_1}$ = 0.04 T. The 320 K data, on the other hand, shows higher onset and endpoint fields which extend over the $\mu_0 H_s^{T_2}$ = 0.03 T to $\mu_0 H_f^{T_2}$ = 0.047 T range. The observed differences can be attributed to the increased twinning stress at lower temperatures (Straka *et al.*, 2006; O'Handley *et al.*, 2006; Peterson *et al.*, 2008). Therefore, for any given magnetic field below $\mu_0 H_f^{T_2}$ = 0.047 T, the MIR process is complete when the film is at T_1, but incomplete when the film is at T_2. Above this field value, the MIR process is complete for both temperatures as is characterized by the cross-over in the two magnetization isotherms in figure 6.10(a). The overall behavior can be summarized by the following inequalities:

$$\begin{cases} M(T_2,H) \approx M(T_1,H) & 0 \le H \le H_s^{T_1} \\ M(T_2,H) < M(T_1,H) & H_s^{T_1} < H < H_f^{T_2} \\ M(T_2,H) > M(T_1,H) & H > H_f^{T_2} \end{cases} \tag{6.8}$$

The first inequality is approximate since Ni-Mn-Ga alloys exhibit a strong magnetic crystalline anisotropy in the martensitic phase, which is a function of temperature and often leads to a lower initial magnetization at reduced temperatures. This effect, however, is negligible for the small temperature intervals (i.e. ΔT = -10 K) used here, as is evident from figure 6.10(a), which shows nearly overlapping magnetization curves for fields below $H_s^{T_1}$. Nevertheless, a conclusive result can be deduced from equation (6.8) which is given by:

$$\begin{cases} \int_0^H M(T_2,H)_H dH - \int_0^H M(T_1,H)_H dH \approx 0 & 0 \le H \le H_s^{T_1} \\ \int_0^H M(T_2,H)_H dH - \int_0^H M(T_1,H)_H dH < 0 & H_s^{T_1} < H < H_f^{T_2} \\ \int_{H_f^{T_2}}^H M(T_2,H)_H dH - \int_{H_f^{T_2}}^H M(T_1,H)_H dH > 0 & H > H_f^{T_2} \end{cases} \tag{6.9}$$

These expressions in combination with equation (6.5) can be used to obtain the relationships:

$$\begin{cases} \Delta S(\frac{T_1+T_2}{2},H) = \frac{1}{\Delta T}[\int_0^H M(T_2,H)_H dH - \int_0^H M(T_1,H)_H dH] \approx 0 & 0 \leq H \leq H_s^{T_1} \\ \Delta S(\frac{T_1+T_2}{2},H) = \frac{1}{\Delta T}[\int_0^H M(T_2,H)_H dH - \int_0^H M(T_1,H)_H dH] > 0 & H_s^{T_1} < H < H_f^{T_2} \\ \Delta S(\frac{T_1+T_2}{2},H) = \frac{1}{\Delta T}[\int_{H_f^{T_2}}^H M(T_2,H)_H dH - \int_{H_f^{T_2}}^H M(T_1,H)_H dH] < 0 & H > H_f^{T_2} \end{cases} \tag{6.10}$$

where for the data shown in figure 6.10,

$$\frac{T_1+T_2}{2} = 325 \text{ K}, \quad \Delta T = 320 - 330 = -10 \text{ K} \tag{6.11}$$

The above analysis accounts for the positive entropy change (i.e. $-\Delta S < 0$) observed at 325 K in figure 6.9(b) for $\Delta H = 0.04$ T ($H < H_f^{T_2}$ where $H_f^{T_2} = 0.047$ T). It can also be predicted from the data that the maximum positive entropy change will occur for ΔH=0.047 T, since this value yields the maximum negative integration area (denoted as A1 in figure 6.10). For $\Delta H > 0.047$ T, where $M(T_2,H) > M(T_1,H)$, the sign of the entropy change could be either positive or negative, since it is determined from the additive contributions of the negative integration area A1 obtained for $H < H_f^{T_2}$ and positive integration areas obtained for $H > H_f^{T_2}$ (i.e. the areas A2, A3, and A4 corresponding to 0.05 T, 0.06 T, and 0.07 T, respectively). The sign for any given field interval will depend on whether the accumulated positive areas exceed the negative ones. In simple terms the sign-change, for a given pair of isotherms such as those shown in figure 6.10, occurs at a field value where the area between the isotherms below the cross-over at $H_f^{T_2}$ (i.e. A1) is equal to area after the cross-over. As fields are increased further the area below the cross-over will progressively be dominated by the much larger integration area above the cross-over. For example, when considering the total area (A1+A2+A3+A4), the sign of the integration area will switch from negative to positive for fields exceeding 0.06 T, since the total positive area (A2+A3+A4) is greater than the negative area A1.

It should be noted that the MIR phenomenon is associated with a detwinning process, which occurs only for the martensitic phase. That is, the effect of the MIR on the entropy change can only be observed for temperatures where a significant percentage of the martensitic phase exists which, for the thin films under study, corresponds to temperatures below 340 K. Thus, the negative $-\Delta S$ observed above 340 K for fields of 0.04 T and 0.05 T (figure 6.9(b)) cannot be associated with the MIR process. A closer examination of the entropy data reveals that this non-MIR response occurs only for magnetic fields smaller than 0.05 T, where the austenitic phase has a relatively large magnetization compared to the martensitic phase due to its smaller magnetic anisotropy energy which makes it more amenable to magnetization at low fields. Since the amount of austenitic phase decreases with temperature, the lower values for the magnetization will ensue. The resulting process will, then, very likely fall under the inequality $M(T_2,H) < M(T_1,H)$ and be characterized by a positive entropy change (negative $-\Delta S$). This behavior no longer exists for temperatures lower than 340 K due to the extremely low levels of the austenitic phase present (see figure 6.2).

On a final note, it should be recognized that the above discussion represents a phenomenological interpretation of the magnetic entropy change. It does not reveal the structural source of $M(T_2,H) < M(T_1,H)$, which is directly responsible for the positive entropy change, as indicated by equation (6.5). There could very well be some unknown effects, other than the MIR effect and/or magnetic anisotropy difference between the two structural

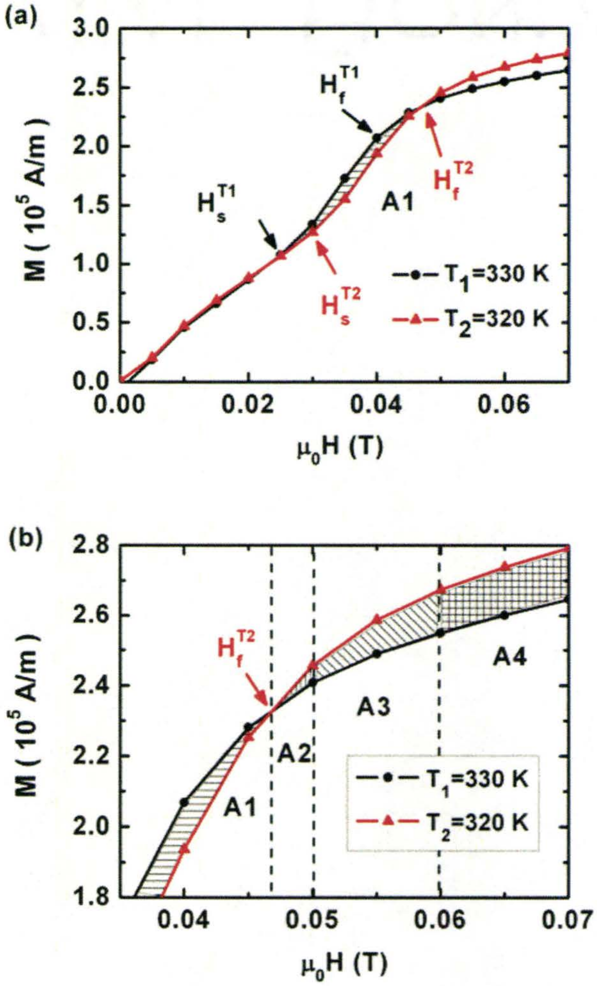

Figure 6.10: (a) Magnetization isotherms measured at $T_1 = 300$ K (black) and $T_2 = 320$ K (red) for low fields where the magnetic induced reorientation of twin variants is observed. Both isotherms show a rapid increase in the slope due to this reorientation with onset and endpoint activation fields labeled at H_s and H_f, respectively. (b) Expanded view of the magnetization curves in the magnetic field range of 0.03 $\sim$ 0.07 T where the integration areas A1, A2, A3, and A4 between the two isotherms correspond to the entropy change under various fields. Of significance is the fact that A1 will give rise to an integration area of opposite sign to that of areas A2, A3 and A4 due to the crossover at $H_f^{T_2}$.

phases, which may contribute to the positive entropy change. To unambiguously interpret this phenomenon, further and more comprehensive studies are required and these are beyond the scope of the present work.

6.5 Discussion

The results presented show a large MCE in $Ni_{51}Mn_{29}Ga_{20}$ (at.%) films which is characterized by a maximum magnetic entropy change of $|\Delta S_{\mathrm{max}}|$ = -1.4 J/kg-K at 355 K for a magnetic field interval of 0.5 T. While it is often difficult to directly compare this value to other results in the literature due to the widely varying field intervals used, it is possible to make such comparisons if appropriate estimates are made. Using the conservative assumption that the magnetization is saturated at 0.5 T one obtains a maximum magnetic entropy change ($|\Delta S_{\mathrm{max}}|$) of 2.4, 4.5, 10.8, 12.2 J/kg-K for fields of 1, 2, 5, and 6 T respectively. While the 5 T value is smaller than what has been observed in single crystals of Ni-Mn-Ga (Pasquale *et al.*, 2005; Zhou *et al.*, 2005b), the 6 T value of 12.2 J/kg-K is 40% larger than the only reported value of 8.5 J/kg-K for Ni-Mn-Ga films observed at 346 K (Recarte *et al.*, 2009). Also of significance is that the observed magnetic entropy change of 4.5 J/kg-K for a 2 T magnetic field change is two times larger than the 2 J/kg-K value reported for Ni-Mn-Ga particles (Tang *et al.*, 2005). It is noteworthy that the 1 T value of 2.4 J/kg-K is quite comparable to the established values for low field magnetic refrigerant materials (Sarkar *et al.*, 2008). Thus, any micro-length-scale refrigerant devices produced from such films could be operated at significantly lower fields. Contradistinctive to the large entropy change exhibited by these films is the somewhat low refrigerant capacity which results from the narrow nature of the magnetic entropy peak which is due to the small temperature interval associated with the overlapped structural and magnetic phase transitions.

The temperature dependent magnetic and transport properties of the $Ni_{51}Mn_{29}Ga_{20}$ (at.%) films unequivocally show that the MCE is maximized where there exists significant overlap between the structural and magnetic phase transformations. The effect of the overlap is most evident in the fact that the hysteresis in the structural transition manifests itself in the ferromagnetic phase transition due to the dissimilar magnetic properties of the structural phases. Distinctive to the behavior of the film is a temperature hysteresis in the entropy peaks between the heating and cooling sequences. A close examination of the peak positions indicates that the peaks occur at the temperature T_{50}, where the austenitic and martensitic phases show equal volume fractions, a relationship followed for both the heating and cooling sequences. Since the T_{50} temperature is different for both sequences (i.e. T_{50}^{cool} = 355 K and T_{50}^{heat} = 358 K), the difference in peak position is related to the temperature hysteresis in the forward and reverse martensitic phase transitions. It is not surprising that the vertex point appears at the T_{50} temperature, since this is the temperature where the differences in the overall magnetization contributed from each phase are largest. While this finding appears in contradiction to the single crystal results which exhibit an entropy peak at the martensitic start temperature (i.e. the M_s temperature) (Zhou *et al.*, 2005b), it should be recognized that data presented here describe a somewhat more complex situation. The difference originates from the fact that the MCE in single crystals occurs when the sample transforms directly from the paramagnetic austenite to the ferromagnetic martensite state where the ferromagnetic ordering in the austenite phase does not participate in the MCE effect. This, however, is not the case for the films described here, as the ferromagnetic transition of the austenitic phase occurs in the temperature range associated with the MCE and has been shown to play an important role.

Another unique feature associated with the magnetic entropy change versus temperature plots (figure 6.7) is the fact that the peak height also depends upon whether the film has undergone a heating or cooling sequence. In order to understand this variation, one must bear in mind that the Curie temperature for the martensitic phase ($T_c^M >> 361$ K) is well above the $-\Delta S$ peak positions for both the heating and cooling sequences. Thus, it is expected that the ferromagnetic ordering is firmly established for the martensitic phase for both sequences at the peak position. Thus, the response from this phase at the peak positions, where 50% of the film is martensite, should be identical for both sequences. It should be recognized that this is not the case for the austenitic phase since its ferromagnetic transition, which starts at 359 K (T_c^A = 359 K) and ends at 352 K (figure 6.4), overlaps with the temperature ranges associated with the magnetic entropy peak. This overlap, however, is to a lesser extent for heating than it is for the cooling sequence. For the heating sequence, which exhibits a magnetic entropy peak at 358 K, there exists only a small amount of austenite that has transformed from the paramagnetic to the ferromagnetic phase. The cooling sequence, on the other hand, has significantly more austenite that has gone through its ferromagnetic transition due to the fact that the end of the transition, which occurs at 352 K, is closer to the cooling sequence's entropy maximum at 355 K. It is this higher degree of ferromagnetism in austenite that is the likely source of the enhanced peak height for the cooling sequence. The significant asymmetry associated with the $-\Delta S$ peak during the cooling sequence is consistent with a rapid development of ferromagnetic ordering within the austenite component.

The above analysis reveals that the enhancement to the MCE from the overlapping structural and magnetic phase transition is far more intricate than a simple addition of the contributions from each transition. The martensitic transformation contributes through an overall difference in the magnetization between the austenitic and martensitic phase, while the ferromagnetic transition contributes through the ordering in the magnetic subsystem. Improving the latter weakens the former since the overall magnetization difference between the two structural phases is reduced as the total magnetization associated with the austenitic phase increases at the more complete ferromagnetic ordering. A reduction of the ferromagnetic ordering in the austenitic phase, on the other hand, also deteriorates the MCE as is corroborated by the 30% reduction to magnetic entropy peak height observed for the heating process (figure 6.7). It should also be recognized that, while the first-order structural phase transition augmented the MCE observed here, this is not always the case. A weakened MCE can occur if the martensitic phase shows a magnetization which is smaller than that of the austenitic phase. In this scenario, the austenite to martensite transition gives rise to a positive magnetic entropy change (Sharma *et al.*, 2007), which decreases the strength of the MCE governed by the magnetic phase transition when the two phase transitions coexist.

Chapter 7

Ni-Mn-Ga Micro-Bridges

In Chapter 5, the rearrangement of the martensitic variants under an external magnetic field, i.e. MIR effect, has been discussed. This effect is the prerequisite for the existence of the ferromagnetic shape memory effect in Ni-Mn-Ga alloys. It should be noted, however, that the Ni-Mn-Ga system can exhibit shape memory behaviour not only in a magnetic field, but also under external stresses, as observed in conventional shape memory materials. For stress induced SME, detwinning occurs when twin variants are subjected to an external load. The variants which give rise to the largest transformation strain are usually favoured by the stress and grow at the expense of the other variants. This phenomenon which has been intensively investigated in the conventional thermally driven shape memory alloys, such as Ni-Ti and Cu-Zn-Al, is seldom studied for Ni-Mn-Ga system since most of the attention has been paid to the MIR effect due to the ferromagnetic nature of the Ni-Mn-Ga alloys. Recently, the stress-field-induced selection of variants in Ni-Mn-Ga alloys was explored by Wang et al. (Wang *et al.*, 2007). Their experimental results indicate that the spatial distribution of variants in the structure can be dramatically disturbed when the material is subjected to a small uniaxial stress. This finding provides the impetus for investigating the microstructural evolution of the twin variants under stress in the Ni-Mn-Ga system and for developing a mechanical "training" mechanism.

Experimental studies of the mechanical properties of thin films are challenging. The generally applied mechanical testing methods, such as tensile testing and hardness indentation, are not applicable to thin films, although they work quite well on bulk materials. For thin films, mechanical measurements require special tools and equipment. Loading has to be carefully applied and strains are typically measured by optical methods. Important is the fact that films are affixed to rigid substrates, which makes strain measurement more difficult. Therefore, developing a simple, yet efficient, method to test the mechanical behaviour of the Ni-Mn-Ga films is essential. In this chapter, we will demonstrate an approach for detecting the mechanically induced microstructure evolution in the Ni-Mn-Ga films by utilizing the substrate imposed stresses. The method involves the patterning of the films into free-standing bridges where the arm of the bridge is released from the substrate. Some striking detwinning phenomena have been observed in the detached regions of these bridges.

7.1 Ni-Mn-Ga Films Deposited on (100) MgO

To effectively release the Ni-Mn-Ga films from the underlying substrates, proper etching solutions are required. An ideal etching solution should be able to preferentially etch the substrate while not attacking the film. Thus, the film is released from the substrate without being damaged. A number of acids, such as HCl, H_2SO_4, $C_2H_4O_2$, and HNO_3, have been tested on the two substrates which gave rise to the highest quality Ni-Mn-Ga films: (100) YSZ and (100) MgO. It has been found that only the hydrochloric acid (HCl) satisfied the requirements of a preferential etch. It can attack the MgO substrates effectively while leaving the Ni-Mn-Ga films intact. This preferential-etch-substrate combination was then used to fabricate the Ni-Mn-Ga free-standing bridges.

7.1.1 Crystallography

The Ni-Mn-Ga films grown on the MgO substrates have a composition of $Ni_{52}Mn_{24}Ga_{24}$ (at.%). The three-dimensional X-ray diffractometry (XRD^3) measurements indicate that the films have an orthorhombic crystal structure at room temperature with lattice parameters of a=6.2 Å, b=5.8 Å, c=5.4 Å.

Figure 7.1 shows the {400} pole figures extracted from the XRD^3 dataset in which the {400} poles can be found at a radial angle close to 90° for all three pole figures. Those pole patterns indicate a <100> oriented film where there exist three grain growth orientations: [100], [010], and [001]. For those grains growing along the [100] or [001] orientations, their (100) or (001) plane is not quite parallel to the surface of the substrate but instead tilts from it by a small angle, as is indicated by the fact that the peaks for both the (400) and (004) pole figures split into four rather than showing a single peak at the center of the pole figure. For the (400) pole figure the tilt angle is 4° while for (004) pole figure the tilt is 3°. The fact that the (400) and (004) pole pattern shows fourfold symmetry indicates that the films are comprised of four sets of [100] oriented grains and four sets of [001] oriented grains. Any two of the four [100] oriented martensite crystals have the possibility of forming twins when they are adjacent to one another. Similar argument can also be applied to the martensite crystals oriented along [001] direction. No twinning relationship has been observed between grains growing along the [100] and [001] orientations. Such a polytwinned structure is not unexpected since twinning is a common means by which martensitic grains accommodate the strains associated with the diffusionless martensitic phase transformation. Of note is the fact that the (040) pole figure, unlike the (400) and (004) pole figure, shows no peak-splitting. Instead, it demonstrates a single pole at a 90° radial angle. Such a pole pattern indicates that some of the martensite grains grow along the [010] direction and the (010) plane of these grains is parallel to the substrate surface. These observations are consistent with what has been reported in literature (Thomas *et al.*, 2008a,b; Mahnke *et al.*, 2008). The powder X-ray spectra for these films show a broad peak at the 2θ angle of approximate 64°, which is consistent with the (040) reflection of the martensitic phase. The (400) and (004) orientations are not observed since the $\theta - 2\theta$ XRD is only sensitive to periodicities normal to the surface of the substrate.

7.1.2 Surface Morphology and Microstructure

A weave-like surface morphology was observed for the $Ni_{52}Mn_{24}Ga_{24}$ (at.%) films. The entire pattern contains numerous wavy lines approximately 30 to 50 nm in width and typically extending for 5 to 20 μm. These wavy lines propagate along the [011] or $[0\bar{1}1]$ direction of the (100) oriented substrate, as shown in figure 7.2. The regions covered by "parallel" wavy lines are divided into rectangular blocks where the border region between the blocks (denoted by the white arrows in figure 7.2) is typically 100 nm wide and quite

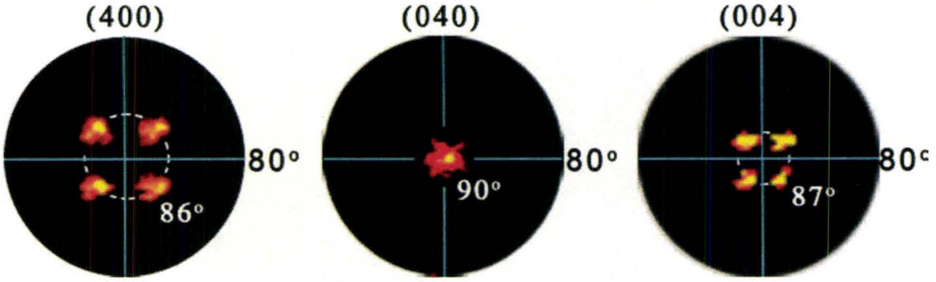

Figure 7.1: Room temperature (400), (040), and (004) pole figures for a $Ni_{52}Mn_{24}Ga_{24}$ (at.%) martensite film where only the central portion of the pole figure (between 80° and 90°) is shown. Both the (400) and (004) pole figures show a fourfold peak-splitting near the 90° radial angle, indicating a polytwinned microstructure for the martensitic phase. The growth direction of these twin-related martensitic variants is not parallel to the normal of the substrate, but instead tilts away from it by a small angle. The (040) pole figure only shows a single peak at the center of the pole figure, indicating the existence of the [010] oriented martensitic variants whose (010) plane is parallel to the substrate surface.

smooth.

In order to obtain a better understanding of the weave-like surface morphology of the $Ni_{52}Mn_{24}Ga_{24}$ (at.%) films, the cross-section of the films were probed with TEM. Figure 7.3(a) shows a TEM bright field image of the films' cross-section. It displays two types of martensite plates which are denoted by white arrows. The Type I martensite plates, labeled as "A" and "B" in figure 7.3(a), tilt approximately 43° from the substrate surface. The Type II martensite plates, labeled "C", show weak contrast since they are rotated by an in-plane angle of 90° relative to the Type I plates. The boundary between any two sets of Type I plates could be narrow or broad, depending on where these plates meet. When the two sets of Type I plates intersect at the surface of the film, they demonstrate a narrow boundary (i.e. the boundary "D" in figure 7.3). Conversely, a wide boundary is exhibited if the two sets of Type I plates meet at the substrate-film interface (e.g. the boundary "E" in figure 7.3(a)). The Type I and Type II plates encounter each other at "F". By comparing the

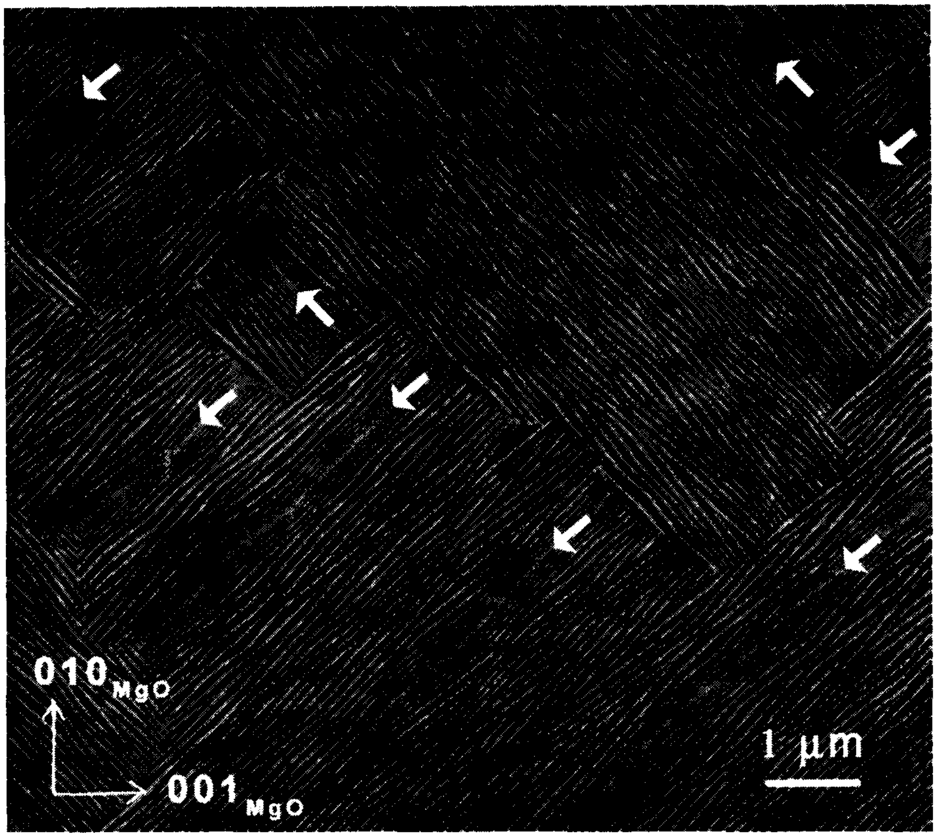

Figure 7.2: SEM image of a $Ni_{52}Mn_{24}Ga_{24}$ (at.%) film grown on (100) MgO showing a weave-like surface morphology. The film surface is comprised of a large number of wavy lines propagating along the [011] or [0$\bar{1}$1] directions of the [100] oriented MgO substrate. The regions covered by "parallel" wavy lines are divided into rectangular blocks where the border regions between the blocks are marked by white arrows. Miller indices at the lower left corner show the orientation of the MgO substrate relative to that of the film.

TEM image with the SEM observation, the surface morphology shown in figure 7.2 can be explained. It appears that the wavy lines in the SEM image originate from the surface relief of the martensite plates. The two groups of perpendicular surface reliefs are associated with the two types of martensite plates. Surface relief from plates belonging to the same type occurs as "parallel" lines while those from plates belonging to a different type are "perpendicular" to one another. The boundaries between the like plates appear as sharp edges (i.e. boundary "D") or wide bands (i.e. boundary "E"), as pointed in figure 7.3(b).

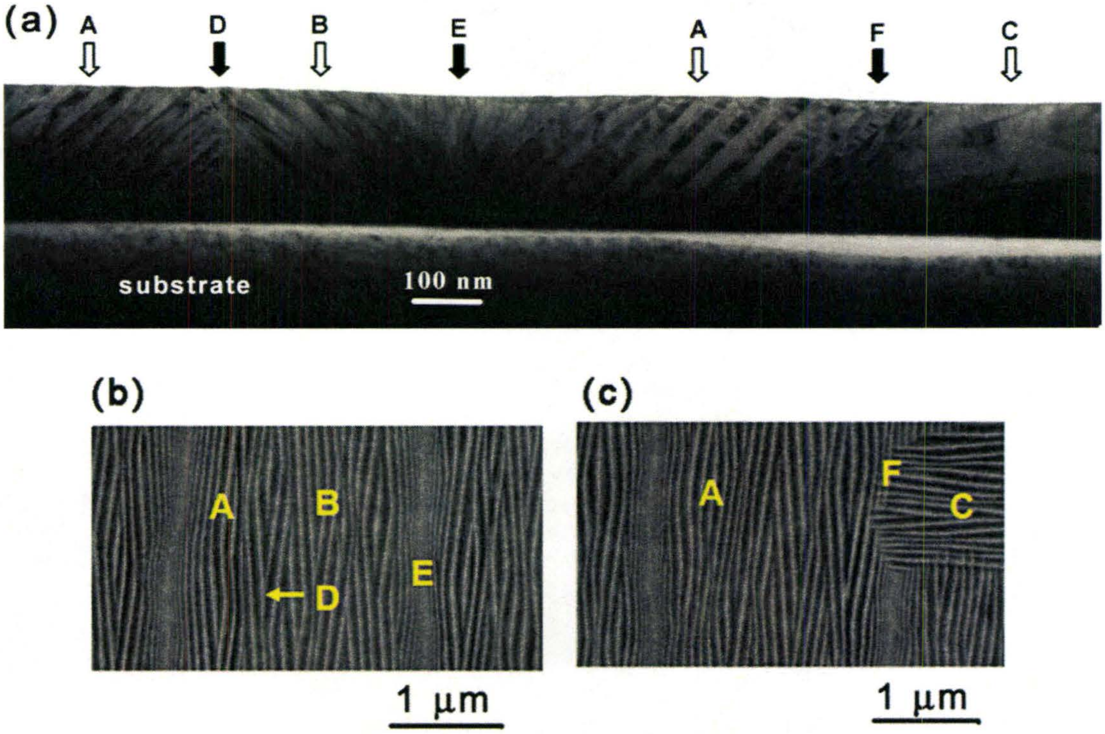

Figure 7.3: The correspondence between the (a) TEM and (b) SEM observations for a $Ni_{52}Mn_{24}Ga_{24}$ (at.%) film. The TEM image displays two types of martensite plates, as denoted by the white arrows in figure 7.3(a). The Type I plates (i.e. "A" and "B") tilt away from the substrate surface at an angle of approximately 43°. The Type II plates (i.e. "C") have a similar geometry but where they are rotated in-plane by 90°. The wavy lines in the SEM image are associated with the surface relief of the martensitic plates. Surface relief from plates belonging to the same type occur as "parallel" lines while those from a different type are "perpendicular" to one another. The boundaries between the like plates appear as sharp edges (i.e. boundary "D") or a wide band (i.e. boundary "E"). The Type I and Type II plates meet at "F".

When plates of a different type encounter one another, the surface relief of one type of plate either stops at or penetrates into the surface relief of the other.

7.1.3 Martensitic Phase Transformation

The martensitic phase transformation in the $Ni_{52}Mn_{24}Ga_{24}$ (at.%) films is characterized through temperature dependent DC resistivity measurements. The resistivity versus temperature curve, $\rho(T)$, is shown in figure 7.4. The martensitic transformation occurs in a wide temperature range between 350 and 445 K, where the four characteristic temperatures are determined as M_s = 430 K, M_f = 350 K, A_s = 351 K, and A_f = 445 K. Compared with the data reported in the literature, it is found that the M_s temperature is approximately 160 K higher than that of the bulk Ni-Mn-Ga sample having the same valence electron concentration (Vasil'ev *et al.*, 1999; Jin *et al.*, 2002). Since the compositional gradient in the film is not significant (see section 3.2.3), the wide transition temperature range together with the increased M_s temperature indicates a high internal stress level in the film accompanying the phase transformation. Such behavior has been attributed to the constraints arising from the underlying substrate (Thomas *et al.*, 2008b).

7.2 Ni-Mn-Ga Micro-Bridges

Ni-Mn-Ga micro-bridges were prepared using photolithographic techniques followed by wet chemical etching. Details of the fabrication process are presented in Section 3.3.

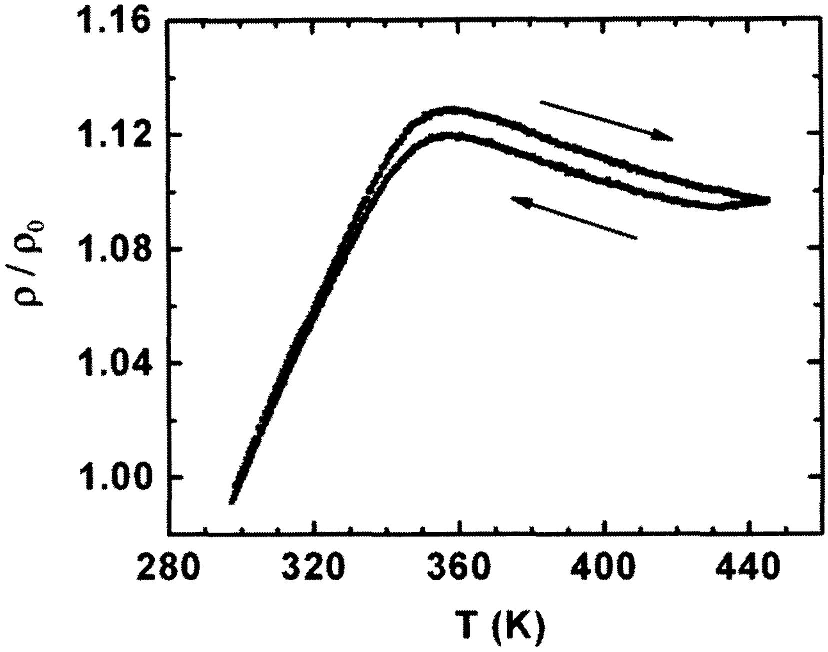

Figure 7.4: Temperature dependent DC resistivity for a $Ni_{52}Mn_{24}Ga_{24}$ (at.%) film measured using the van der Pauw technique. The characteristics show a reversible martensitic transformation in the temperature range of 350 to 445 K. All values were normalized to the resistivity (ρ_0) of the film at 300 K.

7.2.1 Ni-Mn-Ga Bridge Pattern

The produced Ni-Mn-Ga micro-bridges have a typical length, width, and thickness of 50 μm, 20 μm, and 0.2 μm, respectively. Figure 7.5 shows a bridge pattern containing three individual micro-bridges. The bridges were released from the substrate using wet chemical etching. On each released bridge, a plaid pattern is observed (figure 7.6(a)), a feature indicative of a free bridge arm. The contrast becomes more evident when the sample is tilted by a large angle relative to the electron beam. Figure 7.6(b) shows an SEM image of a bridge being tilted by 70° (i.e. the angle between the surface normal of the film and the electron beam is 70°). A strong contrast can be viewed between the released and affixed

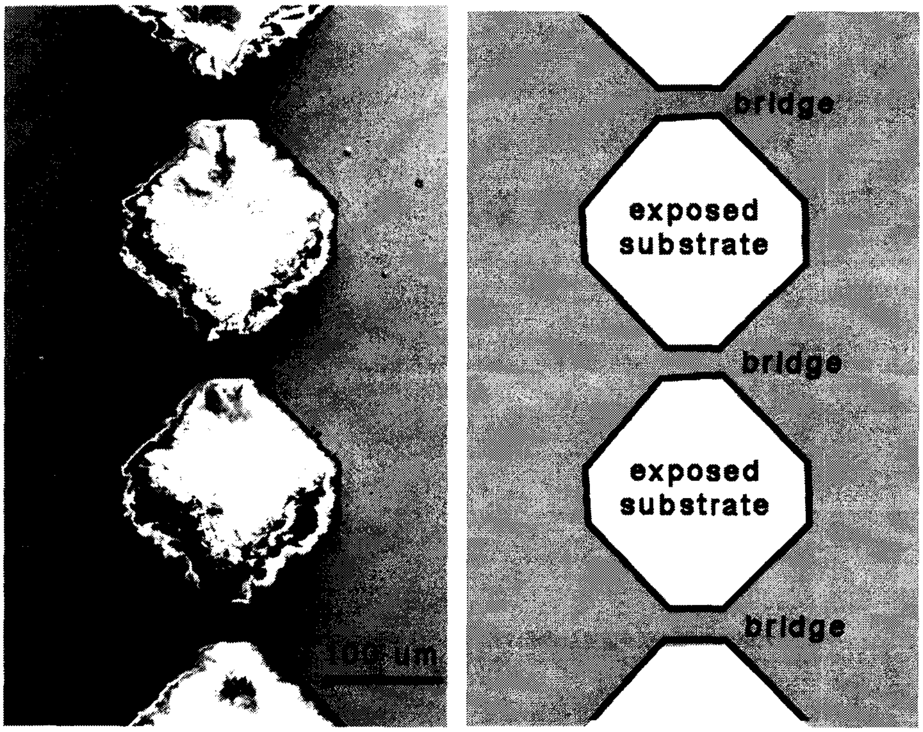

Figure 7.5: SEM image of a bridge pattern made from $Ni_{52}Mn_{24}Ga_{24}$ (at.%) films (Left) and the corresponding schematic depiction (right). The typical dimension of a single bridge is $50\times20\times0.2$ μm^3.

region, which reveals that all the film areas contiguous to the exposed substrate are free of substrate constraints. To provide readers a stronger visual impact, the SEM images for a non-released bridge are also displayed in figure 7.6.

7.2.2 Detwinning on the Detached Bridge Arm

Figure 7.7 displays an expanded view of the border between the detached and affixed region at high magnification. It indicates that one orientation of the surface relief (i.e. the

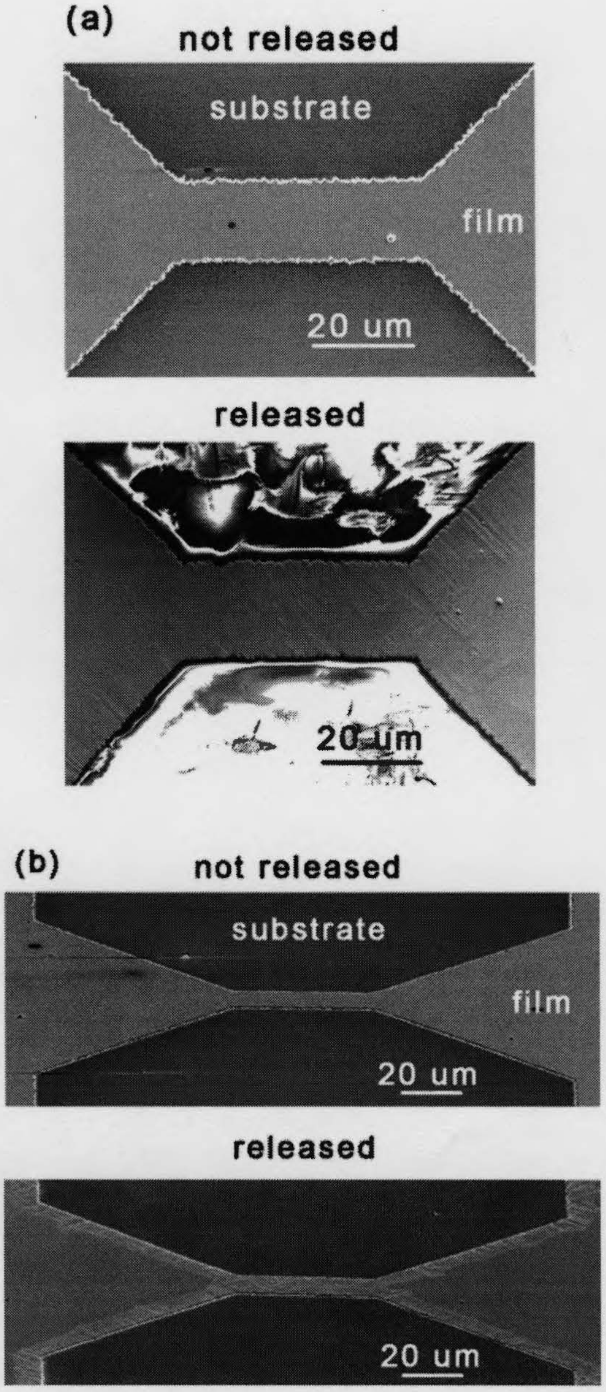

Figure 7.6: SEM image of an attached (top) and a released (bottom) bridge viewed at high magnification from the (a) top and (b) a 70° tilt angle. A plaid pattern is observed on the detached bridge.

surface relief that propagates along Orientation 2 in figure 7.7b) has disappeared in the detached areas. The retained surface relief is perpendicular to the edge of the bridge end, e.g. the surface relief which propagates along Orientation 1 is perpendicular to the bridge end denoted "A" while the surface relief along Orientation 2 is perpendicular to the bridge end denoted "B". Such modifications in the microstructure are likely caused by changes to the stress-field within the released areas. The situation at the detached bridge arm is more complex, as is evident by the plaid pattern on the arm which is comprised of surface relief propagating along both directions. A clear understanding of this detwinning behavior requires further experimental investigations.

7.3 Future Work

Additional features were found in figure 7.7. There exists some difference between the surface relief in the suspended regions and the affixed areas, even though the two are along the same orientation (i.e. surface relief along Orientation 1). The surface relief in the detached area is straight while those formed during the deposition process are wavy. No obvious boundaries, such as those denoted "D" and "E" on figure 7.3, can be found in the detached areas. Such phenomena are attributed to the reorientation of the martensitic variants under stresses. If figure 7.3(a) is used to explain the situation, then Orientation 1 and Orientation 2 in figure 7.7 is assigned to the martensite plates Type I and Type II, respectively. The disappearance of the surface relief along Orientation 2 indicates that the Type II martensite plates are consumed by the Type I plates. The absence of the boundary type "D" and "E" in the detached bridge end indicates that only one of the two sets of Type

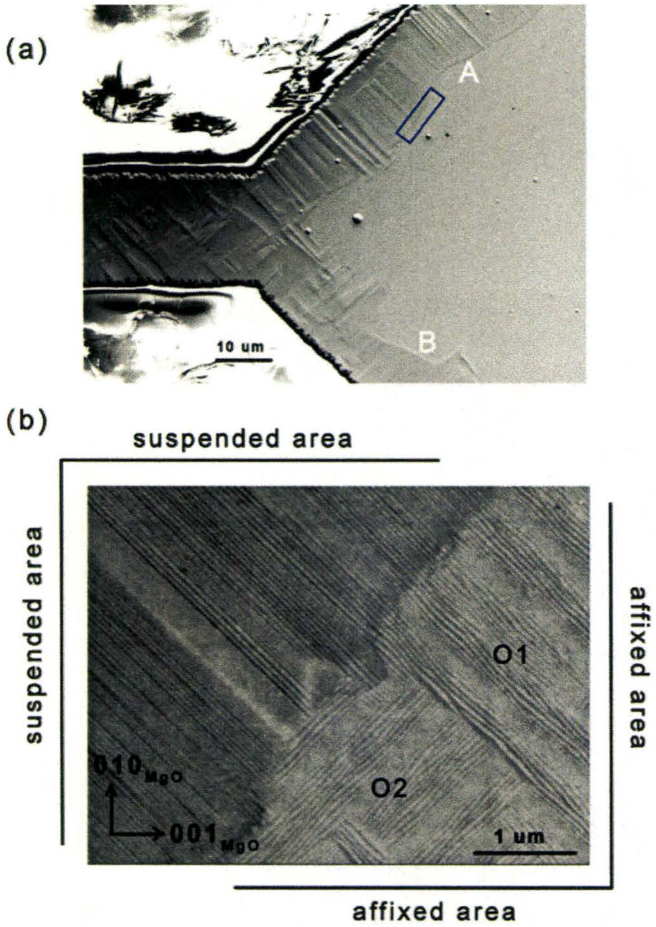

Figure 7.7: SEM image of a single bridge showing (a) a contrast change in the suspended region and (b) the disappearance of surface reliefs which propagate along orientation 2 in the released area. The image in (b) was taken at high magnification from the region in (a) denoted by the rectangle. The retained surface reliefs for the two opposite ends (e.g. end A and B) are oriented differently. Miller indices at the lower left corner of (b) show the orientation of the MgO substrate relative to that of the surface relief for the film. "O1" and "O2" are the abbreviations of the terms "Orientation 1" and "Orientation 2".

I plates remains (e.g. either plates "A" or plates "B" but not both). To verify the above hypothesis, several questions have to be addressed:

1. Do the martensite plates in the suspended areas belong to the same type as the martensite plates which provide the surface relief propagating along Orientation 1 in

the attached regions?

2. Do martensite plates in the detached regions belong to one of the two sets of Type I plates? What do they look like?

3. What happens at the interface between the detached and attached regions?

To answer these questions, some further experimental work is required. Useful experimental tools are electron backscattered diffraction (EBSD) and TEM with atomic resolution. The former should have the ability to address the first question. If the EBSD measurements taken in the detached and affixed regions show the same pattern, we would conclude that the martensite plates in these two areas have the same structure. The second and the third question could be studied using TEM and high resolution TEM as they are ideal for microstructure and interface observation. The focused ion beam (FIB) technique should be employed to prepare the TEM specimen because the general TEM sample preparation methods are not applicable to such delicate micro-bridges which are only 20 μm in width.

Other attractive research aspects for these micro-bridges include *in-situ* observations on the microstructure evolution in a series of physical processes, such as thermally induced shape memory effect and the magnetically induced martensitic variant selection. Without substrate constraint, a free standing film should be able to exhibit more discernable macroscopic shape/size changes and is, thus, ideal for demonstrating the shape memory effect.

Chapter 8

Conclusions

Ferromagnetic Ni-Mn-Ga shape memory thin films are promising candidates for actuation-based applications and magnetic refrigeration applications at the microscopic length scales. To understand the properties of these materials we have synthesized thin films of Ni-Mn-Ga on different substrates and have studied their thermomagnetic and magnetomechanical properties. The films grown on (100) YSZ were used to understand the phase transformation, MIR effect, and the magnetocaloric effect. The films deposited on (100) MgO were fabricated into free-standing micro-bridges, followed by an examination of the microstructure evolution of the martensitic twin variants due to the altered stress field.

A new fabrication pathway for film growth has been developed which allows for synthesis of Ni-Mn-Ga films in a previously unexplored high temperature deposition regime. The temperatures employed allowed the development of the desired micrometer-size highly twinned martensitic grain structure. The loss of the volatile elements, such as manganese and gallium, at high temperatures was compensated for through enrichments to the target material. The as-grown $Ni_{51}Mn_{29}Ga_{20}$ (at.%) films show a high degree of [101] texture and the desired shape memory alloy properties with a well-defined reversible martensitic transformation centered around 340 K, a room temperature martensitic phase with an in-plane saturation magnetization of 4.2×10^5 A/m, and a coercive field as small as $\mu_0H = 0.005$ T. A room-temperature magnetically induced reorientation of the martensite variants (MIR) has been observed at a low magnetic field of $\mu_0H = 0.04$ T.

The MIR effect displayed by the films shows some distinctive features. It is reversible, self-activated, and is characterized by a small increase in the magnetization, which is quite different from what has been observed in single crystals. These features are attributed to a unique magnetic domain structure comprised of MIR-active and MIR-inactive grains. The degree of grain-activity during field-induced microstructure reorganization depends on the relative orientations of the externally applied magnetic field and the easy axis of the magnetization of the variants. The MIR-active and MIR-inactive grains occupy approximately the same volume fraction (i.e. ~50%) of the film's microstructure. The MIR-active grains are responsible for the detwinning while the MIR-inactive grains facilitate the reversibility in the MIR process. The MIR-inactive grains block the displacive movement of the atoms in the MIR-active variants during their reorientation and exert stress on the film. The stress acts as restoring force and shears the atoms in the MIR-active grains back to their initial positions when the magnetic field is removed.

The substrate plays a crucial role in determining the initial crystallographic texture of the film. The texture is inherited by the magnetic microstructure which accordingly contains MIR-active and MIR-inactive grains. The existence of the in-plane grain orientations offset by 90° in the martensitic phase is the consequence of the adaptation of the [110] oriented Ni-Mn-Ga parent phase to the fourfold symmetry of the YSZ substrate's (100) cubic surface.

Except for the aforementioned distinctive features, the MIR effect observed here displays a temperature dependency similar to that reported for single crystals. The magnetic field required to activate the MIR effect decreases at higher temperatures. Such behavior is attributed to a drop in the twinning stress at elevated temperatures as well as the increased thermal activation of twin boundary motion.

In addition to the MIR effect, the $Ni_{51}Mn_{29}Ga_{20}$ (at.%) films also show a large magnetocaloric effect (MCE). The MCE is particularly strong at low magnetic fields, yielding a negative magnetic entropy change as large as 1.4 J/kg-K for a magnetic field interval of only 0.5 T at 355 K. The maximum magnetic entropy change occurs at the temperature where the austenitic and martensitic phases coexist at an equal volume fraction. Consistent with this finding is the temperature dependence of the magnetic entropy change where the position of the peak is dependent upon whether a heating or cooling sequence is used. A 3 K temperature hysteresis has been observed between the two thermal paths. Associated with this hysteresis is a peak height which is significantly larger for the cooling sequence.

The large magnetic entropy change results from a concurrent ferromagnetic and martensitic phase transformation where the ferromagnetic ordering of the austenitic phase occurs in the temperature range of 359 to 352 K while the reversible martensitic transformation takes place between 307 K and 370 K. The contributions from the two phase transitions cannot be described through a simple addition. In fact, the total magnetic entropy change at a given temperature depends on the overall magnetization difference in the austenitic and martensitic phases, and thus, is dependent on both the volume fraction of each phase and the percentage of austenite which has transformed from the paramagnetic to ferromagnetic phase. Maximizing the latter would weaken the former, since the overall magnetization difference between the two structural phases is reduced when the total magnetization of austenitic phase increases as a result of the completion of the ferromagnetic transition.

The temperature associated with the maximum magnetic entropy change is determined by the first-order martensitic transition. The ferromagnetic transition, while not playing a role in determining the position of the maximum, does augment the MCE by providing a contribution derived from the ordering of the magnetic subsystem. This enhancement is significant since the films show a nearly 30% greater magnetic entropy change for the cooling sequence over that of the heating sequence due to a larger ferromagnetic signature of the austenitic phase upon cooling. Taken together, the work presented here shows an intricate interdependence between the MCE and the concurrent structural and magnetic phase transformations of Ni-Mn-Ga, where the effect is optimized through a compromise between the relative contributions obtained from each transformation.

The Ni-Mn-Ga films deposited on the (100) MgO substrate also show a highly twinned microstructure at room temperature. The observed grain structure has three possible orientations normal to the substrate ([100], [010], and [001]) where each has two in-plane orientations offset by a 90° azimuthal angle. Such a grain structure results in a weave-like surface morphology, comprised of an intricate surface relief with features propagating along either the [011] or the $[01\bar{1}]$ direction of the (100) MgO substrate, corresponding to the two perpendicularly oriented martensite plates.

The films were fabricated into free-standing micro-bridges using photolithography followed by wet chemical etching. A plaid pattern has been observed in the detached bridge arm, which is attributed to the change in the local stress field which occurs when a film is released from its substrate. Evident from the detached bridge abutment is the disappearance of one of the two sets of surface relief patterns, a phenomenon indicative of a microstructural reorganization in these areas. However, a thorough understanding of the phenomena requires further experimental investigations.

In summary, we have successfully fabricated Ni-Mn-Ga films with the correct composition and a high degree of crystallinity. The films have been examined using a number of different experimental techniques. The main focus of these studies was to characterize the texture, microstructure, phase transformations, and magnetic properties. Major functional properties, i.e. martensitic variant reorientation induced by an external magnetic field or a changed stress field and the magnetocaloric effect, have been studied. The mechanisms governing these effects have been proposed.

References

Aharoni, A. 1996. *Introduction to the theory of ferromagnetism*. International series of monographs on physics v.93. New York: Oxford University Press.

Ahn, J. P., Cheng, N., Lograsso, T., & Krishnan, K. M. 2001. Magnetic properties, structure and shape-memory transitions in Ni-Mn-Ga thin films grown by ion-beam sputtering. *IEEE Transactions on magnetics*, **37**(4), 2141.

Albertini, F., Morellon, L., Algarabel, P. A., Ibarra, M. R., Pareti, L., Arnold, Z., & Calestani, G. 2001. Magnetoelastic effects and magnetic anisotropy in Ni_2MnGa polycrystals. *Journal of Applied Physics*, **89**(10), 5614–5617.

Anson, T. 1999. Shape Memory Alloys - Medical Applications. *Materials World*, **7**(12), 745.

Arrott, A., & Noakes, J. E. 1967. Approximate Equation of State For Nickel Near its Critical Temperature. *Physical Review Letters*, **19**(14), 786.

Arrott, Anthony. 1957. Criterion for Ferromagnetism from Observations of Magnetic Isotherms. *Physical Review*, **108**(6), 1394.

Aydiner, C. C., Bernier, J. V., Clausen, B., Lienert, U., Tome, C. N., & Brown, D. W. 2009. Evolution of stress in individual grains and twins in a magnesium alloy aggregate. *Physical Review B*, **80**, 024113.

Ayuela, A., Enkovaara, J., Ullakko, K., & Nieminen, R. M. 1999. Structural properties of magnetic Heusler alloys. *Journal of Physics-Condensed Matter*, **11**(8), 2017.

Baruchel, J., Palmer, S. B., & Schlenker, M. 1981. Observation of chirality domains in terbium by polarized neutron diffraction topography. *Journal de Physique*, **42**(9), 1279.

Bhadeshia, H. K. D. H., & Honeycombe, R. W. K. 2006. *Steels: microstructure and properties.* third edn. Butterworths-Heinemann (Elsevier).

Borisenko, I. D., Koledov, V. V., Khovailo, V. V., & Shavrov, V. G. 2005. Martensitic and magnetic phase transitions in ternary ferromagnetic alloys Ni-Mn-Ga. *Journal of Magnetism and Magnetic Materials*, **300**, e486.

Bozhko, A. D., Vasil'ev, A. N., Khovailo, V. V., Dikshtein, I. E., Koledov, V. V., Seletskii, S. M., Tulaikova, A. A., Cherechukin, A. A., Shavrov, V. G., & Buchel'nikov, V. D. 1999. Magnetic and structural phase transitions in the shape-memory ferromagnetic alloys $Ni_{2+x}Mn_{1-x}Ga$. *Journal of Experimental and Theoretical Physics*, **88**(5), 954.

Britten, J. F., & Guan, W. 2007. MAX3D - Visualization of Reciprocal Space Volumes. *IUCr Commission on Crystallographic Computing Newsletter*, **8**, 96.

Brown, P. J., Crangle, J., Kanomata, T., Matsmuoto, M., Neumann, K. U., Ouladdiaf, B., & Ziebeck, K. R. A. 2002. The crystal structure and phase transitions of the magnetic shape memory compound Ni_2MnGa. *Journal of Physics-Condensed Matter*, **14**(43), 10159.

Brown, P. J., Gandy, A. P., Kanomata, T., Matsumoto, M., Neumann, K., Neumann, K. U., Sheikh, A., & Ziebeck, K. R. A. 2008. The crystal structures and transformation mechanisms in stoichiometric Ni_2MnGa. Materials Science Forum, vol. 583. Switzerland: Trans Tech Publications Ltd.

Bruker-AXS. 1999. General Area Detector Diffraction System (GADDS) User's Manual. *Bruker AXS Inc.*

Bruker-AXS. 2009. *Bruker AXS Inc.*, www.bruker.com.

Buschbeck, J., Niemann, R., Heczko, O., Thomas, M., Schultz, L., & Fahler, S. 2009. In situ studies of the martensitic transformation in epitaxial Ni-Mn-Ga films. *Acta Materialia*, **57**(8), 2516.

Chernenko, V. A. 1999. Compositional instability of beta-phase in Ni-Mn-Ga alloys. *Scripta Materialia*, **40**(5), 523.

Chernenko, V. A., Pons, J., Segui, C., & Cesari, E. 2002. Premartensitic phenomena and other phase transformations in Ni-Mn-Ga alloys studied by dynamical mechanical analysis and electron diffraction. *Acta Materialia*, **50**(1), 53.

Chernenko, V. A., L'vov, V. A., Zagorodnyuk, S. P., & Takagi, T. 2003. Ferromagnetism of thermoelastic martensites: Theory and experiment. *Physical Review B*, **67**(6), 064407.

Chernenko, V. A., Anton, R. L., Kohl, M., Ohtsuka, M., Orue, I., & Barandiaran, J. M. 2005a. Magnetic domains in Ni-Mn-Ga martensitic thin films. *Journal of Physics-Condensed Matter*, **17**(34), 5215.

Chernenko, V. A., Ohtsuka, M., Kohl, M., Khovailo, V. V., & Takagi, T. 2005b. Transformation behavior of Ni-Mn-Ga thin films. *Smart Materials & Structures*, **14**(5), S245.

Chernenko, V. A., Anton, R. L., Barandiaran, J. M., Orue, I., Besseghini, S., Ohtsuka, M., & Gambardella, A. 2008. MFM Domain Imaging of Textured Ni-Mn-Ga/MgO(100) Thin Films. *Ieee Transactions on Magnetics*, **44**(11), 3040.

Chernenko, Volodymyr A., Hagler, Michael, Mullner, Peter, Kniazkyi, Volodymyr M., L'Vov, Victor A., Ohtsuka, Makoto, & Besseghini, Stefano. 2007. Magnetic susceptibility of martensitic Ni-Mn-Ga film. *Journal of Applied Physics*, **101**(5), 053909.

Christian, J. W. 1987. *The Theory of Transformations in Metals and Alloys*. International Series of Monographs in Metal Physics and Physical Metallurgy, vol. 7. Pergamon Press.

Colinet, C., & Pasturel, A. 2002. Ab initio calculation of the formation energies of $L1_2$, $D0_{22}$, $D0_{23}$ and one dimensional long period structures in $TiAl_3$ compound. *Intermetallics*, **10**(8), 751.

Cui, Y. T., Liu, Z. H., Zhang, M., Liu, G. D., Li, Y. X., Wang, W. L., & Wu, G. H. 2005. Temperature stability of magnetic field-induced strain and field-controlled shape memory effect on $Ni_{52}Mn_{16.4}Fe_8Ga_{23.6}$ single crystals. *Magnetics, IEEE Transactions on*, **41**(3), 1086.

Cullity, B. D., & Graham, C. D. 2009. *Introduction to magnetic materials*. second edn. Hoboken, New Jersey: John Wiley & Sons, Inc.

Digital-Instruments. 1996. Magnetic Force Microscopy (MFM)-Applicable to Dimension Series and MultiMode Systems. *Support Note*, **229**(Rev. B), 4.

Digital-Instruments. 2008. *Digital Instruments is now Veeco Instruments, www.veeco.com.*

Dong, J. W., Chen, L. C., Xie, J. Q., Muller, T. A. R., Carr, D. M., Palmstrom, C. J., McKernan, S., Pan, Q., & James, R. D. 2000. Epitaxial growth of ferromagnetic Ni_2MnGa on GaAs(001) using NiGa interlayers. *Journal of Applied Physics*, **88**(12), 7357.

Dong, J. W., Xie, J. Q., Lu, J., Adelmann, C., Palmstrom, C. J., Cui, J., Pan, Q., Shield, T. W., James, R. D., & McKernan, S. 2004. Shape memory and ferromagnetic shape memory effects in single-crystal Ni_2MnGa thin films. *Journal of Applied Physics*, **95**(5), 2593.

Dubowik, J., Kudryavtsev, Y. V., & Lee, Y. P. 2004. Ferromagnetic resonance observation of martensitic phase transformation in Ni_2MnGa films. *Journal of Magnetism and Magnetic Materials*, **272-76**, 1178.

Funakubo, H. (ed). 1987. *Shape Memory Alloys*. Gordon and Breach Science Publishers.

Gass, J., Srikanth, H., Kislov, N., Srinivasan, S. S., & Emirov, Y. 2008. Magnetization and magnetocaloric effect in ball-milled zinc ferrite powder. *Journal of Applied Physics*, **103**(7), 07B309.

Goldstein, J., Newbury, D.E., Joy, D.C., Lyman, C.E., Echlin, P., Lifshin, E., Sawyer, L.C., & Michael, J.R. 2003. *Scanning electron microscopy and x-ray microanalysis*. Springer.

Golub, V. O., Vovk, A. Y., Malkinski, L., O'Connor, C. J., Wang, Z. J., & Tang, J. K. 2004. Anomalous magnetoresistance in NiMnGa thin films. *Journal of Applied Physics*, **96**(7), 3865.

Gomez-Polo, C., Perez-Landazabal, J. I., Recarte, V., Sanchez-Alarcos, V., & Chernenko, V. A. 2009. Temperature and time dependent magnetic phenomena in a nearly stoichiometric Ni_2MnGa alloy. *Journal of Physics-Condensed Matter*, **21**(2), 026020.

Gorria, P., Llamazares, J. L. S., Alvarez, P., Perez, M. J., Marcos, J. S., & Blanco, J. A. 2008. Relative cooling power enhancement in magneto-caloric nanostructured Pr_2Fe_17. *Journal of Physics D-Applied Physics*, **41**(19), 192003.

Gschneidner, K. A., & Pecharsky, V. K. 2000. Magnetocaloric materials. *Annual Review of Materials Science*, **30**, 387.

Gutierrez, J., Barandiaran, J. M., Lazpita, P., Segui, C., & Cesari, E. 2006. Magnetic properties of a rapidly quenched Ni-Mn-Ga shape memory alloy. *Sensors and Actuators a-Physical*, **129**(1-2), 163.

Hakola, A., Heczko, O., Jaakkola, A., Kajava, T., & Ullakko, K. 2004a. Ni-Mn-Ga films on Si, GaAs and Ni-Mn-Ga single crystals by pulsed laser deposition. *Applied Surface Science*, **238**(1-4), 155.

Hakola, A., Heczko, O., Jaakkola, A., Kajava, T., & Ullakko, K. 2004b. Pulsed laser deposition of NiMnGa thin films on silicon. *Applied Physics a-Materials Science & Processing*, **79**(4-6), 1505.

Handley, R. C. O'. 1998. Model for strain and magnetization in magnetic shape-memory alloys. *Journal of Applied Physics*, **83**(6), 3263.

Heczko, O. 2005. Magnetic shape memory effect and magnetization reversal. *Journal of Magnetism and Magnetic Materials*, **290**, 787.

Heczko, O., Sozinov, A., & Ullakko, K. 2000. Giant field-induced reversible strain in magnetic shape memory NiMnGa alloy. *IEEE Transactions on Magnetics*, **36**(5), 3266.

Heczko, O., Straka, L., Lanska, N., Ullakko, K., & Enkovaara, J. 2002. Temperature dependence of magnetic anisotropy in Ni-Mn-Ga alloys exhibiting giant field-induced strain. *Journal of Applied Physics*, **91**, 8228–8230.

Heczko, O., Thomas, M., Buschbeck, J., Schultz, L., & Fahler, S. 2008. Epitaxial Ni-Mn-Ga films deposited on $SrTiO_3$ and evidence of magnetically induced reorientation of martensitic variants at room temperature. *Applied Physics Letters*, **92**(7), 072502.

Heczko, Oleg, & Straka, Ladislav. 2003. Temperature dependence and temperature limits of magnetic shape memory effect. *Journal of Applied Physics*, **94**(11), 7139.

Hubert, A., & Schafer, R. 1998. *Magnetic Domains-The Analysis of Magnetic Microstructures.* Springer.

Isokawa, S., Suzuki, M., Ohtsuka, M., Matsumoto, M., & Itagaki, K. 2001. Shape Memory Effect of Sputtered Ni-rich Ni_2MnGa Alloy Films Aged in Constraint Condition. *Materials Transactions, JIM*, **42**(9), 1886.

Jakob, G., & Elmers, H. J. 2007. Correlation of electronic structure and martensitic transition in epitaxial Ni_2MnGa films. *Physical Review B*, **76**, 174407.

Jenkins, C. A., Ramesh, R., Huth, M., Eichhorn, T., Porsch, P., Elmers, H. J., & Jakob, G. 2008. Growth and magnetic control of twinning structure in thin films of Heusler shape memory compound Ni_2MnGa. *Applied Physics Letters*, **93**(23), 234101.

Jiang, C. B., Liang, T., Xu, H. B., Zhang, M., & Wu, G. H. 2002. Superhigh strains by variant reorientation in the nonmodulated ferromagnetic NiMnGa alloys. *Applied Physics Letters*, **81**(15), 2818.

Jiang, C. B., Muhammad, Y., Deng, L. F., Wu, W., & Xu, H. B. 2004. Composition dependence on the martensitic structures of the Mn-rich NiMnGa alloys. *Acta Materialia*, **52**(9), 2779.

Jin, X., Marioni, M., Bono, D., Allen, S. M., O'Handley, R. C., & Hsu, T. Y. 2002. Empirical mapping of Ni-Mn-Ga properties with composition and valence electron concentration. *Journal of Applied Physics*, **91**(10), 8222.

Kanomata, T., Shirakawa, K., & Kaneko, T. 1987. Effect of Hydrostatic-Pressure on the Curie-Temperature of the Heusler Alloys Ni_2MnGa, Ni_2MnIn, Ni_2MnSn and Ni_2MnSb. *Journal of Magnetism and Magnetic Materials*, **65**(1), 76.

Khan, M., Stadler, S., Craig, J., Mitchell, J., & Ali, N. 2006. The overlap of first- and second-order phase transitions and related magnetic entropy changes in $Ni_{2+x}Mn_{1-x}Ga$ Heusler alloys. *IEEE Transactions on Magnetics*, **42**(10), 3108.

Khelfaoui, F., Kohl, M., Buschbeck, J., Heczko, O., Faehler, S., & Schultz, L. 2008. A fabrication technology for epitaxial Ni-Mn-Ga microactuators. *European Physical Journal-Special Topics*, **158**, 167.

Khovailo, V. V., Takagi, T., Vasilev, A. N., Miki, H., Matsumoto, M., & Kainuma, R. 2001. On order-disorder ($L2_1 \rightarrow B2'$) phase transition in $Ni_{2+x}Mn_{1-x}Ga$ Heusler alloys. *Physica Status Solidi a-Applied Research*, **183**(2), R1.

Khovaylo, V. V., Buchelnikov, V. D., Kainuma, R., Koledov, V. V., Ohtsuka, M., Shavrov, V. G., Takagi, T., Taskaev, S. V., & Vasiliev, A. N. 2005. Phase transitions in $Ni_{2+x}Mn_{1-x}Ga$ with a high Ni excess. *Physical Review B*, **72**(22), 224408.

Khovaylo, V. V., Skokov, K. P., Koshkid'ko, Y. S., Koledov, V. V., Shavrov, V. G., Buchelnikov, V. D., Taskaev, S. V., Miki, H., Takagi, T., & Vasiliev, A. N. 2008. Adiabatic temperature change at first-order magnetic phase transitions: $Ni_{2.19}Mn_{0.81}Ga$ as a case study. *Physical Review B*, **78**, 060403.

Kohl, M., Brugger, D., Ohtsuka, M., & Takagi, T. 2004. A novel actuation mechanism on the basis of ferromagnetic SMA thin films. *Sensors and Actuators a-Physical*, **114**(2-3), 445–450.

Kohl, M., Agarwal, A., Chernenko, V. A., Ohtsuka, M., & Seemann, K. 2006. Shape memory effect and magnetostriction in polycrystalline Ni-Mn-Ga thin film microactuators. *Materials Science and Engineering A*, **438-440**(SPEC ISS), 940.

Koike, K., Ohtsuka, M., Honda, Y., Katsuyama, H., Matsumoto, M., Itagaki, K., Adachi, Y., & Morita, H. 2007. Magnetoresistance of Ni-Mn-Ga-Fe ferromagnetic shape memory films. *Journal of Magnetism and Magnetic Materials*, **310**(2), 996.

Kubler, J., William, A. R., & Sommers, C. B. 1983. Formation and coupling of magnetic moments in Heusler alloys. *Physical Review B*, **28**(4), 1745.

Kulkova, S. E., Kulkov, S. S., & Subashiev, A. V. 2006. Ab-initio investigation of electronic and magnetic properties of Heusler alloys. *Computational Materials Science*, **36**, 249.

Lai, Y. W., Scheerbaum, N., Hinz, D., Gutfleisch, O., Schafer, R., Schultz, L., & McCord, J. 2007. Absence of magnetic domain wall motion during magnetic field induced twin boundary motion in bulk magnetic shape memory alloys. *Applied Physics Letters*, **90**(19).

Li, F., Xu, Z., Wei, X., Yao, X., & Jin, L. 2008. Domain switching contribution to piezoelectric response in $BaTiO_3$ single crystals. *Applied Physics Letters*, **93**(19), 192904.

Liu, C., Gao, Z. Y., An, X., Wang, H. B., Gao, L. X., & Cai, W. 2008. Surface characteristics and nanoindentation study of Ni-Mn-Ga ferromagnetic shape memory sputtered thin films. *Applied Surface Science*, **254**(9), 2861.

Liu, Z. H., Zhang, M., Wang, W. Q., Wang, W. H., Chen, J. L., Wu, G. H., Meng, F. B., Liu, H. Y., Liu, B. D., Qu, J. P., & Li, Y. X. 2002. Magnetic properties and martensitic transformation in quaternary Heusler alloy of NiMnFeGa. *Journal of Applied Physics*, **92**(9), 5006–5010.

Lodder, J. C. 1983. R.f.-sputtered Co-Cr layers for perpendicular magnetic recording I: Structural properties. *Thin Solid Films*, **101**(1), 61.

Long, Y., Zhang, Z. Y., Wen, D., Wu, G. H., Ye, R. C., Chang, Y. Q., & Wan, F. R. 2005. Phase transition processes and magnetocaloric effects in the Heusler alloys NiMnGa with concurrence of magnetic and structural phase transition. *Journal of Applied Physics*, **98**(4), 046102.

Mahan, J. E. 2000. *Physical Vapor Deposition of Thin Films*. New York: Wiley & Sons.

Mahnke, Guido J., Seibt, M., & Mayr, S. G. 2008. Microstructure and twinning in epitaxial NiMnGa films. *Physical Review B (Condensed Matter and Materials Physics)*, **78**(1), 012101.

Marioni, M. A., O'Handley, R. C., & Allen, S. M. 2003. Pulsed magnetic field-induced actuation of Ni-Mn-Ga single crystals. *Applied Physics Letters*, **83**(19), 3966.

Mavroidis, C. 2002. Development of Advanced Actuators Using Shape Memory Alloys and Electrorheological Fluids. *Research in Nondestructive Evaluation*, **14**(1), 1–32.

McMichael, R. D., Ritter, J. J., & Shull, R. D. 1993. Enhanced magnetocaloric effect in

$Gd_3Ga_{5-x}Fe_xO_{12}$. *Journal of Applied Physics*, **73**, 6946.

Morelli, D. T., Mance, A. M., Mantese, J. V., & Micheli, A. L. 1996. Magnetocaloric properties of doped lanthanum manganite films. *Journal of Applied Physics*, **79**(1), 373.

Morrish, A. H. 1965. *The Physical Principles of Magnetism*. New York: Wiley & Sons.

Muller, M. W. 1961. Distribution of the Magnetization in a Ferromagnet. *Physical Review*, **122**(5), 1485.

Murray, S. J., Marioni, M., Allen, S. M., O'Handley, R. C., & Lograsso, T. A. 2000. 6 % magnetic-field-induced strain by twin-boundary motion in ferromagnetic Ni-Mn-Ga. *Applied Physics Letters*, **77**(6), 886–888.

O'Handley, R. C. 2000. *Modern Magnetic Materials-Principles and Applications*. New York: John Wiley & Sons, INC.

O'Handley, R. C., Paul, D. I., Allen, S. M., Richard, M., Feuchtwanger, J., Peterson, B., Techapiesancharoenkij, R., Barandiaran, M., & Lazpita, P. 2006. Model for temperature dependence of field-induced strain in ferromagnetic shape memory alloys. *Materials Science and Engineering: A*, **438-440**, 445.

Ohtsuka, M., & Itagaki, K. 2000. Effect of heat treatment on properties of Ni-Mn-Ga films prepared by a sputtering method. *International Journal of Applied Electromagnetics and Mechanics*, **12**(1-2), 49.

Ohtsuka, M., Matsumoto, M., & Itagaki, K. 2006. Two-way shape memory behavior of sputter-deposited Ni-rich Ni_2MnGa films. *Journal of Intelligent Material Systems and Structures*, **17**(12), 1069.

Okamoto, N., Fukuda, T., Kakeshita, T., & Takeuchi, T. 2006. Magnetocrystalline anisotropy and twinning stress of 10M and 2M martensites in Ni-Mn-Ga system. Materials Science Forum, vol. 512. Switzerland: Trans Tech Publications Ltd.

Overholser, R. W., Wuttig, M., & Neumann, D. A. 1999. Chemical ordering in Ni-Mn-Ga Heusler alloys. *Scripta Materialia*, **40**(10), 1095.

Panish, M. B., & Temkin, H. 1993. *Gas Source Molecular Beam Epitaxy: Growth and Properties of Phosphorus Containing III-V Heterostructures*. Springer Series in Materials Science, vol. 26. Verlag: Spinger.

Pareti, L., Solzi, M., Albertini, F., & Paoluzi, A. 2003. Giant entropy change at the co-occurrence of structural and magnetic transitions in the $Ni_{2.19}Mn_{0.81}Ga$ Heusler alloy. *European Physical Journal B*, **32**(3), 303.

Park, Seung-Eek, & Shrout, Thomas R. 1997. Ultrahigh strain and piezoelectric behavior in relaxor based ferroelectric single crystals. *Journal of Applied Physics*, **82**(4), 1804.

Pasquale, M. 2003. Mechanical sensors and actuators. *Sensors and Actuators A: Physical*, **106**(1-3), 142.

Pasquale, M., Sasso, C. P., Besseghini, S., Villa, E., & Chernenko, V. 2002. Temperature dependence of magnetically induced strain in single crystal samples of Ni-Mn-Ga. *Journal of Applied Physics*, **91**(10), 7815.

Pasquale, M., Sasso, C. P., Lewis, L. H., Giudici, L., Lograsso, T., & Schlagel, D. 2005. Magnetostructural transition and magnetocaloric effect in $Ni_{55}Mn_{20}Ga_{25}$ single crystals. *Physical Review B*, **72**(9), 094435.

Pecharsky, V. K., & Gschneidner, K. A. 1997. Tunable magnetic regenerator alloys with a giant magnetocaloric effect for magnetic refrigeration from $\sim$20 to $\sim$290 K. *Applied Physics Letters*, **70**(24), 3299.

Pecharsky, V. K., & Gschneidner, K. A. 1999a. Heat capacity near first order phase transitions and the magnetocaloric effect: An analysis of the errors, and a case study of $Gd_5(Si_2Ge_2)$ and Dy. *Journal of Applied Physics*, **86**(11), 6315.

Pecharsky, V. K., & Gschneidner, K. A. 1999b. Magnetocaloric effect from indirect measurements: Magnetization and heat capacity. *Journal of Applied Physics*, **86**(1), 565.

Peterson, B. W., Allen, S. M., & O'Handley, R. C. 2008. Temperature dependence of the magnetic-field-induced strain of NiMnGa in the presence of an acoustic drive. *Journal of Applied Physics*, **104**(3), 033918.

Planes, A., Manosa, L., & Acet, M. 2009. Magnetocaloric effect and its relation to shape-memory properties in ferromagnetic Heusler alloys. *Journal of Physics-Condensed Matter*, **21**(23), 29.

Porsch, P., Kallmayer, M., Eichhorn, T., Jakob, G., Elmers, H. J., Jenkins, C. A., Felser, C., Ramesh, R., & Huth, M. 2008. Suppression of martensitic phase transition at the Ni_2MnGa film surface. *Applied Physics Letters*, **93**(2), 022501.

Pramanik, A. K., & Banerjee, A. 2009. Critical behavior at paramagnetic to ferromagnetic phase transition in $Pr_{0.5}Sr_{0.5}MnO_3$: A bulk magnetization study. *Physical Review B*, **79**(21), 7.

Provenzano, Virgil, Shapiro, Alexander J., & Shull, Robert D. 2004. Reduction of hysteresis losses in the magnetic refrigerant $Gd_5Ge_2Si_2$ by the addition of iron. *Nature*, **429**(6994), 853.

Rave, W., Schafer, R., & Hubert, A. 1987. Quantitative observation of magnetic domains with the magneto-optical Kerr effect. *Journal of Magnetism and Magnetic Materials*, **65**(1), 7.

Recarte, V., Perez-Landazabal, J. I., Sanchez-Alarcos, V., Chernenko, V. A., & Ohtsuka, M. 2009. Magnetocaloric effect linked to the martensitic transformation in sputter-deposited Ni-Mn-Ga thin films. *Applied Physics Letters*, **95**(14), 141908.

Rumpf, H., Craciunescu, C. M., Modrow, H., Olimov, K., Quandt, E., & Wuttig, M. 2006. Successive occurrence of ferromagnetic and shape memory properties during crystallization of NiMnGa freestanding films. *Journal of Magnetism and Magnetic Materials*, **302**(2), 421.

Ryhanen, J. 1999. *Biocompatibility Evaluation of Nickel Titanium Shape Memory Alloy*. Ph.D. thesis, University of Oulu.

Saenz, J. J., & Garcia, N. 1987. Observation of magnetic forces by the atomic force microscope. *Journal of Applied Physics*, **62**, 4293.

Saito, Nobuo, Fujiwara, Hideo, & Sugita, Yutaka. 1964. A new type of magnetic domain in thin Ni-Fe films. *Journal of the Physical Society of Japan*, **19**, 421.

Sarkar, P., Mandal, P., & Choudhury, P. 2008. Large magnetocaloric effect in Sm[sub 0.52]Sr[sub 0.48]MnO[sub 3] in low magnetic field. *Applied Physics Letters*, **92**(18), 182506.

Shanina, B. D., Konchits, A. A., Kolesnik, S. P., Gavriljuk, V. G., Glavatskij, I. N., Glavatska, N. I., Soderberg, O., Lindroos, V. K., & Foct, J. 2001. Ferromagnetic resonance in non-stoichiometric $Ni_{1-x-y}Mn_xGay$. *Journal of Magnetism and Magnetic Materials*, **237**(3), 309.

Sharma, V. K., Chattopadhyay, M. K., Kumar, R., Ganguli, T., Tiwari, P., & Roy, S. B. 2007. Magnetocaloric effect in Heusler alloys $Ni_{50}Mn_{34}In_{16}$ and $Ni_{50}Mn_{34}Sn_{16}$. *Journal of Physics-Condensed Matter*, **19**(49), 496207.

Soderberg, O., Ge, Y., Sozinov, A., Hannula, S. P., & Lindroos, V. K. 2005. Recent breakthrough development of the magnetic shape memory effect in Ni-Mn-Ga alloys. *Smart Materials & Structures*, **14**(5), S223.

Soderberg, O., Aaltio, I., Ge, Y., Heczko, O., & Hannula, S. P. 2008. Ni-Mn-Ga multifunctional compounds. *Materials Science and Engineering a-Structural Materials Properties Microstructure and Processing*, **481**, 80.

Sozinov, A., Likhachev, A. A., & Ullakko, K. 2002a. Crystal structures and magnetic anisotropy properties of Ni-Mn-Ga martensitic phases with giant magnetic-field-induced strain. *IEEE Transactions on Magnetics*, **38**(5), 2814.

Sozinov, A., Likhachev, A. A., Lanska, N., & Ullakko, K. 2002b. Giant magnetic-field-induced strain in NiMnGa seven-layered martensitic phase. *Applied Physics Letters*, **80**(10), 1746.

Stanley, H. E. 1971. *Introduction to phase transitions and critical phenomena.* The international series of monographs on physics. New York: Oxford University Press.

Straka, L., & Heczko, O. 2005. Reversible 6 % strain of Ni-Mn-Ga martensite using opposing exterrical stress in static and variable magnetic fields. *Journal of Magnetism and Magnetic Materials*, **290**, 829.

Straka, L., & Heczko, O. 2006. Magnetization changes in Ni-Mn-Ga magnetic shape memory single crystal during compressive stress reorientation. *Scripta Materialia*, **54**(9), 1549.

Straka, L., Heczko, O., & Hannula, S. P. 2006. Temperature dependence of reversible field-induced strain in Ni-Mn-Ga single crystal. *Scripta Materialia*, **54**(8), 1497–1500.

Suorsa, K., Pagounis, E., & Ullakko, K. 2004. Magnetic shape memory actuator performance. *Journal of Magnetism and Magnetic Materials*, **272-76**, 2029.

Suzuki, M., Ohtsuka, M., Matssumoto, M., Murakami, Y., Shindo, D., & Itagaki, K. 2002. Effect of Aging Time on Shape Memory Properties of Sputtered Ni-rich Ni_2MnGa Alloy Films. *Materials transactions JIM*, **43**(5), 861.

Tang, Y. J., Solomon, V. C., Smith, D. J., Harper, H., & Berkowitz, A. E. 2005. Magnetocaloric effect in NiMnGa particles produced by spark erosion. *Journal of Applied Physics*, **97**(10), 10M309.

Tello, P. G., Castano, F. J., O'Handley, R. C., Allen, S. M., Esteve, M., Castano, F., Labarta, A., & Batlle, X. 2002. Ni-Mn-Ga thin films produced by pulsed laser deposition. *Journal of Applied Physics*, **91**(10), 8234.

Thomas, M., Heczko, O., Buschbeck, J., Rossler, U. K., McCord, J., Scheerbaum, N., Schultz, L.,

& Fahler, S. 2008a. Magnetically induced reorientation of martensite variants in constrained epitaxial Ni-Mn-Ga films grown on MgO(001). *New Journal of Physics*, **10**, 023040.

Thomas, M., Heczko, O., Buschbeck, J., Schultz, L., & Fahler, S. 2008b. Stress induced martensite in epitaxial Ni-Mn-Ga films deposited on MgO(001). *Applied Physics Letters*, **92**(19), 192515.

Tickle, R., & James, R. D. 1999. Magnetic and magnetomechanical properties of Ni_2MnGa. *Journal of Magnetism and Magnetic Materials*, **195**(3), 627.

Tsuchiya, K., Ohashi, A., Ohtoyo, D., Nakayama, K., Umemoto, M., & McCormick, P. G. 2000. Phase transformations and magnetostriction in Ni-Mn-Ga ferromagnetic shape memory alloys. *Materials Transactions Jim*, **41**(8), 938.

Tung, A. T., Park, B. H., Liang, D. H., & Niemeyer, G. 2008. Laser-machined shape memory alloy sensors for position feedback in active catheters. *Sensors and Actuators A: Physical*, **147**(1), 83.

Ullakko, K., Huang, J. K., Kantner, C., Ohandley, R. C., & Kokorin, V. V. 1996. Large magnetic-field-induced strains in Ni_2MnGa single crystals. *Applied Physics Letters*, **69**(13), 1966.

Ullakko, K., Ezer, Y., Sozinov, A., Kimmel, G., Yakovenko, P., & Lindroos, V. K. 2001. Magnetic-field-induced strains in polycrystalline Ni-Mn-Ga at room temperature. *Scripta Materialia*, **44**(3), 475.

Van der PAUW, L. J. 1958. A method of measuring specific resistivity and hall effect of discs of arbitrary shape. *Philips Research Reports*, **13**(1), 1.

Vasil'ev, A. N., Bozhko, A. D., Khovailo, V. V., Dikshtein, I. E., Shavrov, V. G., Buchelnikov, V. D., Matsumoto, M., Suzuki, S., Takagi, T., & Tani, J. 1999. Structural and magnetic phase transitions in shape-memory alloys $Ni_{2+x}Mn_{1-x}Ga$. *Physical Review B*, **59**(2), 1113.

Vasil'ev, A. N., Buchel'nikov, V. D., Takagi, T., Khovailo, V. V., & Estrin, E. I. 2003. Shape memory ferromagnets. *Physics-Uspekhi*, **46**(6), 559.

Veeco-Instruments. 2003. SPM Training Notebook. *www.veeco.com*.

Veeco-Instruments. 2009. *www.veecoprobes.com*.

Wang, W. H., Wu, G. H., Chen, J. L., Gao, S. X., Zhan, W. S., Wen, G. H., & Zhang, X. X. 2001a. Intermartensitic transformation and magnetic-field-induced strain in $Ni_{52}Mn_{24.5}Ga_{23.5}$ single crystals. *Applied Physics Letters*, **79**(8), 1148.

Wang, W. H., Hu, F. X., Chen, J. L., Li, Y. X., Wang, Z., Gao, Z. Y., Zheng, Y. F., Zhao, L. C., Wu, G. H., & Zan, W. S. 2001b. Magnetic properties and structural phase transformations of NiMnGa alloys. *IEEE Transactions on Magnetics*, **37**(4), 2715.

Wang, Y. D., Brown, D. W., Choo, H., Liaw, P. K., Cong, D. Y., Benson, M. L., & Zuo, L. 2007. Experimental evidence of stress-field-induced selection of variants in Ni-Mn-Ga ferromagnetic shape-memory alloys. *Physical Review B (Condensed Matter and Materials Physics)*, **75**(17), 174404.

Webster, P. J., Ziebeck, K. R. A., Town, S. L., & Peak, M. S. 1984. Magnetic Order and Phase-Transformation in Ni_2MnGa. *Philosophical Magazine B-Physics of Condensed Matter Statistical Mechanics Electronic Optical and Magnetic Properties*, **49**(3), 295.

Williams, A. J., & Cahn, R. W. 1963. Deformation Twinning. Gainesville, Florida: Gordon and Breach Science Publishers.

Williams, D. B., & Carter, C. B. 1996. *Transmission Electron Microscopy: A Textbook for Materials Science*. New York: Plenum Press.

Williams, H. J., Bozorth, R. M., & Shockley, W. 1949. Magnetic Domain Patterns on Single Crystals of Silicon Iron. *Physical Review*, **75**(1), 155.

Wilson, S. A., Jourdain, R. P. J., Zhang, Q., Dorey, R. A., Bowen, C. R., Willander, M., Wahab, Q. U., Willander, M., Safaa, M. A. H., Nur, O., Quandt, E., Johansson, C., Pagounis, E., Kohl, M., Matovic, J., Samel, B., van der Wijngaart, W., Jager, E. W. H., Carlsson, D., Djinovic, Z., Wegener, M., Moldovan, C., Iosub, R., Abad, E., Wendlandt, M., Rusu, C., & Persson, K. 2007. New materials for micro-scale sensors and actuators An engineering review. *Materials Science & Engineering R-Reports*, **56**(1-6), 1.

Wood, M. E., & Potter, W. H. 1985. General analysis of magnetic refrigeration and its optimization using a new concept: maximization of refrigerant capacity. *Cryogenics*, **25**(12), 667.

Wuttig, M., Craciunescu, C., & Li, J. 2000. Phase Transformations in Ferromagnetic NiMnGa Shape Memory Films. *Material Transactions, JIM*, **41**(8), 933.

Zhang, Y., Hughes, R. A., Britten, J. F., Gong, W., Preston, J. S., Botton, G. A., & Niewczas, M. 2009. Epitaxial Ni-Mn-Ga films derived through high temperature in situ depositions. *Smart*

Materials & Structures, **18**(2), 025019.

Zhang, Y. P. 2003. *Thermal Cycling Behavior in Cu-Zn-Al Shape Memory Alloys.* Master thesis, McMaster University.

Zhou, X. Z., Li, W., Kunkel, H. P., & Williams, G. 2004. A criterion for enhancing the giant magnetocaloric effect: Ni-Mn-Ga a promising new system for magnetic refrigeration. *Journal of Physics: Condensed Matter*, **16**, L39.

Zhou, X. Z., Li, W., Kunkel, H. P., & Williams, G. 2005a. Influence of the nature of the magnetic phase transition on the associated magnetocaloric effect in the Ni-Mn-Ga system. *Journal of Magnetism and Magnetic Materials*, **293**(3), 854.

Zhou, X. Z., Li, W., Kunkel, H. P., Williams, G., & Zhang, S. H. 2005b. Relationship between the magnetocaloric effect and sequential magnetic phase transitions in Ni-Mn-Ga alloys. *Journal of Applied Physics*, **97**(10), 10M515.